NASA/TM–2012–216001

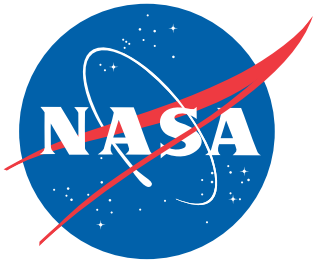

Shielded-twisted-pair cable model for chafe fault detection via time-domain reflectometry

Stefan R. Schuet
Ames Research Center
Moffett Field, California

Doğan A. Timuçin
Ames Research Center
Moffett Field, California

Kevin R. Wheeler
Ames Research Center
Moffett Field, California

March 2012

NASA STI Program ... in Profile

Since its founding, NASA has been dedicated to the advancement of aeronautics and space science. The NASA scientific and technical information (STI) program plays a key part in helping NASA maintain this important role.

The NASA STI Program operates under the auspices of the Agency Chief Information Officer. It collects, organizes, provides for archiving, and disseminates NASA's STI. The NASA STI Program provides access to the NASA Aeronautics and Space Database and its public interface, the NASA Technical Report Server, thus providing one of the largest collection of aeronautical and space science STI in the world. Results are published in both non-NASA channels and by NASA in the NASA STI Report Series, which includes the following report types:

- TECHNICAL PUBLICATION. Reports of completed research or a major significant phase of research that present the results of NASA programs and include extensive data or theoretical analysis. Includes compilations of significant scientific and technical data and information deemed to be of continuing reference value. NASA counterpart of peer-reviewed formal professional papers, but having less stringent limitations on manuscript length and extent of graphic presentations.
- TECHNICAL MEMORANDUM. Scientific and technical findings that are preliminary or of specialized interest, e.g., quick release reports, working papers, and bibliographies that contain minimal annotation. Does not contain extensive analysis.
- CONTRACTOR REPORT. Scientific and technical findings by NASA-sponsored contractors and grantees.
- CONFERENCE PUBLICATION. Collected papers from scientific and technical conferences, symposia, seminars, or other meetings sponsored or co-sponsored by NASA.
- SPECIAL PUBLICATION. Scientific, technical, or historical information from NASA programs, projects, and missions, often concerned with subjects having substantial public interest.
- TECHNICAL TRANSLATION. English- language translations of foreign scientific and technical material pertinent to NASA's mission.

Specialized services also include creating custom thesauri, building customized databases, and organizing and publishing research results.

For more information about the NASA STI Program, see the following:

- Access the NASA STI program home page at ***http://www.sti.nasa.gov***
- E-mail your question via the Internet to help@sti.nasa.gov
- Fax your question to the NASA STI Help Desk at 443-757-5803
- Phone the NASA STI Help Desk at 443-757-5802
- Write to:
  NASA STI Help Desk
  NASA Center for AeroSpace Information
  7115 Standard Drive
  Hanover, MD 21076–1320

NASA/TM–2012–216001

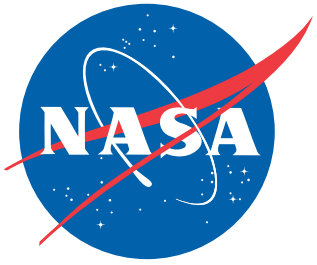

Shielded-twisted-pair cable model for chafe fault detection via time-domain reflectometry

Stefan R. Schuet
Ames Research Center
Moffett Field, California

Doğan A. Timuçin
Ames Research Center
Moffett Field, California

Kevin R. Wheeler
Ames Research Center
Moffett Field, California

National Aeronautics and
Space Administration

Ames Research Center
Moffett Field, California 94035-1000

March 2012

Acknowledgments

This work was funded by NASA's Aeronautics Research Mission Directorate under the Vehicle Systems Safety Technologies Project of the Aviation Safety Program.

Available from:

NASA Center for AeroSpace Information
7115 Standard Drive
Hanover, MD 21076-1320
443-757-5802

Contents

List of Tables

List of Figures

List of Symbols

A	unknown coefficient
$\mathcal{A}$	insulator cross-section
B	unknown coefficient
c	speed of light in the insulator; per-unit-length capacitance
C	unknown coefficient
$\mathcal{C}$	closed contour
$\mathbf{C}$	capacitance matrix
d	distance
e	2.71828
E[·]	statistical expectation operator
$\mathbf{E}$	electric field
f	(linear) frequency
F	magnetic flux; normalized potential
g	measurement forward model
G	measurement gain
$\mathbf{G}$	conductance matrix
$\mathbf{H}$	magnetic field
$H_m^{(1)}(\cdot)$	Hankel function of the first kind
i	$\sqrt{-1}$
i	conductor current
$\mathbf{i}$	current vector
I	constant current
$\Im$	imaginary part
$I_m(\cdot)$	modified Bessel function of the first kind
j	conductor index
$\mathbf{j}$	current vector
$\mathbf{J}$	volume current density
$J_m(\cdot)$	ordinary Bessel function of the first kind
k	wavenumber in the insulator
$\mathbf{K}$	surface current density
$K_m(\cdot)$	modified Bessel function of the second kind
l	per-unit-length inductance
ℓ	length
$\mathbf{L}$	inductance matrix
m	azimuthal eigenvalue; measurement index
M	number of measurements
n	Monte-Carlo sample index
$\hat{\mathbf{n}}$	unit normal vector
N	number of samples
$\mathcal{N}^+$	nonnegative Gaussian distribution
$N_m(\cdot)$	ordinary Bessel function of the second kind
p	helix period
$p(\cdot)$	probability density function

$\mathcal{P}$	integration path
q	wire center offset from origin
Q	electric charge
r	radius
R	(effective) radius
$\Re$	real part
s	noise standard deviation
S_{mn}	S-parameter
$\mathbf{S}$	S matrix
t	time
$\mathbf{u}$	voltage vector
U	mode amplitude
v	conductor voltage; propagation velocity
$\mathbf{v}$	voltage vector
V	mode amplitude
w	width
$\mathcal{W}$	bounding wall
$\mathbf{x}$	eigenvector
y	measurement vector
$\mathbf{y}$	eigenvector
z	per-unit-length impedance
$\hat{\mathbf{z}}$	unit axial vector
$\mathbf{Z}$	impedance matrix
(x, y, z)	rectangular coordinates
α	attenuation index
β	phase index
γ, γ_m	radial eigenvalue
Γ	reflection coefficient
$\delta(\cdot)$	Dirac delta
δ_{mn}	Kronecker delta
$\Delta\phi$	azimuthal interval
Δt	time interval
Δz	axial interval
ϵ	permittivity
ε	relative permittivity
ζ	surface impedance
η	impedance coefficient
θ	unknown parameter vector
κ	helix twist rate
λ	axial eigenvalue
μ	permeability
ν	measurement noise
ξ	wavenumber in metal
π	3.14159
$\boldsymbol{\Pi}$	Hertz vector
$\hat{\boldsymbol{\rho}}$, $\hat{\boldsymbol{\varrho}}$	unit radial vector
σ	conductivity
Σ	surface charge density
τ	capacitance coefficient
$\hat{\boldsymbol{\phi}}$, $\hat{\boldsymbol{\varphi}}$	unit azimuthal vector
Φ	electrostatic potential
χ	eigenvalue
ψ	helix pitch angle

Ψ	Debye potential
ω	(angular) frequency
(ρ, ϕ, z)	(global) cylindrical coordinates
(ϱ, φ, z)	(local) cylindrical coordinates
$\boldsymbol{\nabla}$	nabla
$\parallel$	axial component
$\perp$	transverse component
AC	alternating current
DC	direct current
EWIS	electrical wiring and interconnect system
`fft`	fast Fourier transform
`ifft`	inverse fast Fourier transform
MCMC	Markov-chain Monte Carlo
RF	radio frequency
STP	shielded twisted pair
SUP	shielded uniform pair
TDR	time-domain reflectometry
TDT	time-domain transmissometry
TEM	transverse electromagnetic
VNA	vector network analyzer

Executive Summary

Problem statement. Studies show that electrical wires on aircraft often experience chafing, which causes short circuits or broken wires leading to loss of system functionality, accompanied by smoke and fire events, presenting a serious threat to flight safety. The capability to locate and characterize chafing can potentially enable preventive maintenance well before failures occur, thus maximizing safety while minimizing out-of-service time. In order to realize this capability, however, highly accurate and computationally efficient models are needed to detect, in noisy operating environments, the small electrical effects that chafing can cause.

Overview. This report details the development, verification, and validation of an innovative physics-based model of electrical signal propagation through *shielded-twisted-pair* cable, which is commonly found on aircraft and offers an ideal proving ground for detection of small holes in a shield well before catastrophic damage occurs. The accuracy of this model is verified through numerical electromagnetic simulations using a commercially available software tool. The model is shown to be representative of more realistic (analytically intractable) cable configurations as well. A probabilistic framework is developed for validating the model accuracy with reflectometry data obtained from real aircraft-grade cables chafed in the laboratory.

Main results. The analytical modeling process and its subsequent verification through rigorous numerical simulations and its validation through laboratory measurements resulted in a number of insights relevant to the practice of chafing fault detection. Firstly, the various assumptions and approximations made in deriving the theoretical model were found to be acceptable for the typical cable geometries. In particular, the numerical simulations have shown that the eigenvalues derived from the theoretical model are close enough to the actual eigenvalues of the impedance-controlled cable to be realistic for practical application. This demonstrated ability to derive a highly accurate yet closed-form physics model is a key contribution of this work, as it is crucial for the subsequent development of fast and reliable fault detection algorithms.

The laboratory validation of model accuracy on real aircraft-grade cables required additional steps to model the measurement setup itself and to employ probabilistic methods to infer the key underlying parameters such as effective dielectric permittivity of the insulation and the finite conductivity of the wires and the shield. Notably, the optimal estimates inferred from data differed from the manufacturer's specifications. Overall, the analytical model was able to match lab measurements to within 2 % absolute maximum error out to 1 GHz. Not surprisingly, it was observed that the slight analytical correction for twisting does not have a significant effect on the ability to fit the model to measurements, though it did seem to reduce the bias on the parameter estimates. It was therefore judged that other (unmodeled) elements in the system (*e.g.*, cable imperfections, connectors, *etc.*) are mainly responsible for the residual.

The analytical derivation and supporting simulations lay the foundation for a trade-space study to aid in the requirements specification of both a maintenance tool and an on-board fault diagnosis system. One important observation, relevant to any such study, is that for a fixed fault size and distance from the source, the angular fault location relative to the two inner conductors has a strong effect on the scattered field, and hence creates ambiguity in the ability to quantify fault location and size. It was confirmed that the simple impedance-discontinuity model of a chafe is able to replicate the tell-tale "differentiation" effect of a small hole on a propagating pulse. It was also established empirically that average-size chafes do not produce a sensible reflection or transmission signal below 200 MHz. All other classical trade-offs also exist. For example, a fast rise-time interrogation pulse will be better able to discern the edges of a small fault by using higher frequencies, with the down-side that high frequencies are rapidly attenuated in long cables.

Chapter 1

Introduction

1.1 Problem statement

The electrical wiring and interconnect system (EWIS) in any vehicle is a critical, and sometimes overlooked, subsystem where relatively minor issues can grow and eventually lead to serious safety problems like smoke, fire, and loss of critical system functionality. As such, these types of faults are sometimes considered either *single-point events* where a single component (*e.g.*, a wire) fault causes a system to fail, or *common-cause events* where a single fault causes multiple systems to fail. Such events are generally considered high risk no matter how improbable they may be. Wiring faults, however, do frequently occur in practice, and are clearly capable of leading to both single-point and common-cause fault events; for examples in aviation, see [1, 2].*

While the technology for detecting hard faults (*e.g.*, opens, shorts, and arcing) is available, it only enables mitigation after serious sustained electrical issues occur. Preventive measures, on the other hand, require the *detection* of precursor problems. Wire chafing is one such precursor to both intermittent and full-system breakdown, and is among the most commonly occurring issues identified in wiring health maintenance studies [1]. Thus, the ability to detect and locate chafe faults enables the repair of wiring systems well before serious problems occur, and even in some cases when intermittent faults observed in operation disappear during maintenance. To date, the failed efforts targeted at detecting chafing faults in practice have focused primarily on hardware development. As a result, there is almost no existing research detailing the underlying physics needed to thoroughly understand how signals propagating through the interconnect system are affected by these faults. Such an understanding would allow one to design fault detection algorithms that can optimally identify and locate chafes by extracting fault signatures from native or injected signals propagating on the cable.

This work seeks to fill the primary technology gap identified above by detailing a physics-based model for signal propagation in *shielded-twisted-pair* cable, commonly used in aircraft, among a great variety of other application domains. The chafing of the insulation on an unshielded cable cannot be detected remotely, since the permittivity contrast between most dielectrics and the ambient medium (*e.g.*, air) is too small. Furthermore, the continuously changing distance between an unshielded cable and some nearby metallic surface that serves as a ground plane produces spurious signal reflections which are typically much greater than those caused by chafing alone, as was demonstrated in [3]. The shield not only isolates the internal signals flowing down the cable from the noisy environment, but also serves as a uniform conductor for the return current. As a result, even a small hole in the shield causes enough of a disruption to produce a sensible effect that can be measured at either end of the cable. The focus on shielded cable types is therefore crucial, as this represents the most viable avenue for successful chafe fault detection in the field.

An additional advantage of shielded-twisted-pair cable, for instance over coaxial cable, is that it provides *two* tranmission-line modes—common and differential—for signal propagation. Since the differential mode is used almost exclusively for the transmission of information or power over the cable, the common mode is available and perhaps more suited for signals designed to assess the health of the cable without affecting the

*Absent sufficient preventive diagnostics and prognostics tools for wiring, regular inspections and built-in redundancy are the only currently available protection mechanisms against critical system failures.

primary purpose of the cable itself. For this reason, the experimental results presented here are focused on the common mode, while the theory is derived for both.

The detailed physics-based model developed here is important for at least two reasons. First, it enables one to simulate fault scenarios and noise conditions in order to study and characterize optimal cable and interrogation signal design for fault detection. Second, it has produced an extremely accurate and computationally efficient model suitable for the design of optimal fault detection algorithms, along with the quantification of one's ability to detect faults under a large variety of practical noise conditions, the details of which will be the topic of a future publication.

1.2 Literature survey

An extensive survey of previous work in this area (including literature in German and Russian) was conducted as part of this study, whose pertinent findings will now be summarized.

The two-wire (or twin-lead) transmission line, consisting of a pair of parallel round conductors, has been used extensively in power distribution and telephony applications, and therefore its study garnered much attention in the late 19^{th} and the early 20^{th} centuries. Various techniques (*e.g.*, method of images [4, pp. 162–170], conformal mapping [5, pp. 76–78], variational principles [6, pp. 273–279], *etc.*) may be used to analyze the electromagnetic field distribution around this line. (The requisite presence of insulation around the wires—typically a thin dielectric ribbon which helps to avoid shorting and to maintain uniform spacing between the conductors—changes the physical picture only slightly, and is therefore typically ignored for analytical convenience.)

The introduction of additional wires, or a shield that envelopes the wires, presents significant analytical challenges, which consumed considerable effort. The fundamental difficulty here stems from the fact that there is no known coordinate system in which *all* the conductors can be made to coincide with constant-coordinate surfaces. The techniques mentioned above were generalized to these problems, but the solutions obtained were now approximate [7, 8, 9, 10, 11]. Perhaps a more principled approach to this problem (see, *e.g.*, [12, pp. 38–40 and 53]) entails the representation of charge density around the periphery of each conductor as a Fourier series with unknown coefficients, using the two-dimensional free-space Green function to express the electric field in the space between the conductors as a sum of integrals over the conductor surfaces, and finally imposing the boundary condition of vanishing tangential electric field at each conductor surface. This procedure leads to an infinite set of linear equations for the unknown Fourier coefficients, which may be solved to any desired accuracy. This approach was used by J. Craggs and his followers in calculating the capacitance of the shielded-uniform-pair cable [13, 14, 15, 16, 17, 18]. Unfortunately, this solution approach does not yield a closed-form expression for the field distribution inside the insulator, which one needs when studying the consequences of deviations from the idealized geometry and/or infinite conductivity of the wires and/or the shield.

For long-distance transmission of signals or power, the main concern is attenuation due to energy loss in the conductors. In studying this aspect, metals may no longer be assumed perfectly conducting. Indeed, one must now solve for the fields *everywhere* in the cable, and stitch the solutions together at the metal–insulator interfaces using the appropriate continuity conditions for the fields. The solutions are again in the forms of infinite series whose coefficients may be obtained, at least in principle, to arbitrary orders of accuracy. For the sake of historical accuracy, it should be noted that J. Carson pioneered this general approach in his study of the proximity effect in cables, and in fact suggested in [19]—some 25 years ahead of J. Craggs—that it can be used for the calculation of the cable capacitance (see also [20, 21, 22, 23, 24, 25, 26, 27, 28]). Craggs and his followers seem to have been unaware of this earlier work.

As the density of communication lines increased, cross-talk among cables became a paramount issue. It was recognized that the simple device of twisting the wires around each other endowed the two-wire line with considerable degree of immunity to electromagnetic interference. As one would expect, analytical difficulties persist when one moves to this twisted geometry. The geometric complications arising from the twist may be removed to a large extent by working in a curvilinear coordinate system that twists with the wires, and the resulting field equations may be approached exactly or via perturbation theory [29, 30] (see also [31, pp. 96–101]). Alternatively, the Craggs approach outlined above may be generalized to three dimensions by employing dyadic Green functions (see, *e.g.*, [32, pp. 23–25], [6, pp. 121–130], or [33, pp. 544–549]);

the resulting formulation is known as the electric-field integral equation in the engineering literature (see, *e.g.*, [34, pp. 696–707], [35, pp. 354–356], [6, pp. 139–153], or [33, pp. 617–624]). In any case, the fundamental obstacle posed by the non-separable nature of the conductor surfaces remains, and the final solution can only be obtained numerically, as in [36].

Instead of the continuous Fourier representations of the surface charge distributions adopted by Craggs, the wires may also be represented by discrete volume charges within the bulk of the metal, corresponding to infinitesimal current filaments in three dimensions. This approximation—a perfectly valid alternative parametrization of the normal electric field at the conductor surfaces—considerably improves the analytical tractability of the problem. Such filament models, wherein the wires are treated as conductors of infinitesimal cross-section, were preferred, especially in the early days of modest computing power, in analyzing the radiation characteristics of twisted-pair cables [37, 38, 39, 40, 41, 42]. The geometries considered therein naturally lacked a shield. Mention must also be made of an excellent paper on scattering of plane waves from a uniform pair of round conductors [43], which combines filament and wire approaches nicely, and provided inspiration for the present work.

On a different front, in the 1940s and 50s, designs featuring helically wound conductors became popular for high-frequency antennas [44, pp. 265–339] as well as for slow-wave devices such as traveling-wave tubes [45, pp. 19–48, 229–232], and considerable modeling efforts were devoted to the understanding of their propagation characteristics. Unlike in the transmission-line problem, the field distributions had to be known accurately here, since they directly determine the radiation pattern of an antenna or the efficiency of interaction with a charged-particle stream. Of particular interest were the sheath helix and the tape helix models wherein the current-carrying surface is confined to a shell of infinitesimal thickness [46, 47, 48, 49, 50, 51], with *ad hoc* analytical devices employed to account for finite wire radius [52] (see also [45, pp. 34–43] or [53, pp. 306-308]). Textbook overviews of these efforts may be found in [54, pp. 40–45, 46–54, 77–82], [55, pp. 476–478], or [6, pp. 637–640]. Since the conductor surfaces of this geometry are separable in the cylindrical coordinate system, much progress could be made analytically in this case, especially toward obtaining the field distributions established around the helical conductor(s), though a fully satisfactory treatment eluded the early workers and did not appear until recently [56].

In addition to the field-theoretic models of uniform and twisted cable structures described above, it is possible to approach the problem from a circuit-theoretic viewpoint when one is interested only in the transmission-line modes of the cable. The twisted-pair cable, in particular, received this type of treatment extensively, ranging from a first-principles derivation of the equivalent-circuit equations [57] to the experimental characterization of equivalent-circuit parameters [58], the application of cascaded T-matrix approach on piece-wise uniform models whose parameters were calculated analytically [59, 60, 61] or numerically [62], finally to the treatment of finite wire radius by a numerical solution of the electric-field integral equation via the finite-element method [63]. This basic modeling approach was generalized recently to shielded-twisted-pair cable and validated experimentally [64].

1.3 Report overview

The development in this report blends and refines various elements of the analytical approaches mentioned above in an effort to obtain a highly accurate yet closed-form model of wave propagation on shielded-pair cables. The report consists of three main chapters. In §2, a physics-based model is developed for signal propagation along a cable consisting of two wires enclosed by a metallic shield. Specifically, the eigenvalues and the corresponding field distributions for the common and the differential transmission-line modes are derived. Amplitudes of forward- and backward-propagating modes are then obtained by considering sources and loads attached to the cable. The case of uniform wires is studied in some detail, and the results are subsequently extended to the case of twisted wires.

In §3, a careful series of first-principles simulations is undertaken to verify the theory of §2. By solving the exact electromagnetic field equations numerically for the same cable geometry, the assumptions made in obtaining the approximate analytical model are checked for validity and accuracy. Alternative geometries, which cannot be treated analytically, are also simulated to increase confidence in the applicability of the theoretical model to practical cable constructions. Finally, parameters for a preliminary fault model considered in §4 are obtained by simulating the effects of a hole in the shield.

In §4, a comprehensive framework is developed for extracting cable and fault parameters from experimental data. At the core of this framework is the S-parameter formalism for describing a multi-port system. Specifically, the theory of §2 is used to derive the S-parameters of nominal and faulty cable segments. Considerations of source and load effects and other features of the experimental setup lead finally to a combined measurement system model. The estimation of unknown cable and measurement device parameters from laboratory data is then couched as a Bayesian inference problem. The power of the overall modeling and inference approach is demonstrated on data from both nominal and faulty cables.

The main conclusions of the report are collected in §5.

Chapter 2

Theory

2.1 Basic model formulation

2.1.1 Cable specification

Consider the cross-section of an ideal shielded-pair cable, oriented along the z axis of a cylindrical coordinate system (ρ, ϕ, z), as shown in Fig. 2.1. The shield and the two (identical) wires are labeled "conductor 0," "conductor 1" and "conductor 2," respectively, the former having (outer) radius r_{s}, and the latter r_{w}. The space between the conductors is filled entirely with an homogeneous, isotropic insulator of radius r_{i}, having permittivity ϵ, permeability μ, and conductivity σ. The centers of the two wires are placed symmetrically on a circle of radius q. Contact between the conductors is avoided via the constraint $2r_{\mathsf{w}} < q + r_{\mathsf{w}} < r_{\mathsf{i}}$. The cable is insulated from the ambient medium by a jacket on the outside of the shield (not shown).

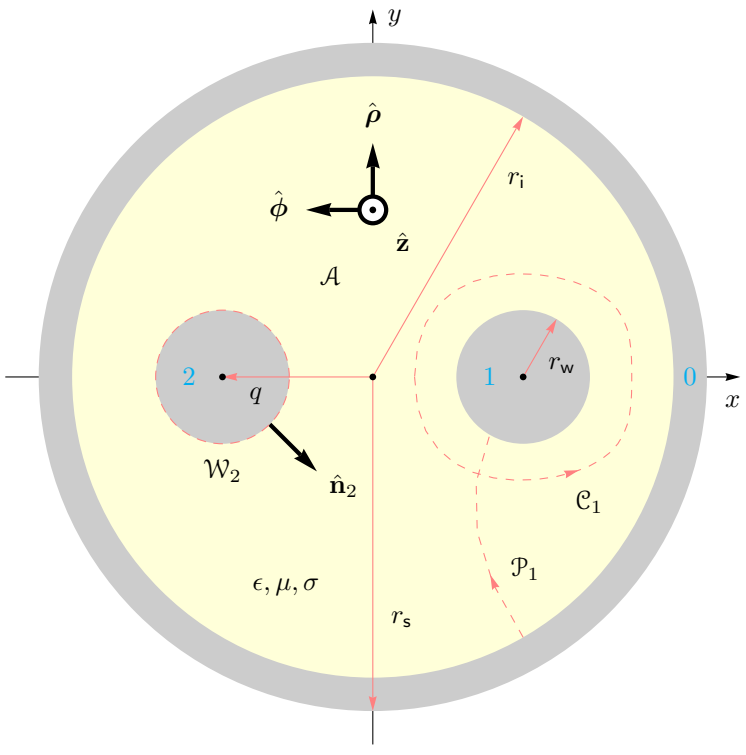

Figure 2.1: Shielded-pair waveguide cross-section.

If this cross-section is translated uniformly in the positive z direction, one obtains a *shielded-uniform-pair* (SUP) cable. If, during such translation, one simultaneously rotates the cross-section at a constant rate κ (rad/m) in the positive ϕ direction, a (right-handed) *shielded-twisted-pair* (STP) cable results, having a period $p = 2\pi/\kappa$ along the z axis. (This may be termed a "polar" twist; see [65] for a "toroidal" twist.) Figures and plots in this chapter are generated for a "typical" STP cable whose geometric and constitutive parameters are listed in Table 2.1.*

Table 2.1: Shielded-pair cable parameters.

Shield		**Wires**		**Insulator**	
Parameter	*Value*	*Parameter*	*Value*	*Parameter*	*Value*
r_{s}	1.5 mm	r_{w}	0.3 mm	r_{i}	1.35 mm
		p	30.0 mm	ϵ	$2.3\,\epsilon_0$
		q	0.675 mm	μ	$1.0\,\mu_0$
σ_{s}	$5.998\,10^7$ S/m	σ_{w}	$5.998\,10^7$ S/m	σ	0.0 S/m

2.1.2 Maxwell equations

With all the conductors initially assumed to be perfect, the electric and the magnetic fields within the insulator satisfy the (source-free) Maxwell equations

$$\boldsymbol{\nabla} \times \mathbf{E} = \mathrm{i}\omega\mu\mathbf{H}, \tag{2.1}$$

$$\boldsymbol{\nabla} \times \mathbf{H} = (\sigma - \mathrm{i}\omega\epsilon)\mathbf{E}. \tag{2.2}$$

A suitable basis and a coordinate system must be chosen in which to solve these equations. Among the two closest candidates, the polar and the bipolar coordinate systems [66, pp. 1175–1215], the former is preferred as it affords a more accurate representation of the fields near the shield. (Since the ultimate goal of the present work is to develop a physics-based algorithm for detecting faults in the *shield* of the cable, fields in the vicinity of the two conductors need not be modeled with great precision.) It then becomes necessary, as argued in §1.2, to approximate the wire cross-sections with a shape that is more amenable to analysis. It is judged that a pair of *filaments*, helically wound on a (fictitious) cylindrical shell of radius $r_{\mathsf{c}} \in (q - r_{\mathsf{w}}, q + r_{\mathsf{w}})$ and with period p, comes closest to mimicking, both qualitatively and quantitatively, the fields produced by the round wires. (Another possible choice, a pair of similarly wound *tapes* with "optimally chosen" thickness and width, has sharp features that produce large localized fields, which are uncharacteristic of the round wires.) As will be demonstrated in §2.2.3, a judicious choice for the filament radius helps retain the salient features of the proximity effect, which may be suspected, at first glance, to be thrown out by this approximation. Denoting by $i_j(z)$ the current flowing on the j^{th} filament, the (surface) current density on the shell at $\rho = r_{\mathsf{c}}$ containing the filaments may thus be written

$$\mathbf{K}(\phi, z) = \frac{\hat{\boldsymbol{\phi}}\,\kappa r_{\mathsf{c}} + \hat{\mathbf{z}}}{r_{\mathsf{c}}\sqrt{1 + (\kappa r_{\mathsf{c}})^2}} \left[i_1(z)\,\delta(\phi - \kappa z) + i_2(z)\,\delta(\phi - \kappa z - \pi) \right], \tag{2.3}$$

where $\delta(\cdot)$ denotes the Dirac delta function. This "surrogate" cable model is depicted in Fig. 2.2.

Taking the curl of (2.1), substituting from (2.2), and dot-multiplying by $\hat{\mathbf{z}}$, one obtains the Helmholtz equation

$$\nabla^2 E_{\parallel} + k^2 E_{\parallel} = 0, \tag{2.4}$$

*The *exact* vacuum permittivity and permeability are $\epsilon_0 = 8.85418781762\,10^{-12}$ F/m and $\mu_0 = 1.25663706143\,10^{-6}$ H/m, respectively. For frequencies in the microwave regime and below, the permittivity and the permeability of (nonmagnetic) metals are typically taken to have these values.

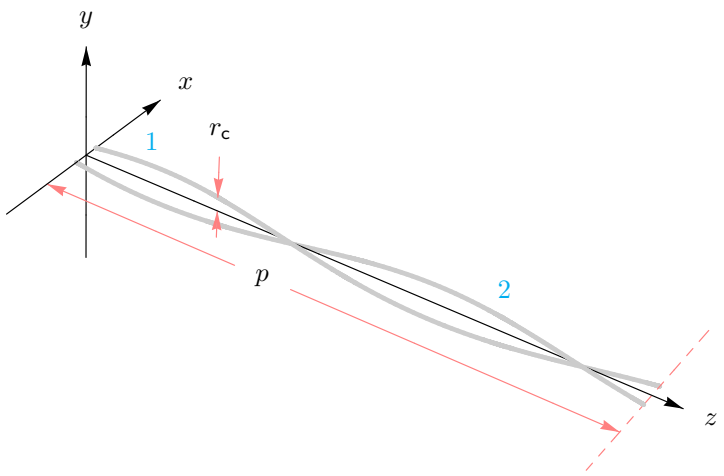

Figure 2.2: A pair of helically wound, current-carrying filaments inside a cylindrical shield (not shown).

where $k \equiv \sqrt{\mathrm{i}\omega\mu(\sigma - \mathrm{i}\omega\epsilon)}$ is the wavenumber in the insulator, and $\parallel$ denotes the axial component. Floquet's theorem dictates that the fields in an helically symmetric structure must have the form (see, *e.g.*, [67, p. 584])

$$E_{\parallel}(\mathbf{r}) = \sum_{m=-\infty}^{\infty} e_{\parallel m}(\rho)\, \mathrm{e}^{\mathrm{i}m(\phi-\kappa z)}\, \mathrm{e}^{\mathrm{i}\lambda z}. \tag{2.5}$$

Inserting (2.5) into (2.4), the radial dependence of the axial electric field is found to obey the Bessel equation

$$\frac{1}{\rho}\frac{\mathrm{d}}{\mathrm{d}\rho}\left(\rho\,\frac{\mathrm{d}e_{\parallel m}}{\mathrm{d}\rho}\right) - \left(\gamma_m^2 + \frac{m^2}{\rho^2}\right) e_{\parallel m} = 0, \tag{2.6}$$

where $\gamma_m \equiv \sqrt{(\lambda - m\kappa)^2 - k^2}$. This definition of the radial eigenvalue reflects the expectation that the phase velocity for the principal modes of interest should be slightly less than that in the unbounded insulator. Elimination of the electric field from (2.1) and (2.2) leads to a similar representation for the axial magnetic field.

Next, cross-multiplying (2.1) and (2.2) with $\hat{\mathbf{z}}$ on the left, one obtains

$$\frac{\partial \mathbf{E}_{\perp}}{\partial z} = \boldsymbol{\nabla}_{\perp} E_{\parallel} - \mathrm{i}\omega\mu\, \hat{\mathbf{z}} \times \mathbf{H}_{\perp}, \tag{2.7}$$

$$\frac{\partial \mathbf{H}_{\perp}}{\partial z} = \boldsymbol{\nabla}_{\perp} H_{\parallel} - (\sigma - \mathrm{i}\omega\epsilon)\, \hat{\mathbf{z}} \times \mathbf{E}_{\perp}, \tag{2.8}$$

where $\perp$ denotes the transverse component. Substituting Floquet expansions of the form (2.5) for all the field components, (2.7) and (2.8) are transformed into

$$\mathrm{i}(\lambda - m\kappa)\mathbf{e}_{\perp m} = \hat{\boldsymbol{\rho}}\,\frac{\mathrm{d}e_{\parallel m}}{\mathrm{d}\rho} + \hat{\boldsymbol{\phi}}\,\frac{\mathrm{i}m}{\rho}\,e_{\parallel m} - \mathrm{i}\omega\mu\,\hat{\mathbf{z}} \times \mathbf{h}_{\perp m},$$

$$\mathrm{i}(\lambda - m\kappa)\mathbf{h}_{\perp m} = \hat{\boldsymbol{\rho}}\,\frac{\mathrm{d}h_{\parallel m}}{\mathrm{d}\rho} + \hat{\boldsymbol{\phi}}\,\frac{\mathrm{i}m}{\rho}\,h_{\parallel m} - (\sigma - \mathrm{i}\omega\epsilon)\,\hat{\mathbf{z}} \times \mathbf{e}_{\perp m}.$$

Solving for $\mathbf{e}_{\perp m}$ and $\mathbf{h}_{\perp m}$, one finally obtains

$$\mathbf{e}_{\perp m} = \frac{1}{\gamma_m^2}\left[\mathrm{i}\omega\mu\left(\hat{\boldsymbol{\phi}}\,\frac{\mathrm{d}h_{\parallel m}}{\mathrm{d}\rho} - \hat{\boldsymbol{\rho}}\,\frac{\mathrm{i}m}{\rho}\,h_{\parallel m}\right) - \mathrm{i}(\lambda - m\kappa)\left(\hat{\boldsymbol{\rho}}\,\frac{\mathrm{d}e_{\parallel m}}{\mathrm{d}\rho} + \hat{\boldsymbol{\phi}}\,\frac{\mathrm{i}m}{\rho}\,e_{\parallel m}\right)\right], \tag{2.9}$$

$$\mathbf{h}_{\perp m} = \frac{1}{\gamma_m^2}\left[(\sigma - \mathrm{i}\omega\epsilon)\left(\hat{\boldsymbol{\phi}}\,\frac{\mathrm{d}e_{\parallel m}}{\mathrm{d}\rho} - \hat{\boldsymbol{\rho}}\,\frac{\mathrm{i}m}{\rho}\,e_{\parallel m}\right) - \mathrm{i}(\lambda - m\kappa)\left(\hat{\boldsymbol{\rho}}\,\frac{\mathrm{d}h_{\parallel m}}{\mathrm{d}\rho} + \hat{\boldsymbol{\phi}}\,\frac{\mathrm{i}m}{\rho}\,h_{\parallel m}\right)\right], \tag{2.10}$$

giving the transverse field components in terms of the axial ones.

2.1.3 Field solutions

For the "interior" region ($0 \le \rho < r_{\mathsf{c}}$), the requirement of finiteness at $\rho = 0$ leads for (2.6) to the solutions

$$e^{\mathsf{in}}_{\parallel m}(\rho) \;=\; A^{\mathsf{in}}_m \, I_m(\gamma_m \rho), \tag{2.11}$$

$$h^{\mathsf{in}}_{\parallel m}(\rho) \;=\; B^{\mathsf{in}}_m \, I_m(\gamma_m \rho). \tag{2.12}$$

For the "exterior" region ($r_{\mathsf{c}} < \rho \le r_{\mathsf{i}}$), on the other hand, the requirement of vanishing axial and azimuthal electric fields, and therefore $e_{\parallel m}$ and $\mathrm{d}h_{\parallel m}/\mathrm{d}\rho$, on the shield at $\rho = r_{\mathsf{i}}$ leads to

$$e^{\mathsf{ex}}_{\parallel m}(\rho) \;=\; A^{\mathsf{ex}}_m \left[I_m(\gamma_m \rho) - \frac{I_m(\gamma_m r_{\mathsf{i}})}{K_m(\gamma_m r_{\mathsf{i}})} \, K_m(\gamma_m \rho) \right], \tag{2.13}$$

$$h^{\mathsf{ex}}_{\parallel m}(\rho) \;=\; B^{\mathsf{ex}}_m \left[I_m(\gamma_m \rho) - \frac{I'_m(\gamma_m r_{\mathsf{i}})}{K'_m(\gamma_m r_{\mathsf{i}})} \, K_m(\gamma_m \rho) \right]. \tag{2.14}$$

In these solutions, $I_m(\cdot)$ and $K_m(\cdot)$ denote the modified Bessel functions of the first and the second kinds, respectively, while $'$ signifies differentiation with respect to argument.

The unknown coefficients in (2.11) through (2.14) are now determined by imposing the continuity conditions

$$\hat{\boldsymbol{\rho}} \times (\mathbf{E}^{\mathsf{ex}} - \mathbf{E}^{\mathsf{in}}) \;=\; \mathbf{0}, \tag{2.15}$$

$$\hat{\boldsymbol{\rho}} \times (\mathbf{H}^{\mathsf{ex}} - \mathbf{H}^{\mathsf{in}}) \;=\; \mathbf{K} \tag{2.16}$$

across the current shell at $\rho = r_{\mathsf{c}}$. Toward this end, (2.3) is put into a more useful form by defining the helix pitch angle $\psi \equiv \cot^{-1}(\kappa r)$, substituting $i_j(z) = I_j \, \mathrm{e}^{\mathrm{i}\lambda z}$ to endow the mode currents with the same axial dependence as the mode fields they support, and making use of the identity $\delta(\phi) = 1/(2\pi) \sum_{m=-\infty}^{\infty} \mathrm{e}^{\mathrm{i}m\phi}$ to acquire the Floquet form, resulting in

$$\mathbf{K}(\phi, z) = \frac{\hat{\boldsymbol{\phi}} \cos\psi + \hat{\mathbf{z}} \sin\psi}{2\pi r_{\mathsf{c}}} \sum_{m=-\infty}^{\infty} \left[I_1 + (-1)^m \, I_2 \right] \mathrm{e}^{\mathrm{i}m(\phi - \kappa z)} \, \mathrm{e}^{\mathrm{i}\lambda z}. \tag{2.17}$$

The application of (2.15) leads immediately to

$$A^{\mathsf{in}}_m \;=\; A^{\mathsf{ex}}_m \left[1 - \frac{I_m(\gamma_m r_{\mathsf{i}})}{K_m(\gamma_m r_{\mathsf{i}})} \, \frac{K_m(\gamma_m r_{\mathsf{c}})}{I_m(\gamma_m r_{\mathsf{c}})} \right], \tag{2.18}$$

$$B^{\mathsf{in}}_m \;=\; B^{\mathsf{ex}}_m \left[1 - \frac{I'_m(\gamma_m r_{\mathsf{i}})}{K'_m(\gamma_m r_{\mathsf{i}})} \, \frac{K'_m(\gamma_m r_{\mathsf{c}})}{I'_m(\gamma_m r_{\mathsf{c}})} \right]. \tag{2.19}$$

The application of (2.16), with the use of (2.17), (2.18), and (2.19), then yields

$$A^{\mathsf{ex}}_m \;=\; \frac{K_m(\gamma_m r_{\mathsf{i}})}{I_m(\gamma_m r_{\mathsf{i}})} \, I_m(\gamma_m r_{\mathsf{c}}) \, \frac{m(\lambda - m\kappa)\cos\psi + \gamma_m^2 r_{\mathsf{c}} \sin\psi}{2\pi r_{\mathsf{c}}(\sigma - \mathrm{i}\omega\epsilon)} \left[I_1 + (-1)^m \, I_2 \right], \tag{2.20}$$

$$B^{\mathsf{ex}}_m \;=\; \frac{K'_m(\gamma_m r_{\mathsf{i}})}{I'_m(\gamma_m r_{\mathsf{i}})} \, I'_m(\gamma_m r_{\mathsf{c}}) \, \frac{\gamma_m \cos\psi}{2\pi} \left[I_1 + (-1)^m \, I_2 \right], \tag{2.21}$$

where use was made of the Wronskian $I'_m(x) \, K_m(x) - I_m(x) \, K'_m(x) = 1/x$.

2.1.4 Eigenvalue equation

Finally, the heretofore unknown axial eigenvalue λ must be determined by imposing the remaining boundary condition of vanishing tangential electric field on the two filaments; *viz.*,

$$(\hat{\boldsymbol{\phi}} \cos\psi + \hat{\mathbf{z}} \sin\psi) \cdot \mathbf{E} = 0 \tag{2.22}$$

at $\rho = r_{\mathsf{c}}$, $\phi = \kappa z$ *and* $\phi = \kappa z + \pi$. Substituting from (2.9) through (2.12) and then from (2.18) through (2.21), one obtains from (2.22) the linear system

$$\sum_{m=-\infty}^{\infty} \begin{bmatrix} 1 & (-1)^m \\ (-1)^m & 1 \end{bmatrix} \begin{bmatrix} I_1 \\ I_2 \end{bmatrix} S_m(\omega, \lambda) = \mathbf{0}, \tag{2.23}$$

where

$$\begin{aligned} S_m(\omega, \lambda) = &\left[\left(\frac{\lambda}{k}\right)^2 - 1 + \left(\frac{m\kappa}{\gamma_m}\right)^2 \right] [I_m(\gamma_m r_{\mathsf{c}})]^2 \left[\frac{K_m(\gamma_m r_{\mathsf{i}})}{I_m(\gamma_m r_{\mathsf{i}})} - \frac{K_m(\gamma_m r_{\mathsf{c}})}{I_m(\gamma_m r_{\mathsf{c}})} \right] \\ &+ (\kappa r_{\mathsf{c}})^2 [I'_m(\gamma_m r_{\mathsf{c}})]^2 \left[\frac{K'_m(\gamma_m r_{\mathsf{i}})}{I'_m(\gamma_m r_{\mathsf{i}})} - \frac{K'_m(\gamma_m r_{\mathsf{c}})}{I'_m(\gamma_m r_{\mathsf{c}})} \right]. \end{aligned} \tag{2.24}$$

The two nontrivial solutions of (2.23) are readily identified; *viz.*,

$$\begin{aligned} I_2 = I_1 \quad &\Rightarrow \quad \textit{even} \text{ (or longitudinal) mode,} \\ I_2 = -I_1 \quad &\Rightarrow \quad \textit{odd} \text{ (or balanced) mode.} \end{aligned}$$

The eigenvalue equation, from which the permissible values of λ are to be solved for, is therefore given by

$$\Lambda(\omega, \lambda) = \sum_{m=-\infty}^{\infty} [1 \pm (-1)^m] \, S_m(\omega, \lambda) = 0, \tag{2.25}$$

where the top (bottom) sign corresponds to the even (odd) mode. Quantities pertaining to the even and the odd modes will be indicated throughout by the subscripts e and o, respectively.

2.2 Uniform cable

2.2.1 Eigenvalues

In the limit $p \to \infty$, the waveguide geometry reduces to that of SUP cable. Setting $\kappa = 0$, (2.25) becomes

$$\Lambda(\omega, \lambda) = \left[\left(\frac{\lambda}{k}\right)^2 - 1 \right] \underbrace{\sum_{m=-\infty}^{\infty} [1 \pm (-1)^m] \, [I_m(\gamma r_{\mathsf{c}})]^2 \left[\frac{K_m(\gamma r_{\mathsf{i}})}{I_m(\gamma r_{\mathsf{i}})} - \frac{K_m(\gamma r_{\mathsf{c}})}{I_m(\gamma r_{\mathsf{c}})} \right]}_{\Omega(\omega, \lambda)} = 0, \tag{2.26}$$

where $\gamma \equiv \sqrt{\lambda^2 - k^2}$. Evidently, $\lambda = \pm k$ satisfy the eigenvalue equation for both the even and the odd modes of SUP cable. As will be shown in §2.2.2, the mode fields corresponding to these eigenvalues are transverse-electromagnetic (TEM). These are, of course, none other than the two degenerate *transmission-line* modes of this uniform three-conductor structure. The remaining roots of (2.26), due to the zeros of the factor $\Omega(\omega, \lambda)$, correspond to mode fields that are transverse-magnetic, transverse-electric, or possibly hybrid in nature. The cut-off frequencies of these *waveguide* modes may be obtained as the zeros of the function $\Omega(\omega, 0)$, which is plotted against linear frequency $f = \omega/(2\pi)$ in Fig. 2.3 using the parameter values in Table 2.1 and the optimal filament radii to be found in §2.2.3. Specifically, it is observed that the lowest-order even (odd) mode is cut off below roughly 67 GHz (103 GHz). Clearly, none of the waveguide modes can propagate over the spectral region of typical operation for a cable, and therefore they need not be studied here.

2.2.2 Mode fields

With $\psi = \pi/2$, one has from §2.1.3 that

$$e_{\parallel m}(\rho) = I_m(\gamma \rho_<) \, I_m(\gamma \rho_>) \left[\frac{K_m(\gamma r_{\mathsf{i}})}{I_m(\gamma r_{\mathsf{i}})} - \frac{K_m(\gamma \rho_>)}{I_m(\gamma \rho_>)} \right] \frac{\gamma^2 I}{2\pi(\sigma - \mathrm{i}\omega\epsilon)} \, [1 \pm (-1)^m], \tag{2.27}$$

$$h_{\parallel m}(\rho) = 0, \tag{2.28}$$

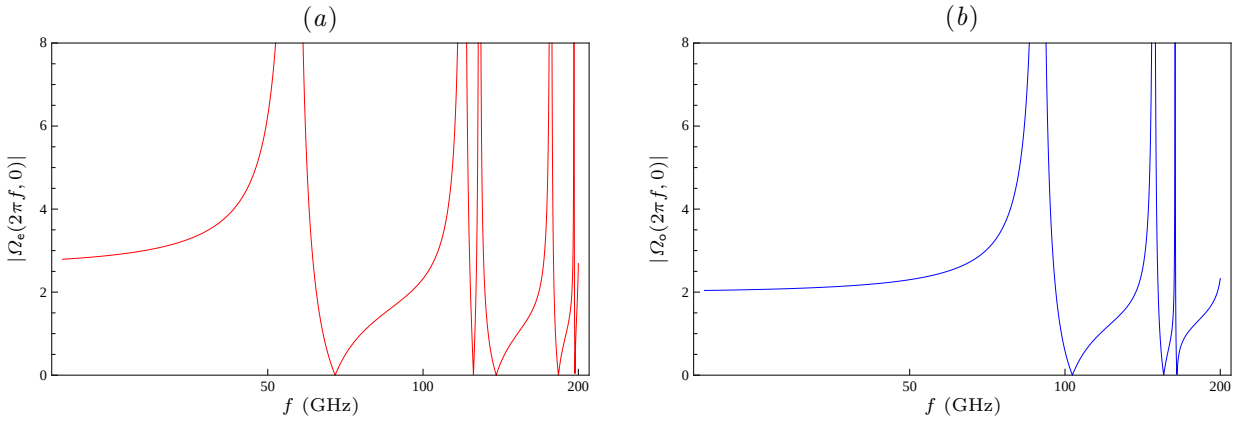

Figure 2.3: Cut-off frequencies of the even (a) and the odd (b) waveguide modes of SUP cable.

where $\rho_<$ ($\rho_>$) denotes the lesser (greater) of r_c and ρ, and I is the current flowing on filament 1. In the limit $\gamma \to 0$, small-argument approximations for Bessel functions [68, p. 375] reveal that $e_{\parallel m}$ also tends to zero, leading to $E_\parallel = H_\parallel = 0$ everywhere; *i.e.*, the even and the odd modes corresponding to $\lambda = \pm k$ are both TEM.

Now, with (2.28) holding identically, the transverse fields (2.9) and (2.10) become

$$\mathbf{e}_{\perp m}(\rho) = -\frac{\mathrm{i}\lambda}{\gamma^2}\left(\hat{\boldsymbol{\rho}}\,\frac{\mathrm{d}e_{\parallel m}}{\mathrm{d}\rho} + \hat{\boldsymbol{\phi}}\,\frac{\mathrm{i}m}{\rho}\,e_{\parallel m}\right),$$
$$\mathbf{h}_{\perp m}(\rho) = \frac{\sigma - \mathrm{i}\omega\epsilon}{\gamma^2}\left(\hat{\boldsymbol{\phi}}\,\frac{\mathrm{d}e_{\parallel m}}{\mathrm{d}\rho} - \hat{\boldsymbol{\rho}}\,\frac{\mathrm{i}m}{\rho}\,e_{\parallel m}\right).$$

Substituting from (2.27) and subsequently into the Floquet series for transverse fields, one obtains

$$\mathbf{E}_\perp(\mathbf{r}) = -\boldsymbol{\nabla}_\perp \Phi(\mathbf{r}_\perp)\,\mathrm{e}^{\pm\mathrm{i}kz}, \tag{2.29}$$
$$\mathbf{H}_\perp(\mathbf{r}) = \pm\mathrm{i}\,\frac{\sigma - \mathrm{i}\omega\epsilon}{k}\,\hat{\mathbf{z}} \times \mathbf{E}_\perp(\mathbf{r}), \tag{2.30}$$

where, passing to the limit $\lambda \to \pm k$ using small-argument approximations for Bessel functions and making use of the expansion $\ln(1 + x^2 - 2x\cos\phi) = -2\sum_{m=1}^{\infty}(x^m/m)\cos(m\phi)$, valid for $|x| \le 1$,

$$\Phi(\mathbf{r}_\perp) = -\frac{\mathrm{i}k|I|}{4\pi(\sigma - \mathrm{i}\omega\epsilon)}\underbrace{\left\{\ln\left[\frac{r_\mathsf{i}^4 + (r_\mathsf{c}\rho)^2 - 2r_\mathsf{i}^2 r_\mathsf{c}\rho\cos\phi}{r_\mathsf{i}^2(\rho^2 + r_\mathsf{c}^2 - 2r_\mathsf{c}\rho\cos\phi)}\right] \pm \ln\left[\frac{r_\mathsf{i}^4 + (r_\mathsf{c}\rho)^2 + 2r_\mathsf{i}^2 r_\mathsf{c}\rho\cos\phi}{r_\mathsf{i}^2(\rho^2 + r_\mathsf{c}^2 + 2r_\mathsf{c}\rho\cos\phi)}\right]\right\}}_{F(\mathbf{r}_\perp)}. \tag{2.31}$$

It should be noted that the upper (lower) signs in (2.29) and (2.30) refer to forward (backward) propagation, whereas those in (2.31) refer to the even (odd) mode. Aside from the prefactor, the function Φ is, of course, nothing but the (electrostatic) potential due to two charges of same or opposite polarity fixed symmetrically on a circle of radius r_c inside a metallic cylinder of radius r_i (see, *e.g.*, [12, p. 90]). Noting that I changes sign with the direction of propagation, it is observed that the field components obtained above conform to the sign convention of the standard normal-mode formalism (see, *e.g.*, [12, p. 390]).

The potential distributions for the two TEM modes are shown in Fig. 2.4, plotted using the optimal filament radii to be found in §2.2.3. The filament current I is chosen (arbitrarily) to produce unit average potential on conductor 1 in both cases (see Fig. 2.8). Consequently, the average potential on conductor 2 is $+1$ V (-1 V) for the even (odd) mode, while the exact potential on the shield is zero in both cases. Note that the potentials are plotted only over the insulator, since (2.31) is *not* valid within the wires.

The azimuthal distributions of charge on the conductor walls reveal the extent to which the proximity effect may be expected to play a role in the subsequent determination of equivalent circuit parameters for the cable, as detailed in §2.3. On the j^{th} conductor at, say, $z = 0$, one has the surface charge density

$$\Sigma_j = -\epsilon\,\hat{\mathbf{n}}_j \cdot \boldsymbol{\nabla}_\perp \Phi(\mathcal{W}_j), \tag{2.32}$$

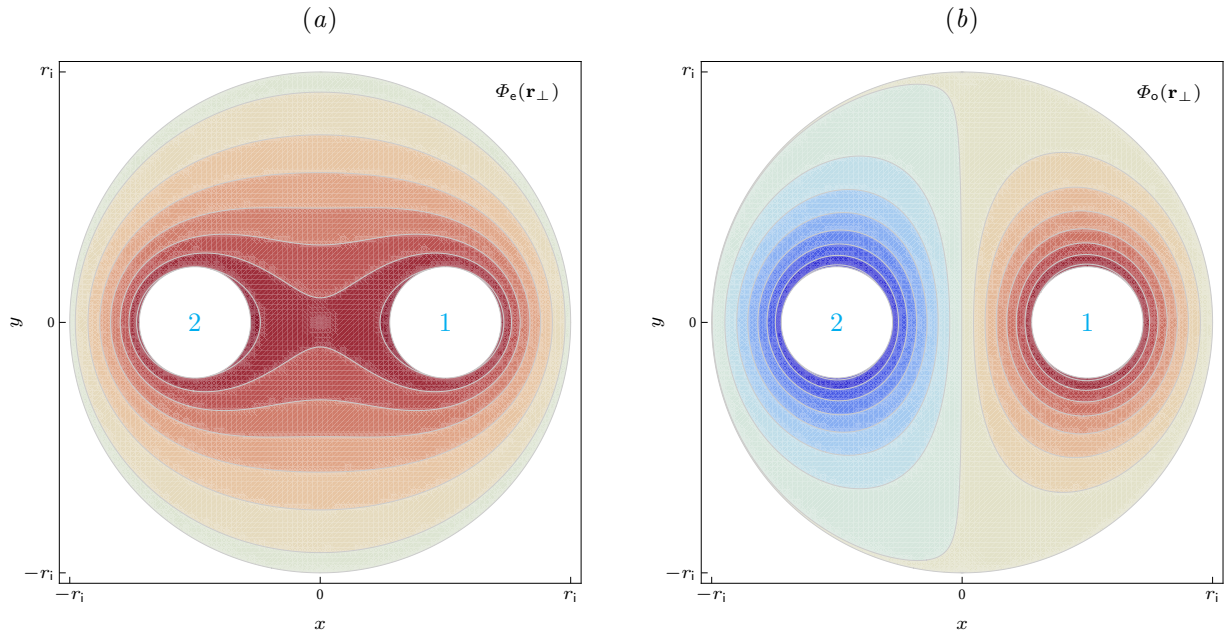

Figure 2.4: Potential distributions for the even (a) and the odd (b) modes of SUP cable; the vertical range is $[0, 1]$ V in (a) and $[-1, 1]$ V in (b), with shades of red (blue) indicating positive (negative) values.

which may be evaluated analytically by direct substitution from (2.31) into (2.32), preceded, where necessary, by a change of coordinates via (2.35) and (2.36). These charge densities are displayed in Fig. 2.5, using the same value for I as in Fig. 2.4. It is observed that the charge densities are highly nonuniform around the conductor walls.

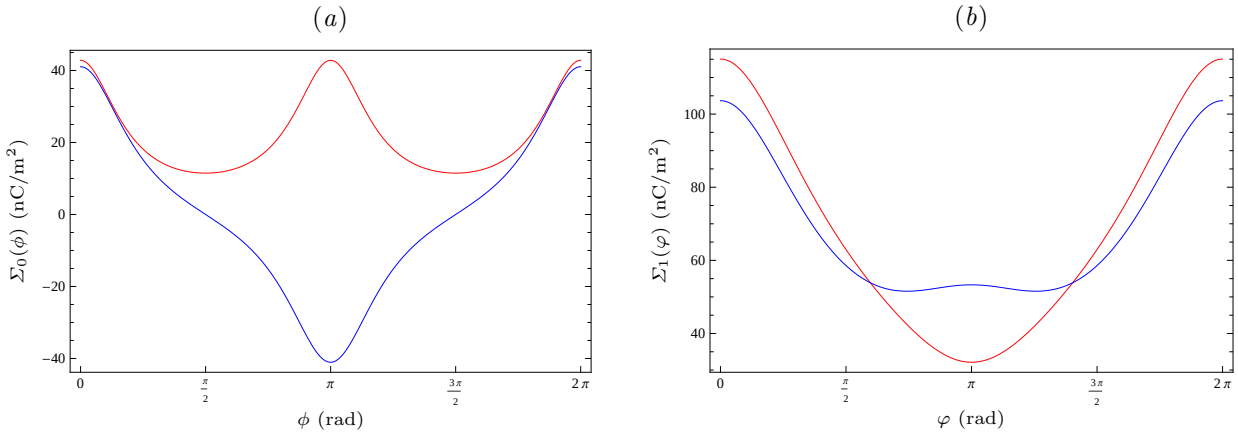

Figure 2.5: Surface charge distributions on the shield (a) and on conductor 1 (b) for the even (red) and the odd (blue) modes of SUP cable.

Substituting (2.31) into (2.29), the corresponding electric field is readily calculated, obtaining

$$\mathbf{E}_\perp(\mathbf{r}) = \frac{\mathrm{i}k|I|\,\mathrm{e}^{\pm\mathrm{i}kz}}{2\pi(\sigma-\mathrm{i}\omega\epsilon)}\left\{\hat{\boldsymbol{\rho}}\left[\frac{r_\mathsf{c}^2\rho - r_\mathsf{i}^2 r_\mathsf{c}\cos\phi}{r_\mathsf{i}^4+(r_\mathsf{c}\rho)^2-2r_\mathsf{i}^2 r_\mathsf{c}\rho\cos\phi} - \frac{\rho - r_\mathsf{c}\cos\phi}{\rho^2+r_\mathsf{c}^2-2r_\mathsf{c}\rho\cos\phi}\right.\right.$$
$$\left. \pm \frac{r_\mathsf{c}^2\rho + r_\mathsf{i}^2 r_\mathsf{c}\cos\phi}{r_\mathsf{i}^4+(r_\mathsf{c}\rho)^2+2r_\mathsf{i}^2 r_\mathsf{c}\rho\cos\phi} \mp \frac{\rho + r_\mathsf{c}\cos\phi}{\rho^2+r_\mathsf{c}^2+2r_\mathsf{c}\rho\cos\phi}\right]$$
$$+\hat{\boldsymbol{\phi}}\left[\frac{r_\mathsf{i}^2 r_\mathsf{c}\sin\phi}{r_\mathsf{i}^4+(r_\mathsf{c}\rho)^2-2r_\mathsf{i}^2 r_\mathsf{c}\rho\cos\phi} - \frac{r_\mathsf{c}\sin\phi}{\rho^2+r_\mathsf{c}^2-2r_\mathsf{c}\rho\cos\phi}\right.$$
$$\left.\left. \mp \frac{r_\mathsf{i}^2 r_\mathsf{c}\sin\phi}{r_\mathsf{i}^4+(r_\mathsf{c}\rho)^2+2r_\mathsf{i}^2 r_\mathsf{c}\rho\cos\phi} \pm \frac{r_\mathsf{c}\sin\phi}{\rho^2+r_\mathsf{c}^2+2r_\mathsf{c}\rho\cos\phi}\right]\right\}. \tag{2.33}$$

The (rectangular) electric-field components of the two modes are shown in Fig. 2.6. The magnetic field is related trivially to the electric field via (2.30), and need not be exhibited explicitly.

2.2.3 Choice of r_c

The optimal radius r_c for the filament pair in Fig. 2.2 will now be determined by imposing the "proper" boundary condition

$$\hat{\mathbf{n}}_j \times \mathbf{E}(\mathcal{W}_j) = \mathbf{0}, \tag{2.34}$$

rather than (2.22), on the round wires, where $\mathcal{W}_j$ denotes the bounding wall of the j^{th} conductor with outward unit normal $\hat{\mathbf{n}}_j$ (see Fig. 2.1). In view of (2.29), (2.34) implies that Φ must be constant on $\mathcal{W}_j$; the value of r_c will be chosen to achieve this as closely as possible for each mode.

Owing to the symmetry of the cable cross-section, it is sufficient to impose (2.34) on only one of the conductor surfaces. With (ϱ,φ) denoting the local polar coordinates around conductor 1 (see Fig. 2.7), one has that

$$\rho^2 = \varrho^2 + q^2 + 2q\varrho\cos\varphi, \tag{2.35}$$
$$\rho\cos\phi = q + \varrho\cos\varphi. \tag{2.36}$$

Substituting into (2.31) and subsequently expanding into a Fourier series in φ, one obtains

$$\Phi(\varrho,\varphi) = -\frac{\mathrm{i}k|I|}{4\pi(\sigma-\mathrm{i}\omega\epsilon)}\left\{\ln\left(\frac{R}{\varrho}\right)^2 - \sum_{m=1}^{\infty}\frac{2}{m}\left[\left(\frac{r_\mathsf{c}\varrho}{r_\mathsf{i}^2-qr_\mathsf{c}}\right)^m - \left(\frac{r_\mathsf{c}-q}{\varrho}\right)^m\right.\right.$$
$$\left.\left. \pm\left(-\frac{r_\mathsf{c}\varrho}{r_\mathsf{i}^2+qr_\mathsf{c}}\right)^m \mp \left(-\frac{\varrho}{r_\mathsf{c}+q}\right)^m\right]\cos(m\varphi)\right\}, \tag{2.37}$$

valid for $r_\mathsf{w} \le \varrho \le \min(q, r_\mathsf{i}-q)$, where

$$R_\mathsf{e} = \frac{r_\mathsf{i}^4-(qr_\mathsf{ce})^2}{(r_\mathsf{ce}+q)r_\mathsf{i}^2}, \tag{2.38}$$
$$R_\mathsf{o} = \frac{(r_\mathsf{co}+q)(r_\mathsf{i}^2-qr_\mathsf{co})}{(r_\mathsf{i}^2+qr_\mathsf{co})}. \tag{2.39}$$

Among possible strategies for choosing r_c, setting the amplitude of the first (azimuthal) harmonic of $\Phi(r_\mathsf{w},\varphi)$ to zero gives arguably the most satisfying result. This strategy leads from (2.37) to a quartic equation for r_c, whose analytic solution is too unwieldy to write down (see, *e.g.*, [69, p. 23]); approximate solutions, accurate to first order in the small quantity $(r_\mathsf{c}-q)$, are found to be

$$r_\mathsf{ce} = \frac{r_\mathsf{w}^2(r_\mathsf{i}^4-3q^4)+2q^2(r_\mathsf{i}^4-q^4)}{2q(r_\mathsf{i}^4-q^4-4r_\mathsf{w}^2q^2)},$$
$$r_\mathsf{co} = \frac{r_\mathsf{w}^2(r_\mathsf{i}^2+q^2)^2-2q^2(r_\mathsf{i}^4-q^4)}{2q\left[r_\mathsf{w}^2(3r_\mathsf{i}^2+q^2)-r_\mathsf{i}^4+q^4\right]}.$$

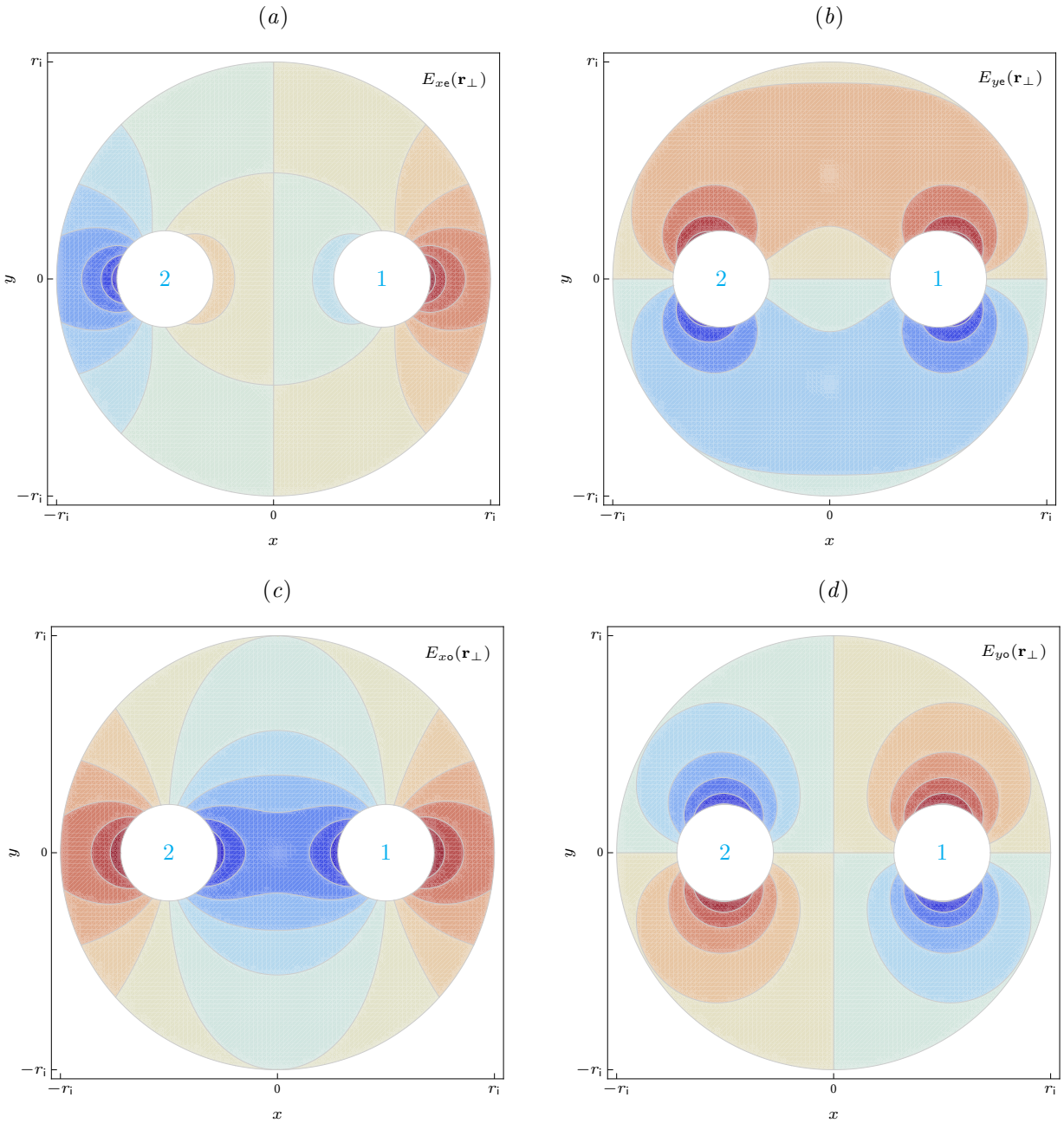

Figure 2.6: Electric-field distributions for the even (a and b) and the odd (c and d) modes of SUP cable; the vertical range is $[-5, 5]$ kV/m in all the plots.

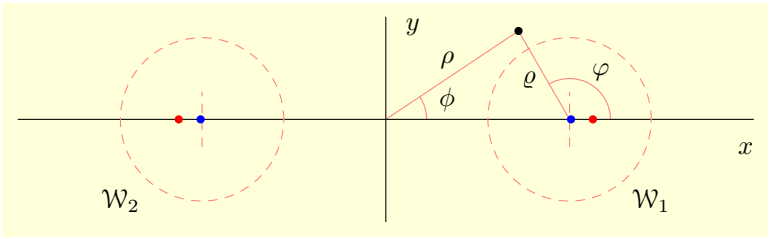

Figure 2.7: Optimal filament positions for the even (red) and the odd (blue) modes of SUP cable; the dashed vertical lines indicate the centers of the two wires.

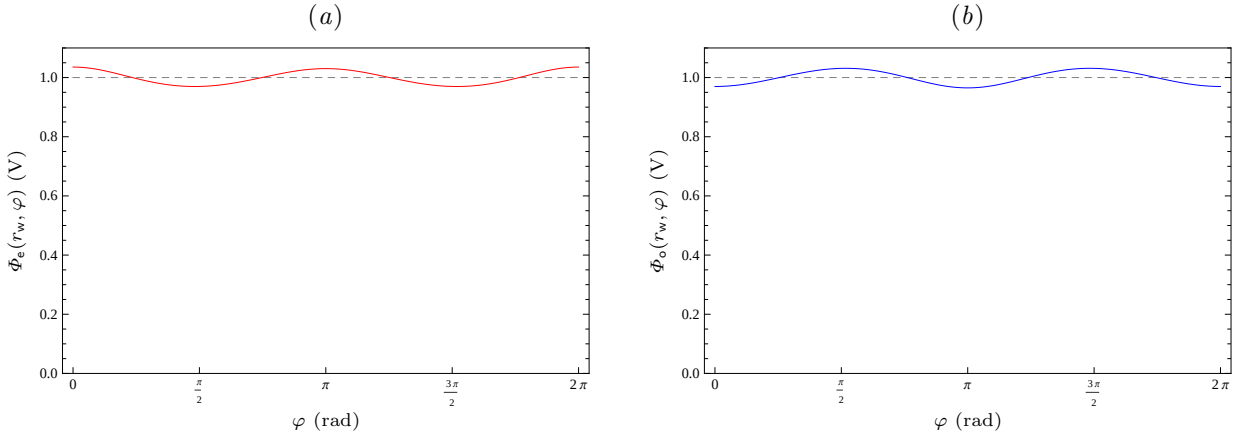

Figure 2.8: Variation of the approximate potential (2.37) on the periphery of conductor 1 for the even (a) and the odd (b) modes of SUP cable.

For the parameter values in Table 2.1, the above expressions give $r_{ce} = 0.773523$ mm and $r_{co} = 0.680362$ mm, while the corresponding exact values found numerically are $r_{ce} = 0.760679$ mm and $r_{co} = 0.680347$ mm. These latter filament positions are indicated in Fig. 2.7. With the (exact) numerical values of r_c inserted into (2.37), the variation in the potential on $\mathcal{W}_1$, defined as the ratio of the amplitude of the second harmonic to $\ln(R/\varrho)^2$ at $\varrho = r_w$,[†] is found to be around 3 % (see Fig. 2.8). Other conceivable strategies—*e.g.*, choosing r_c to jointly minimize the first two harmonics, introducing a second pair of filaments, *etc.*—do not yield an appreciable improvement over the simpler strategy adopted here.

2.2.4 Exact potentials

Since $\boldsymbol{\nabla} \cdot (\boldsymbol{\nabla} \times \mathbf{V}) = 0$ for any vector $\mathbf{V}$, it follows from (2.2) that $\boldsymbol{\nabla} \cdot \mathbf{E} = 0$. Substituting from (2.31), it is seen that the potential must satisfy the Laplace equation in the insulator; *viz.*,

$$\nabla_\perp^2 \Phi(\mathbf{r}_\perp) = 0 \quad \text{for} \quad \mathbf{r}_\perp \in \mathcal{A}. \tag{2.40}$$

In keeping with the convention established in §2.2.2, (2.40) is to be solved under the boundary conditions

$$\begin{aligned} \Phi(\mathcal{W}_0) &= 0, \\ \Phi(\mathcal{W}_1) &= +1, \\ \Phi(\mathcal{W}_2) &= \pm 1. \end{aligned}$$

This task may be performed numerically via the relaxation method (see, *e.g.*, [70, pp. 1059–1066]). Toward this end, a 2.5-μm resolution Cartesian mesh with a total of 825,559 grid points is constructed over the insulator. The analytical approximation (2.31) is used to generate initial guesses, and the grid-point potential values are then relaxed using the Gauss–Seidel iteration with Chebyshev acceleration. The direction

[†]The amplitudes of the higher-order harmonics in (2.37) are more than 10 times smaller than that of the second harmonic.

of grid traversal is alternated between successive iterations. Updates are computed at each grid point as an optimal blend of "+" and "×" averages over the nearest neighbors, as described in JACKSON [12, pp. 47–50]. Iterations are terminated when the largest update becomes smaller than 10^{-3}; convergence is achieved in under 20 iterations for each mode. Results of this computation are displayed in Fig. 2.9 as slices along the coordinate axes, showing excellent agreement, particularly away from the two wires, with the approximate analytical potentials (2.31).

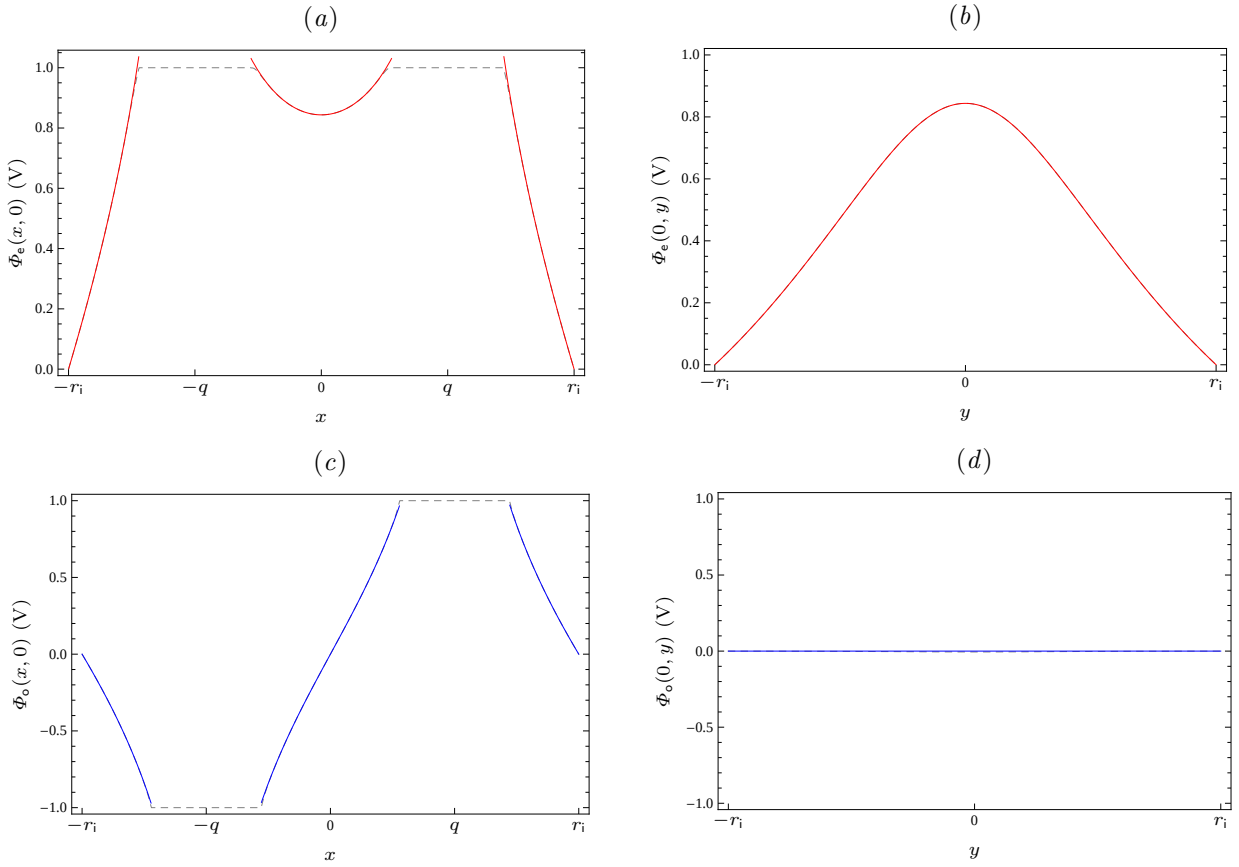

Figure 2.9: Comparison along the x and the y axes of the approximate analytical (solid curves) and the exact numerical (dashed curves) solutions for the even (a and b) and the odd (c and d) mode potentials of SUP cable.

2.3 Equivalent circuit model

2.3.1 Basic variables

Although the foregoing model of SUP cable in terms of electromagnetic fields is fundamental and self-contained, a "reduced" model involving voltage and current affords greater ease in describing the interconnection of the cable with external circuits (see, *e.g.*, [67, pp. 72–96]), as well as allowing for the inclusion of the effects of finite metallic conductivity in a relatively simple way. Furthermore, the twist rate in typical STP cables is extremely small, and one may therefore reasonably expect that the circuit-theoretic approach developed here can also be used profitably in modeling the STP cable.

Owing to the absence of axial field components for the transmission-line modes, conductor voltages v_j and currents i_j may be defined uniquely from (2.1) and (2.2) using Stokes' theorem in the usual way. For

the j^{th} conductor,[‡] then, one has

$$v_j(z) = -\int_{\mathcal{P}_j} \mathbf{E}(\mathbf{r}_\perp, z) \cdot \mathrm{d}\mathbf{l}, \tag{2.41}$$

$$i_j(z) = \oint_{\mathcal{C}_j} \mathbf{H}(\mathbf{r}_\perp, z) \cdot \mathrm{d}\mathbf{l}, \tag{2.42}$$

where $\mathcal{P}_j$ is an arbitrary contour in the transverse plane that originates from the shield and terminates on the surface of the j^{th} conductor, and $\mathcal{C}_j$ is an arbitrary closed contour in the transverse plane that circumscribes, in the positive sense, the j^{th} conductor (see Fig. 2.1). The shield voltage and current are, by definition,

$$\begin{aligned} v_0(z) &= 0, \\ i_0(z) &= -\sum_j i_j(z). \end{aligned}$$

One could substitute from (2.29) and (2.30) into (2.41) and (2.42) to obtain the conductor voltages and currents directly from the field-theoretic model of §2.2, but it is instructive to develop the circuit-theoretic model in its own right. In particular, it will be seen below that the same two transmission-line modes found before will emerge from this formulation as well. Contact must, of course, be made eventually with the field-theoretic model in order to obtain the line parameters defined in formulating the circuit-theoretic model (see, *e.g.*, [71, pp. 64–185]).

2.3.2 Transmission-line equations

Telegrapher's equations

Differential equations governing the propagation of voltage and current along the line may be derived directly from the Maxwell equations. Toward this end, note firstly that, with $E_\parallel = H_\parallel = 0$, (2.7) and (2.8) become

$$\frac{\partial \mathbf{E}_\perp}{\partial z} = -\mathrm{i}\omega\mu\, \hat{\mathbf{z}} \times \mathbf{H}_\perp, \tag{2.43}$$

$$\frac{\partial \mathbf{H}_\perp}{\partial z} = -(\sigma - \mathrm{i}\omega\epsilon)\, \hat{\mathbf{z}} \times \mathbf{E}_\perp. \tag{2.44}$$

Now, differentiating (2.41) and substituting from (2.43) leads to

$$\frac{\mathrm{d}v_j}{\mathrm{d}z} = -\int_{\mathcal{P}_j} \frac{\partial \mathbf{E}_\perp}{\partial z} \cdot \mathrm{d}\mathbf{l} = \mathrm{i}\omega\mu \int_{\mathcal{P}_j} \mathbf{H}_\perp \cdot (\mathrm{d}\mathbf{l} \times \hat{\mathbf{z}}) = \mathrm{i}\omega F_j(z), \tag{2.45}$$

where F_j is the (per-unit-length) magnetic flux linked by the contour $\mathcal{P}_j$. This, in turn, is related linearly to the conductor currents, and may be written in the form

$$F_j(z) = \sum_{j'} l_{jj'}\, i_{j'}(z). \tag{2.46}$$

Inserting (2.46) into (2.45), one obtains

$$\frac{\mathrm{d}\mathsf{v}}{\mathrm{d}z} = \mathrm{i}\omega\mathsf{L}\mathsf{i}, \tag{2.47}$$

where v and i denote the (2×1) vectors of conductor voltages and currents, respectively. Note from (2.46) that the elements $l_{jj'}$ of the inductance matrix L may be obtained by computing the flux linked by $\mathcal{P}_j$ under the condition

$$\lim_{\Delta z \to 0} \frac{1}{\Delta z} \int_z^{z+\Delta z} i_{j''}(z')\, \mathrm{d}z' = \delta_{j'j''} \text{ (A)}.$$

[‡]In this section, the indices j and j' will be understood to exclude conductor 0.

Next, differentiating (2.42) and substituting from (2.44) leads to

$$\frac{\mathrm{d}i_j}{\mathrm{d}z} = \oint_{\mathcal{C}_j} \frac{\partial \mathbf{H}_\perp}{\partial z} \cdot \mathrm{d}\mathbf{l} = -(\sigma - \mathrm{i}\omega\epsilon) \oint_{\mathcal{C}_j} \mathbf{E}_\perp \cdot (\mathrm{d}\mathbf{l} \times \hat{\mathbf{z}}) = -\left(\frac{\sigma}{\epsilon} - \mathrm{i}\omega\right) Q_j(z), \tag{2.48}$$

where Q_j is the (per-unit-length) electric charge enclosed by the contour $\mathcal{C}_j$. This, in turn, is related linearly to the conductor voltages, and may be written in the form

$$Q_j(z) = \sum_{j'} c_{jj'}\, v_{j'}(z). \tag{2.49}$$

Inserting (2.49) into (2.48), one obtains

$$\frac{\mathrm{d}\mathbf{i}}{\mathrm{d}z} = -(\mathsf{G} - \mathrm{i}\omega\mathsf{C})\,\mathbf{v}, \tag{2.50}$$

where the conductance matrix is given simply by

$$\mathsf{G} = \frac{\sigma}{\epsilon}\,\mathsf{C}. \tag{2.51}$$

Note from (2.49) that the elements $c_{jj'}$ of the capacitance matrix C may be obtained by computing the charge enclosed by $\mathcal{C}_j$ under the condition

$$\lim_{\Delta z \to 0} \frac{1}{\Delta z} \int_z^{z+\Delta z} v_{j''}(z')\,\mathrm{d}z' = \delta_{j'j''} \ \text{(V)}. \tag{2.52}$$

For the symmetric cable cross-section depicted in Fig. 2.1, the definition of capacitance implies that one has $c_{11} = c_{22} \equiv c_{\mathsf{s}}$ and $c_{12} = c_{21} \equiv c_{\mathsf{m}}$, where c_{s} and c_{m} respectively denote the self and the mutual capacitances of the two conductors. Consequently, the capacitance matrix takes the form

$$\mathsf{C} = \begin{bmatrix} c_{\mathsf{s}} & c_{\mathsf{m}} \\ c_{\mathsf{m}} & c_{\mathsf{s}} \end{bmatrix}. \tag{2.53}$$

It may be deduced from physical considerations that one must have

$$\begin{aligned} c_{\mathsf{s}} &\geq 0, \\ c_{\mathsf{m}} &\leq 0, \\ c_{\mathsf{s}} + c_{\mathsf{m}} &\geq 0. \end{aligned}$$

Voltage wave equation

Differentiating (2.47) and substituting from (2.50) and (2.51), one obtains the voltage wave equation

$$\frac{\mathrm{d}^2\mathbf{v}}{\mathrm{d}z^2} = -\mathrm{i}\omega\left(\frac{\sigma}{\epsilon} - \mathrm{i}\omega\right)\mathsf{LC}\mathbf{v}.$$

The conductor voltages are related linearly via (2.41) to the electric field, which satisfies

$$\frac{\partial^2 \mathbf{E}}{\partial z^2} = -k^2\mathbf{E},$$

as seen from (2.43) and (2.44). Therefore, one must have that

$$\mathrm{i}\omega\left(\frac{\sigma}{\epsilon} - \mathrm{i}\omega\right)\mathsf{LC} = k^2\mathsf{I},$$

where I denotes the (2×2) identity matrix. Consequently, the inductance matrix may be obtained from the capacitance matrix simply via

$$\mathsf{L} = \mu\epsilon\mathsf{C}^{-1}. \tag{2.54}$$

Since real metals are of large but finite conductivity, the two transmission-line modes of SUP cable are in fact *quasi*-TEM. The presence of (small) axial field components renders the definitions (2.41) and (2.42) for v_j and i_j dependent on the choices for $\mathcal{P}_j$ and $\mathcal{C}_j$, which, strictly speaking, spoils the unique correspondence between the circuit- and the field-theoretic variables. Fortunately, rigor may be restored by assuming *only* that the volume current density $\mathbf{J}$ remains purely axial within the metals. This is not merely a convenient analytical device for alleviating the difficulties associated with the circuit-theoretic model, but is indeed necessary for maintaining consistency with the filament model, which can only support axial currents. Under this assumption, the magnetic field remains purely transverse, while the transverse electric field remains perpendicular to the waveguide walls; thus, the uniqueness of definition (2.41) is preserved for arbitrary $\mathcal{P}_j$. Meanwhile, the ambiguity in definition (2.42), caused by the appearance of a small axial electric field in the insulator, may be removed by agreeing to let the contour $\mathcal{C}_j$ collapse onto the conductor wall $\mathcal{W}_j$.

Now, with $H_\parallel = 0$, (2.50) remains intact, while the term $\boldsymbol{\nabla}_\perp E_\parallel$ in (2.7) leads on the right-hand side of (2.45) to the additional term $-[E_\parallel(P_j) - E_\parallel(P_0)]$, where P_j and P_0 denote the end points of the path $\mathcal{P}_j$ on the j^{th} conductor and on the shield, respectively. Since $E_\parallel$ is proportional to the axial current density inside the metals, these additional voltage drops will also be related linearly to the conductor currents. Accordingly, (2.47) is generalized, for the case of finite metallic conductivity, by the introduction of a series impedance matrix Z, resulting in

$$\frac{\mathrm{d}\mathbf{v}}{\mathrm{d}z} = -(\mathsf{Z} - \mathrm{i}\omega\mathsf{L})\,\mathbf{i}. \tag{2.55}$$

Differentiating (2.55), substituting from (2.50), and making use of (2.51) and (2.54), one now obtains the *modified* voltage wave equation

$$\frac{\mathrm{d}^2\mathbf{v}}{\mathrm{d}z^2} = \left(\frac{\sigma}{\epsilon} - \mathrm{i}\omega\right)(\mathsf{ZC} - \mathrm{i}\omega\mu\epsilon\mathsf{I})\,\mathbf{v}. \tag{2.56}$$

For the symmetric cable cross-section depicted in Fig. 2.1, the definition of impedance implies that one has $z_{11} = z_{22} \equiv z_\mathsf{s}$ and $z_{12} = z_{21} \equiv z_\mathsf{m}$, where z_s and z_m respectively denote the self and the mutual impedances of the two conductors. Consequently, the impedance matrix takes the form

$$\mathsf{Z} = \begin{bmatrix} z_\mathsf{s} & z_\mathsf{m} \\ z_\mathsf{m} & z_\mathsf{s} \end{bmatrix}. \tag{2.57}$$

Physical considerations lead one to expect that

$$\begin{aligned} \Re[z_\mathsf{x}] &> 0, \\ \Im[z_\mathsf{x}] &< 0, \\ |z_\mathsf{s}| &\geq |z_\mathsf{m}|. \end{aligned}$$

2.3.3 Calculation of C

Filament model

It has been established in §2.3.2 that, for an ideal cable with infinite metallic conductivity, knowledge of C is sufficient for obtaining the remaining line parameters via (2.51) and (2.54). Based on the prescription given in connection with (2.49), the self capacitance may be computed via

$$c_\mathsf{s} = -\epsilon \oint_{\mathcal{W}_1} \hat{\mathbf{n}}_1 \cdot \boldsymbol{\nabla}_\perp \Phi(\mathbf{r}_\perp)\,\mathrm{d}l, \tag{2.58}$$

where use was made of (2.32), and the appropriate potential satisfying (2.52) is

$$\Phi(\mathbf{r}_\perp) = \frac{1}{2}\left[\frac{\Phi_\mathsf{e}(\mathbf{r}_\perp)}{\Phi_\mathsf{e}(\mathcal{W}_1)} + \frac{\Phi_\mathsf{o}(\mathbf{r}_\perp)}{\Phi_\mathsf{o}(\mathcal{W}_1)}\right]. \tag{2.59}$$

There is a minor difficulty in using (2.37) to construct (2.59), since $\mathcal{W}_1$ is *not* an equipotential surface under the filament model, and hence $\Phi_\mathsf{x}(\mathcal{W}_1)$ are not constant. This ambiguity may be removed by agreeing to use

the *average* value of the potential on $\mathcal{W}_1$. With this convention, substitution into (2.58), along with $\hat{\mathbf{n}}_1 = \hat{\boldsymbol{\varrho}}$ and $\oint_{\mathcal{W}_1} \mathrm{d}l = \int_0^{2\pi} r_\mathsf{w}\,\mathrm{d}\varphi$, leads readily to

$$c_\mathsf{s} = \pi\epsilon \left[\frac{1}{\ln(R_\mathsf{e}/r_\mathsf{w})} + \frac{1}{\ln(R_\mathsf{o}/r_\mathsf{w})} \right]. \tag{2.60}$$

For the mutual capacitance, one may again integrate on $\mathcal{W}_1$ as in (2.58), but this time taking the difference, rather than the sum, of the ratios in (2.59) in order to satisfy (2.52). The result is

$$c_\mathsf{m} = \pi\epsilon \left[\frac{1}{\ln(R_\mathsf{e}/r_\mathsf{w})} - \frac{1}{\ln(R_\mathsf{o}/r_\mathsf{w})} \right]. \tag{2.61}$$

For the parameter values in Table 2.1, (2.60) and (2.61) give $c_\mathsf{s} = 111.477\,\mathrm{pF/m}$ and $c_\mathsf{m} = -17.3822\,\mathrm{pF/m}$. These theoretical values compare favorably with the results of numerical integration on the numerical potential computation described in §2.2.2, which yields $c_\mathsf{s} = 111.475\ \mathrm{pF/m}$ and $c_\mathsf{m} = -17.3847\ \mathrm{pF/m}$.

Comparison with other models

It is worthwhile comparing the accuracy of the analytical capacitance expressions obtained here with those found in the literature in order to cement one's confidence in the present model. One typically finds the conductor-to-conductor capacitance specified for balanced (*i.e.*, odd-mode) excitation, and sometimes also the conductor-to-shield capacitance for longitudinal (*i.e.*, even-mode) excitation. For the filament model, these capacitances may be obtained by substituting from (2.60) and (2.61) into the definitions

$$\begin{aligned} c_\mathsf{o} &\equiv \tfrac{1}{2}\,(c_\mathsf{s} - c_\mathsf{m}), \\ c_\mathsf{e} &\equiv c_\mathsf{s} + c_\mathsf{m}. \end{aligned}$$

Other well-known formulas are listed in Table 2.2, along with their numerical evaluations for the parameter values in Table 2.1. Since the calculation of capacitance is a one-time operation, the simplicity of formulas is not a key consideration, and accuracy is the chief criterion by which different models are to be judged. That all the formulas are of similar form and complexity reveals an essential commonality among the different analytical approaches, as mentioned in §1.2. It should be noted that the observations made below regarding the relative accuracies of the various models apply only to the cable geometry considered here, and should *not* be expected to hold generally.

The results of numerical computation are given to serve as a benchmark, and the filament model is included to facilitate comparison. The textbook formulas for the two-wire and the coaxial lines are provided for comparison with the analogous cases of balanced and longitudinal SUP cable excitation, respectively. (The additional factor of two in the formula for the coaxial line accounts for the fact that c_e defined here is the capacitance between a *single* conductor and the shield.) Not surprisingly, both give poor results.

The Bell Labs formula, due to S. Mead, is widely quoted (see, *e.g.*, [25], [67, p. 117] or [55, p. 250]) and was evidently obtained by solving, via successive approximations, J. Carson's original formulation for the proximity effect [19, 22]. Comparison with the King formula for c_o, however, shows that the additional term in the Bell Labs formula is not appreciable. The Philips Labs formulas are given without a derivation or a source reference; their crudeness was noted by C. Miller.[§]

The other formula based on a filament model in Table 2.2 is the one due to A. Gent. In order to establish equipotential surfaces on the two conductors, he placed the first pair of filaments at the bipolar foci, which are on the *opposite* sides of the conductor centers from the optimal filament positions shown in Fig. 2.7. As a result, he found it necessary to add *five* more pairs—one pair outside the shield, with the remaining pairs along the x axis within the conductors—yet the accuracy he achieved is still relatively poor.

King, on the other hand, placed his filaments at the centers of the conductors, and adjusted the positions of the image filaments outside the shield to achieve zero potential on the shield. (More precisely, he started from an exact formulation *à la* Craggs, but then made assumptions on the cable geometry that effectively reduces his approach to a filament model.) Consequently, his formulas agree exactly with the present model *if* one takes $r_\mathsf{c} = q$ in evaluating R_x in (2.38) and (2.39). As one would expect in view of Fig. 2.7, the

[§]The transcription of the Philips formula for c_e in [15] contains an inconsequential error, which is corrected here.

Table 2.2: Comparison of SUP cable capacitance values obtained with different models.

Source	$\pi\epsilon/c_{\mathsf{o}}$		$2\pi\epsilon/c_{\mathsf{e}}$	
	Formula	*Value*	*Formula*	*Value*
numerical computation		0.992975		1.35991
filament model	$\ln\left(\frac{r_{\mathsf{co}}+q}{r_{\mathsf{w}}}\,\frac{r_{\mathsf{i}}^2-qr_{\mathsf{co}}}{r_{\mathsf{i}}^2+qr_{\mathsf{co}}}\right)$	0.992978	$\ln\left[\frac{r_{\mathsf{i}}^4-(qr_{\mathsf{ce}})^2}{(r_{\mathsf{ce}}+q)r_{\mathsf{w}}r_{\mathsf{i}}^2}\right]$	1.35984
two-wire line	$\cosh^{-1}(q/r_{\mathsf{w}})$	1.45057		
coaxial line			$2\ln(r_{\mathsf{i}}/r_{\mathsf{ce}})$	1.1473
BELL LABS [23]	$\ln\left(\frac{2q}{r_{\mathsf{w}}}\,\frac{r_{\mathsf{i}}^2-q^2}{r_{\mathsf{i}}^2+q^2}\right)$ $-\,\frac{r_{\mathsf{w}}^2(r_{\mathsf{w}}^2+4q^2)(r_{\mathsf{i}}^2-4q^2)}{(4q^2r_{\mathsf{i}})^2}$	0.993252		
PHILIPS LABS [72]	$\cosh^{-1}\left[\frac{q}{r_{\mathsf{w}}}\,\frac{r_{\mathsf{i}}^2-(q^2-r_{\mathsf{w}}^2)}{r_{\mathsf{i}}^2+(q^2-r_{\mathsf{w}}^2)}\right]$	0.960697	$\cosh^{-1}\left[\frac{r_{\mathsf{i}}^4-(q^2-r_{\mathsf{w}}^2)^2}{4qr_{\mathsf{w}}r_{\mathsf{i}}^2}\right]$	1.40448
GENT [7]	$\ln\left(\frac{q+\sqrt{q^2-r_{\mathsf{w}}^2}}{r_{\mathsf{w}}}\,\frac{r_{\mathsf{i}}^2-q\sqrt{q^2-r_{\mathsf{w}}^2}}{r_{\mathsf{i}}^2+q\sqrt{q^2-r_{\mathsf{w}}^2}}\right)$	0.994949		
KING [73, pp. 34–39]	$\ln\left(\frac{2q}{r_{\mathsf{w}}}\,\frac{r_{\mathsf{i}}^2-q^2}{r_{\mathsf{i}}^2+q^2}\right)$	0.993252	$\ln\left(\frac{r_{\mathsf{i}}^4-q^4}{2qr_{\mathsf{w}}r_{\mathsf{i}}^2}\right)$	1.43954
MILLER [15]	$\ln\left(\frac{2q}{r_{\mathsf{w}}}\,\frac{r_{\mathsf{i}}^2-q^2}{r_{\mathsf{i}}^2+q^2}\right)$ $-\,\frac{\frac{1}{4}\left(\frac{r_{\mathsf{w}}}{q}\right)^2\left[1-\frac{4(qr_{\mathsf{i}})^2}{r_{\mathsf{i}}^4-q^4}\right]^2}{1-\left(\frac{r_{\mathsf{w}}}{q}\right)^2\left[\frac{1}{4}+\frac{2(qr_{\mathsf{i}})^2(r_{\mathsf{i}}^4+q^4)}{(r_{\mathsf{i}}^4-q^4)^2}\right]}$	0.992988	$\ln\left(\frac{r_{\mathsf{i}}^2}{2qr_{\mathsf{w}}}\sqrt{\frac{r_{\mathsf{i}}^4-q^4}{r_{\mathsf{i}}^4+q^4}}\,\frac{r_{\mathsf{i}}^8-q^8}{r_{\mathsf{i}}^8+q^8}\right)$ $-\,\frac{\frac{1}{4}\left(\frac{r_{\mathsf{w}}}{q}\right)^2\left(1+\frac{4q^4}{r_{\mathsf{i}}^4-q^4}\right)^2}{1+\left(\frac{r_{\mathsf{w}}}{q}\right)^2\left[\frac{1}{4}-\frac{4(qr_{\mathsf{i}})^4}{(r_{\mathsf{i}}^4-q^4)^2}\right]}$	1.35391

numerical agreement between the King formula and the present model for c_{o} is good, while that for c_{e} is less than satisfactory.

The Miller formulas are based on the rigorous approach of J. Craggs described in §1.2;¶ the expressions given here were obtained by a 2×2 truncation of the infinite determinants in [15]. Comparison with the exact value for c_{o} shows that the additional term in the Miller formula does provide an improvement over the King formula. Despite the proper treatment of the conductor boundaries, however, it is observed that this approach is *not* superior in accuracy to the filament model developed here. Going up to a 3×3 truncation might improve the accuracy, but would certainly lead to considerably more unwieldy formulas, and is therefore omitted.

2.3.4 Calculation of Z

Skin effect

In order to isolate the contribution of the skin effect, the coaxial arrangement of a *single* wire inside a shield will be treated first (see, *e.g.*, [75] or [76, pp. 545–554]), and the familiar boundary conditions $\hat{\mathbf{n}} \times \mathbf{E} = \mathbf{0}$, $\hat{\mathbf{n}} \times \mathbf{H} = \mathbf{K}$ at the surface of a perfect conductor will be supplanted by the "impedance" boundary condition

$$E_{\parallel} = \zeta K_{\parallel}, \tag{2.62}$$

leading to the identification of a suitable surface impedance ζ for each conductor.

Consider, then, a round metallic wire of radius r_{w} and (large) conductivity σ_{w}, carrying a current through an homogeneous medium with constitutive parameters ϵ, μ, and σ. The return conductor is a cylindrical tube with inner radius $r_{\mathsf{i}} > r_{\mathsf{w}}$, outer radius r_{s}, and (large) conductivity σ_{s}. The wire and the shield

¶The transcription of the Craggs formula for c_{o} in [7], with which Gent compared his result, contained an error; the Miller formula derived here supplies the correction. Although B. King and coworkers later picked up the same error in [74], their criticism of Gent's conclusions remains valid.

are situated coaxially, and therefore the currents on both conductors are azimuthally uniform. With the conductor currents assumed to be purely axial, as has been discussed in §2.3.1, the Maxwell equations may be solved by the introduction of an (E-type) Hertz potential $\boldsymbol{\Pi} = \hat{\mathbf{z}}\,\Psi(\rho)\,\mathrm{e}^{\mathrm{i}\lambda z}$ (see, *e.g.*, [76, pp. 28–32]). Thus, inside the wire, one has

$$E_{\parallel}(\rho) \;=\; (\xi_{\mathsf{w}}^2 - \lambda^2)\,\Psi(\rho)\,\mathrm{e}^{\mathrm{i}\lambda z}, \tag{2.63}$$

$$H_{\phi}(\rho) \;=\; -(\sigma_{\mathsf{w}} - \mathrm{i}\omega\epsilon_0)\,\frac{\mathrm{d}\Psi}{\mathrm{d}\rho}\,\mathrm{e}^{\mathrm{i}\lambda z}, \tag{2.64}$$

where $\xi_{\mathsf{w}} = \sqrt{\mathrm{i}\omega\mu_0(\sigma_{\mathsf{w}} - \mathrm{i}\omega\epsilon_0)} \simeq \sqrt{\mathrm{i}\omega\mu_0\sigma_{\mathsf{w}}}$ is the wave number in the wire, and Ψ satisfies

$$\frac{1}{\rho}\,\frac{\mathrm{d}}{\mathrm{d}\rho}\left(\rho\,\frac{\mathrm{d}\Psi}{\mathrm{d}\rho}\right) + (\xi_{\mathsf{w}}^2 - \lambda^2)\,\Psi = 0. \tag{2.65}$$

Since $\lambda \simeq k \ll \xi_{\mathsf{w}}$, the solution of (2.65) is approximately

$$\Psi(\rho) = AJ_0(\xi_{\mathsf{w}}\rho), \tag{2.66}$$

where A is an unknown constant, and $J_m(\cdot)$ denotes the ordinary Bessel function of the first kind.

At $\rho = r_{\mathsf{w}}$, one has that $K_{\parallel} = H_{\phi}$, where $\mathbf{K}$ signifies an *effective* surface current density [12, pp. 352–356]. It then follows from (2.62) that the ratio $E_{\parallel}/H_{\phi}$ gives the AC surface impedance ζ_{w} of the wire. Substituting from (2.66) into (2.63) and (2.64), one thus obtains

$$\zeta_{\mathsf{w}} = \frac{\xi_{\mathsf{w}}}{\sigma_{\mathsf{w}}}\,\frac{J_0(\xi_{\mathsf{w}} r_{\mathsf{w}})}{J_1(\xi_{\mathsf{w}} r_{\mathsf{w}})}. \tag{2.67}$$

Using small-argument approximations for $J_m(\cdot)$ [68, p. 360], one readily finds that

$$\lim_{\omega\to 0}\frac{\zeta_{\mathsf{w}}}{2\pi r_{\mathsf{w}}} = \frac{1}{\pi r_{\mathsf{w}}^2\sigma_{\mathsf{w}}},$$

which is the correct (per-unit-length) DC resistance of the wire. Meanwhile, large-argument approximations for $J_m(\cdot)$ [68, p. 364] lead to the high-frequency asymptote

$$\lim_{\omega\to\infty}\frac{\zeta_{\mathsf{w}}}{2\pi r_{\mathsf{w}}} = \frac{1-\mathrm{i}}{2\pi r_{\mathsf{w}}}\sqrt{\frac{\omega\mu_0}{2\sigma_{\mathsf{w}}}}.$$

Inside the shield, one instead has the solution

$$\Psi(\rho) = BJ_0(\xi_{\mathsf{s}}\rho) + CN_0(\xi_{\mathsf{s}}\rho),$$

where $\xi_{\mathsf{s}} \simeq \sqrt{\mathrm{i}\omega\mu_0\sigma_{\mathsf{s}}}$, B and C are unknown constants, and $N_m(\cdot)$ denotes the ordinary Bessel function of the second kind. The corresponding fields are obtained as in (2.63) and (2.64), giving

$$\begin{aligned} E_{\parallel}(\rho) \;&\simeq\; \xi_{\mathsf{s}}^2[BJ_0(\xi_{\mathsf{s}}\rho) + CN_0(\xi_{\mathsf{s}}\rho)]\,\mathrm{e}^{\mathrm{i}\lambda z}, \\ H_{\phi}(\rho) \;&\simeq\; \sigma_{\mathsf{s}}\xi_{\mathsf{s}}[BJ_1(\xi_{\mathsf{s}}\rho) + CN_1(\xi_{\mathsf{s}}\rho)]\,\mathrm{e}^{\mathrm{i}\lambda z}. \end{aligned}$$

At $\rho = r_{\mathsf{i}}$, one now has that $K_{\parallel} = -H_{\phi}$, since the outward surface normal reverses its direction. In forming the ratio $-E_{\parallel}/H_{\phi}$ to obtain the AC surface impedance ζ_{s} of the shield, it is necessary to explicitly evaluate the quantity C/B. Rigorously, one must write down solutions for $E_{\parallel}$ and H_{ϕ} suitable for the dielectric media in the interior and the exterior of the shield, and match them with the above solutions across the three boundaries at $\rho = r_{\mathsf{w}}$, $\rho = r_{\mathsf{i}}$, and $\rho = r_{\mathsf{s}}$ to find all the unknown constants along with the appropriate axial eigenvalue λ. For sufficiently large σ_{s}, the result is simply $C/B \simeq -J_1(\xi_{\mathsf{s}} r_{\mathsf{s}})/N_1(\xi_{\mathsf{s}} r_{\mathsf{s}})$, and consequently

$$\zeta_{\mathsf{s}} = -\frac{\xi_{\mathsf{s}}}{\sigma_{\mathsf{s}}}\,\frac{J_0(\xi_{\mathsf{s}} r_{\mathsf{i}})\,N_1(\xi_{\mathsf{s}} r_{\mathsf{s}}) - N_0(\xi_{\mathsf{s}} r_{\mathsf{i}})\,J_1(\xi_{\mathsf{s}} r_{\mathsf{s}})}{J_1(\xi_{\mathsf{s}} r_{\mathsf{i}})\,N_1(\xi_{\mathsf{s}} r_{\mathsf{s}}) - N_1(\xi_{\mathsf{s}} r_{\mathsf{i}})\,J_1(\xi_{\mathsf{s}} r_{\mathsf{s}})}. \tag{2.68}$$

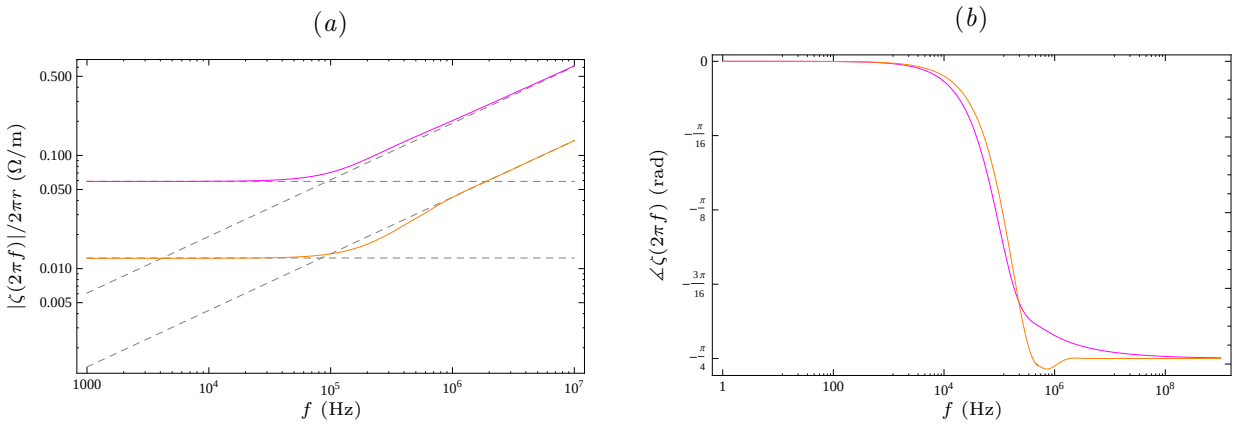

Figure 2.10: Magnitudes (a) and phases (b) of the surface impedances of a round wire (magenta) and a cylindrical tube (orange) in a coaxial arrangement; the dashed lines indicate the corresponding low- and high-frequency asymptotes.

Using small-argument approximations, it may be shown that

$$\lim_{\omega\to 0}\frac{\zeta_{\mathsf{s}}}{2\pi r_{\mathsf{i}}}=\frac{1}{\pi(r_{\mathsf{s}}^2-r_{\mathsf{i}}^2)\sigma_{\mathsf{s}}},$$

which is the correct (per-unit-length) DC resistance of the shield. At sufficiently high frequencies, where the skin effect is fully developed, large-argument approximations provide the asymptotic value $C/B\to\mathrm{i}$, which leads to

$$\lim_{\omega\to\infty}\frac{\zeta_{\mathsf{s}}}{2\pi r_{\mathsf{i}}}=-\frac{\xi_{\mathsf{s}}}{\sigma_{\mathsf{s}}}\frac{H_0^{(1)}(\xi_{\mathsf{s}}r_{\mathsf{i}})}{H_1^{(1)}(\xi_{\mathsf{s}}r_{\mathsf{i}})}\to\frac{1-\mathrm{i}}{2\pi r_{\mathsf{i}}}\sqrt{\frac{\omega\mu_0}{2\sigma_{\mathsf{s}}}},$$

where $H_m^{(1)}(\cdot)=J_m(\cdot)+\mathrm{i}N_m(\cdot)$ denotes the Hankel function of the first kind.

The per-unit-length surface impedances of the wire and the shield are plotted in Fig. 2.10 using the parameter values in Table 2.1. It is observed that these impedances are indeed inductive, as has been anticipated in §2.3.2.

Proximity effect

When *two* round wires and a tubular shield are assembled into cable form as in Fig. 2.1, the proximity effect enters into the picture, modifying the azimuthal distributions of currents on the conductors from the uniform case of the coaxial arrangement considered above. This situation is analyzed next by perturbing the boundary conditions (see, *e.g.*, [66, pp. 1038–1064] or [12, pp. 366–368]) on the field solutions obtained in §2.2.2, thus supplying the connection between the surface impedances ζ_{w} and ζ_{s} derived above and the heretofore unknown phenomenological line parameters z_{s} and z_{m} introduced in §2.3.2.

With the Hertz potential now taken as $\boldsymbol{\Pi}=\hat{\mathbf{z}}\,\Psi(\mathbf{r}_\perp)\,\mathrm{e}^{\mathrm{i}\lambda z}$, the fields in the insulator are

$$\mathbf{E}_\perp(\mathbf{r}) = \mathrm{i}\lambda\,\boldsymbol{\nabla}_\perp\Psi(\mathbf{r}_\perp)\,\mathrm{e}^{\mathrm{i}\lambda z}, \tag{2.69}$$

$$E_\parallel(\mathbf{r}) = (k^2-\lambda^2)\,\Psi(\mathbf{r}_\perp)\,\mathrm{e}^{\mathrm{i}\lambda z}, \tag{2.70}$$

$$\mathbf{H}_\perp(\mathbf{r}) = -(\sigma-\mathrm{i}\omega\epsilon)\,\hat{\mathbf{z}}\times\boldsymbol{\nabla}_\perp\Psi(\mathbf{r}_\perp)\,\mathrm{e}^{\mathrm{i}\lambda z}, \tag{2.71}$$

where

$$\nabla_\perp^2\Psi+(k^2-\lambda^2)\,\Psi=0. \tag{2.72}$$

In the "unperturbed" case of perfectly conducting metals, to be indicated by the superscript (∞), the field expressions (2.69) and (2.71) must, of course, reduce to (2.29) and (2.30). Since $\lambda^{(\infty)}=k$, this requirement translates into

$$\Psi^{(\infty)}(\mathbf{r}_\perp)=\frac{\mathrm{i}}{k}\,\Phi(\mathbf{r}_\perp). \tag{2.73}$$

The application of Green's theorem to the two potentials Ψ and $\Psi^{(\infty)}$ gives

$$\iint_{\mathcal{A}} \left[\Psi\, \nabla_\perp^2 \Psi^{(\infty)} - \Psi^{(\infty)}\, \nabla_\perp^2 \Psi\right] \mathrm{d}a = \oint_{\mathcal{C}} \left[\Psi\, \frac{\partial \Psi^{(\infty)}}{\partial n} - \Psi^{(\infty)}\, \frac{\partial \Psi}{\partial n}\right] \mathrm{d}l.$$

(Since the surface normals have been drawn *inward* the insulator cross-section $\mathcal{A}$ in Fig. 2.1, the bounding contour $\mathcal{C} = \mathcal{W}_0 \cup \mathcal{W}_1 \cup \mathcal{W}_2$ must be traversed in the *negative* sense around $\mathcal{A}$.) Substituting from (2.72) and (2.73) and recalling (2.40), this becomes

$$(k^2 - \lambda^2) \iint_{\mathcal{A}} \Phi\, \Psi \,\mathrm{d}a = \oint_{\mathcal{C}} \left[\frac{\Psi}{\partial \Psi / \partial n}\, \frac{\partial \Phi}{\partial n} - \Phi\right] \frac{\partial \Psi}{\partial n}\, \mathrm{d}l.$$

At the metal–insulator boundaries, the axial electric field and the azimuthal magnetic field are continuous; therefore, one may use the field solutions inside the wire and the shield obtained above to show that

$$\frac{\Psi}{\partial \Psi / \partial n} = \zeta\, \frac{\sigma - \mathrm{i}\omega\epsilon}{\lambda^2 - k^2} \quad \text{for} \quad \mathbf{r}_\perp \in \mathcal{C}.$$

Rearranging, one finally obtains

$$(\lambda^2 - k^2)^2 \iint_{\mathcal{A}} \Phi\, \Psi \,\mathrm{d}a - (\lambda^2 - k^2) \oint_{\mathcal{C}} \Phi\, \frac{\partial \Psi}{\partial n}\, \mathrm{d}l + (\sigma - \mathrm{i}\omega\epsilon) \oint_{\mathcal{C}} \zeta\, \frac{\partial \Phi}{\partial n}\, \frac{\partial \Psi}{\partial n}\, \mathrm{d}l = 0. \tag{2.74}$$

Two approximations are now made to facilitate the solution of (2.74). In the first place, the unknown potential Ψ is replaced, to lowest order of approximation, by its unperturbed version $\Psi^{(\infty)}$, a choice that may be placed on a firm footing via the variational principle [6, pp. 255–259]. Note secondly that the change in λ from its unperturbed value k is expected to be inversely proportional to (some power of) the metal conductivities, which are very large; therefore, $(\lambda^2 - k^2)^2 \ll (\lambda^2 - k^2)$. At the same time, the ratio of the area integral in the first term to the contour integral in the second term of (2.74) is estimated to be of the order of the cross-sectional area of the guide, which, for typical transverse cable dimensions, is extremely small.[‖] Consequently, canceling out the prefactor in (2.31) that is common to all the terms, and neglecting the first term entirely, (2.74) simplifies to

$$(\lambda^2 - k^2) \underbrace{\oint_{\mathcal{C}} F\, \frac{\partial F}{\partial n}\, \mathrm{d}l}_{\mathcal{I}_1} = (\sigma - \mathrm{i}\omega\epsilon) \underbrace{\oint_{\mathcal{C}} \zeta \left(\frac{\partial F}{\partial n}\right)^2 \mathrm{d}l}_{\mathcal{I}_0}. \tag{2.75}$$

Filament model

The two contour integrals appearing in (2.75) will now be evaluated using the potential obtained in §2.2.2. In keeping with the convention established in evaluating (2.58), it is again assumed that, with the optimal choice of r_{c}, the azimuthal variation of Φ on $\mathcal{W}_j$ is negligibly small; it is important, however, to introduce this approximation *after* the normal derivative of Φ, where it is involved, has been taken. Noting that Φ is exactly zero on the shield and exploiting the symmetry of the cable structure, one readily obtains

$$\begin{aligned} \mathcal{I}_1 &= 2 \int_0^{2\pi} \left[F(\varrho, \varphi)\, \frac{\partial F(\varrho, \varphi)}{\partial \varrho}\right]_{\varrho = r_{\mathsf{w}}} r_{\mathsf{w}}\, \mathrm{d}\varphi \\ &= -16\pi \ln\left(\frac{R}{r_{\mathsf{w}}}\right), \end{aligned} \tag{2.76}$$

where substitutions were made from (2.37), and use was made of $\int_0^{2\pi} \cos(m\varphi)\, \cos(m'\varphi)\, \mathrm{d}\varphi = \pi \delta_{mm'}$. With substitutions from (2.37) and (2.31), and the additional use of $\sum_{m=1}^{\infty} x^m = x/(1-x)$, valid for $|x| < 1$, one similarly obtains

$$\begin{aligned} \mathcal{I}_0 &= 2\zeta_{\mathsf{w}} \int_0^{2\pi} \left[\frac{\partial F(\varrho, \varphi)}{\partial \varrho}\right]_{\varrho = r_{\mathsf{w}}}^2 r_{\mathsf{w}}\, \mathrm{d}\varphi + \zeta_{\mathsf{s}} \int_0^{2\pi} \left[-\frac{\partial F(\rho, -\phi)}{\partial \rho}\right]_{\rho = r_{\mathsf{i}}}^2 r_{\mathsf{i}}\, \mathrm{d}\phi \\ &= 2\zeta_{\mathsf{w}}\, \frac{8\pi}{r_{\mathsf{w}}}\, \frac{r_{\mathsf{w}}^2 + (r_{\mathsf{c}} - q)^2}{r_{\mathsf{w}}^2 - (r_{\mathsf{c}} - q)^2} + \zeta_{\mathsf{s}}\, \frac{8\pi}{r_{\mathsf{i}}} \left[(1 \pm 1)^2 + 4 r_{\mathsf{c}}^2\, \frac{(r_{\mathsf{i}}^2 + r_{\mathsf{c}}^2) \mp (r_{\mathsf{i}}^2 - r_{\mathsf{c}}^2)}{r_{\mathsf{i}}^4 - r_{\mathsf{c}}^4}\right], \end{aligned} \tag{2.77}$$

[‖] Exact integration with $\Psi = \Psi^{(\infty)}$ shows that this ratio is less than 10^{-6} in magnitude for both modes.

where, as before, the upper (lower) sign goes with the even (odd) mode.

Finally, the variational expression (2.75) is compared with the circuit-theoretic expression (2.82) for λ, leading to the identification $\chi^2 = -\epsilon(\mathcal{I}_0/\mathcal{I}_1)$. Using (2.80) for χ_{e} and χ_{o}, along with the expressions (2.60) and (2.61) for c_{s} and c_{m}, this yields the following equations for the unknown impedances z_{s} and z_{m}:

$$\begin{aligned} z_{\mathsf{s}} + z_{\mathsf{m}} &= -\frac{\ln(R_{\mathsf{e}}/r_{\mathsf{w}})}{2\pi} \left.\frac{\mathcal{I}_0}{\mathcal{I}_1}\right|_{\mathsf{e}}, \\ z_{\mathsf{s}} - z_{\mathsf{m}} &= -\frac{\ln(R_{\mathsf{o}}/r_{\mathsf{w}})}{2\pi} \left.\frac{\mathcal{I}_0}{\mathcal{I}_1}\right|_{\mathsf{o}}. \end{aligned}$$

These are solved readily with the aid of the integrals (2.76) and (2.77), obtaining

$$z_{\mathsf{s}} = \frac{\zeta_{\mathsf{w}}}{2\pi r_{\mathsf{w}}}\left[1 + \frac{(r_{\mathsf{ce}}-q)^2}{r_{\mathsf{w}}^2-(r_{\mathsf{ce}}-q)^2} + \frac{(r_{\mathsf{co}}-q)^2}{r_{\mathsf{w}}^2-(r_{\mathsf{co}}-q)^2}\right] + \frac{\zeta_{\mathsf{s}}}{2\pi r_{\mathsf{i}}}\left(\frac{r_{\mathsf{i}}^4+r_{\mathsf{ce}}^4}{r_{\mathsf{i}}^4-r_{\mathsf{ce}}^4} + \frac{2r_{\mathsf{i}}^2 r_{\mathsf{co}}^2}{r_{\mathsf{i}}^4-r_{\mathsf{co}}^4}\right), \tag{2.78}$$

$$z_{\mathsf{m}} = \frac{\zeta_{\mathsf{w}}}{2\pi r_{\mathsf{w}}}\left[\frac{(r_{\mathsf{ce}}-q)^2}{r_{\mathsf{w}}^2-(r_{\mathsf{ce}}-q)^2} - \frac{(r_{\mathsf{co}}-q)^2}{r_{\mathsf{w}}^2-(r_{\mathsf{co}}-q)^2}\right] + \frac{\zeta_{\mathsf{s}}}{2\pi r_{\mathsf{i}}}\left(\frac{r_{\mathsf{i}}^4+r_{\mathsf{ce}}^4}{r_{\mathsf{i}}^4-r_{\mathsf{ce}}^4} - \frac{2r_{\mathsf{i}}^2 r_{\mathsf{co}}^2}{r_{\mathsf{i}}^4-r_{\mathsf{co}}^4}\right). \tag{2.79}$$

2.3.5 General solution

Voltage and current

Returning now to the voltage wave equation, the solution of (2.56) requires knowledge of the eigensystem of the matrix $\mathbf{ZC}$, which is sought in the form

$$\mathbf{ZC}\mathbf{x} = \chi^2\mathbf{x}.$$

For the symmetric and reciprocal cable model under consideration, one has, from (2.53) and (2.57), that

$$\mathbf{ZC} = \begin{bmatrix} z_{\mathsf{s}}c_{\mathsf{s}} + z_{\mathsf{m}}c_{\mathsf{m}} & z_{\mathsf{s}}c_{\mathsf{m}} + z_{\mathsf{m}}c_{\mathsf{s}} \\ z_{\mathsf{s}}c_{\mathsf{m}} + z_{\mathsf{m}}c_{\mathsf{s}} & z_{\mathsf{s}}c_{\mathsf{s}} + z_{\mathsf{m}}c_{\mathsf{m}} \end{bmatrix}.$$

The corresponding eigenvalues and (normalized) eigenvectors are then

$$\begin{aligned} &\chi_{\mathsf{e}} = \sqrt{(z_{\mathsf{s}}+z_{\mathsf{m}})(c_{\mathsf{s}}+c_{\mathsf{m}})}, && \chi_{\mathsf{o}} = \sqrt{(z_{\mathsf{s}}-z_{\mathsf{m}})(c_{\mathsf{s}}-c_{\mathsf{m}})}, \\ &\mathbf{x}_{\mathsf{e}} = \tfrac{1}{\sqrt{2}}\,[1 \quad 1]^{\mathrm{T}}, && \mathbf{x}_{\mathsf{o}} = \tfrac{1}{\sqrt{2}}\,[1 \quad -1]^{\mathrm{T}}. \end{aligned} \tag{2.80}$$

As expected, the eigenmodes of this circuit-theoretic cable model are found to be the same even and odd transmission-line modes of the field-theoretic model developed in §2.2.

The solution of (2.56) may now be written down in the form

$$\mathbf{v}(z) = \left(V_{\mathsf{e}}^+ \,\mathrm{e}^{\mathrm{i}\lambda_{\mathsf{e}}z} + V_{\mathsf{e}}^- \,\mathrm{e}^{-\mathrm{i}\lambda_{\mathsf{e}}z}\right)\mathbf{x}_{\mathsf{e}} + \left(V_{\mathsf{o}}^+ \,\mathrm{e}^{\mathrm{i}\lambda_{\mathsf{o}}z} + V_{\mathsf{o}}^- \,\mathrm{e}^{-\mathrm{i}\lambda_{\mathsf{o}}z}\right)\mathbf{x}_{\mathsf{o}}, \tag{2.81}$$

where, with $\mathsf{x} = \mathsf{e}, \mathsf{o}$, the axial eigenvalues are

$$\lambda_{\mathsf{x}}(\omega) = \sqrt{k^2 - \left(\frac{\sigma}{\epsilon} - \mathrm{i}\omega\right)\chi_{\mathsf{x}}^2}. \tag{2.82}$$

From (2.55), the corresponding mode currents are then given by

$$\begin{aligned} \mathbf{i}(z) &= -(\mathbf{Z} - \mathrm{i}\omega\mathbf{L})^{-1}\,\frac{\mathrm{d}\mathbf{v}}{\mathrm{d}z} \\ &= \frac{1}{Z_{\mathsf{e}}}\left(V_{\mathsf{e}}^+ \,\mathrm{e}^{\mathrm{i}\lambda_{\mathsf{e}}z} - V_{\mathsf{e}}^- \,\mathrm{e}^{-\mathrm{i}\lambda_{\mathsf{e}}z}\right)\mathbf{x}_{\mathsf{e}} + \frac{1}{Z_{\mathsf{o}}}\left(V_{\mathsf{o}}^+ \,\mathrm{e}^{\mathrm{i}\lambda_{\mathsf{o}}z} - V_{\mathsf{o}}^- \,\mathrm{e}^{-\mathrm{i}\lambda_{\mathsf{o}}z}\right)\mathbf{x}_{\mathsf{o}}, \end{aligned} \tag{2.83}$$

where the characteristic impedances for the two modes are defined as

$$Z_{\mathsf{e}}(\omega) = \frac{(z_{\mathsf{m}}^2 - z_{\mathsf{s}}^2)(c_{\mathsf{s}}^2 - c_{\mathsf{m}}^2) + \mathrm{i}2\omega\mu\epsilon(z_{\mathsf{s}}c_{\mathsf{s}} + z_{\mathsf{m}}c_{\mathsf{m}}) + (\omega\mu\epsilon)^2}{\mathrm{i}\lambda_{\mathsf{e}}(c_{\mathsf{s}}+c_{\mathsf{m}})[(z_{\mathsf{s}}-z_{\mathsf{m}})(c_{\mathsf{s}}-c_{\mathsf{m}}) - \mathrm{i}\omega\mu\epsilon]}, \tag{2.84}$$

$$Z_{\mathsf{o}}(\omega) = \frac{(z_{\mathsf{m}}^2 - z_{\mathsf{s}}^2)(c_{\mathsf{s}}^2 - c_{\mathsf{m}}^2) + \mathrm{i}2\omega\mu\epsilon(z_{\mathsf{s}}c_{\mathsf{s}} + z_{\mathsf{m}}c_{\mathsf{m}}) + (\omega\mu\epsilon)^2}{\mathrm{i}\lambda_{\mathsf{o}}(c_{\mathsf{s}}-c_{\mathsf{m}})[(z_{\mathsf{s}}+z_{\mathsf{m}})(c_{\mathsf{s}}+c_{\mathsf{m}}) - \mathrm{i}\omega\mu\epsilon]}. \tag{2.85}$$

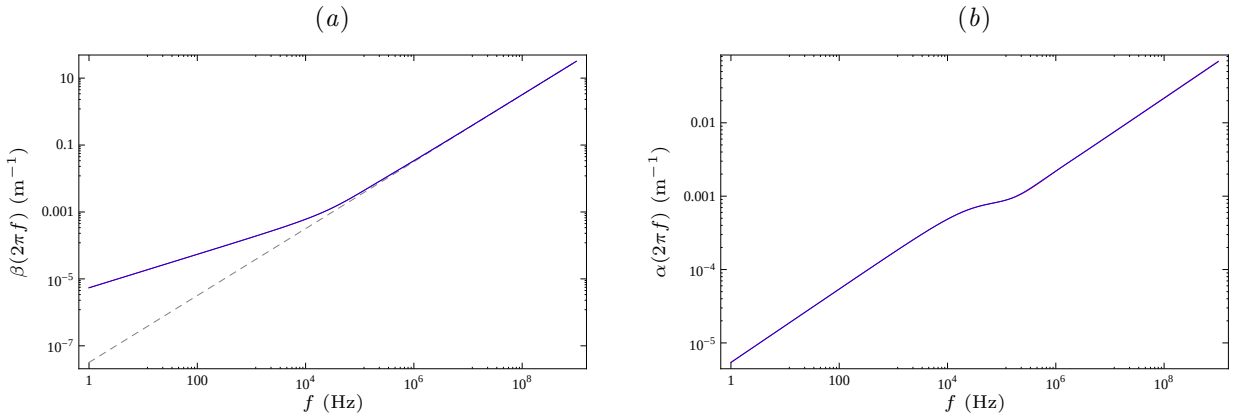

Figure 2.11: Real (a) and imaginary (b) parts of the even (red) and the odd (blue) mode eigenvalues for lossy SUP cable; the dashed line indicates the lossless case.

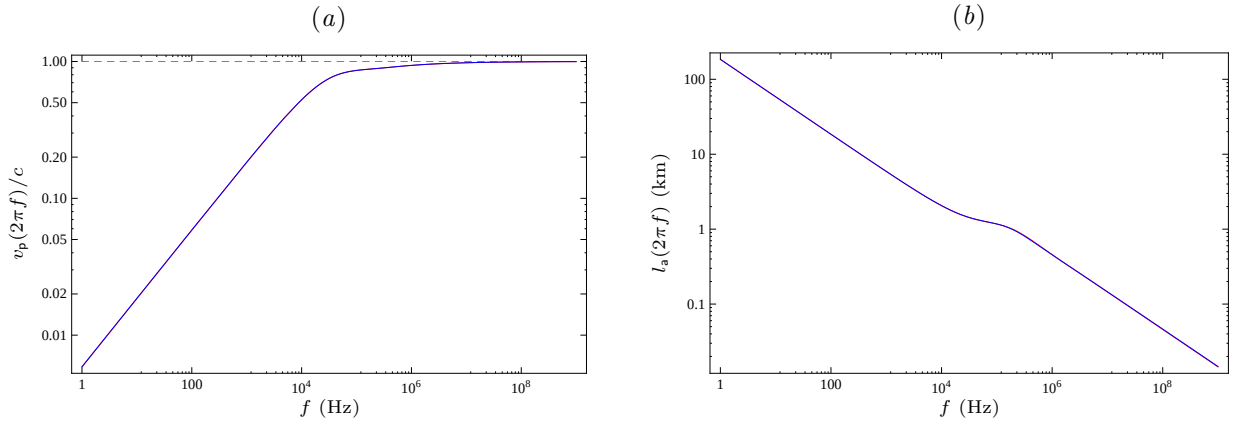

Figure 2.12: Phase velocities (a) and attenuation lengths (b) of the even (red) and the odd (blue) modes for lossy SUP cable. The phase velocity in the (unbounded) insulator is $c = 1/\sqrt{\mu\epsilon} = 1.97677\,10^8$ m/s.

For the parameter values in Table 2.1, and using the expressions (2.60), (2.61), (2.78) and (2.79) derived above for the equivalent-circuit capacitances and impedances, the real and the imaginary parts of the transmission-line mode eigenvalues λ_{x} are plotted in Fig. 2.11. Also of interest are the phase velocities and the attenuation lengths of the modes, defined respectively as

$$v_{\mathsf{p}} \equiv \frac{\omega}{\Re[\lambda]} = \frac{\omega}{\beta},$$
$$l_{\mathsf{a}} \equiv \frac{1}{\Im[\lambda]} = \frac{1}{\alpha};$$

these are plotted in Fig. 2.12. Finally, the characteristic impedances Z_{x} of the two modes are plotted in Fig. 2.13; at 1 GHz, (2.84) and (2.85) evaluate to $Z_{\mathsf{e}} = 53.8786 + \mathrm{i}\,0.11659\ \Omega/\mathrm{m}$ and $Z_{\mathsf{o}} = 39.3419 + \mathrm{i}\,0.0841395\ \Omega/\mathrm{m}$. It is noted that, except for the magnitudes of the characteristic impedances, there is almost no perceptible difference in these quantities between the two modes.

Mode amplitudes

Finally, the heretofore unknown mode amplitudes $V_{\mathsf{x}}^{\pm}$ must be determined from a specification of the source and the load configurations at the two ends of the cable, whose length will be denoted ℓ. Referring to Fig. 2.14, adapted from [73, p. 203], it is assumed that two voltage sources v_{S1} and v_{S2} with internal impedances Z_{S1} and Z_{S2} are connected between conductor 1 and the shield and conductor 2 and the shield, respectively;

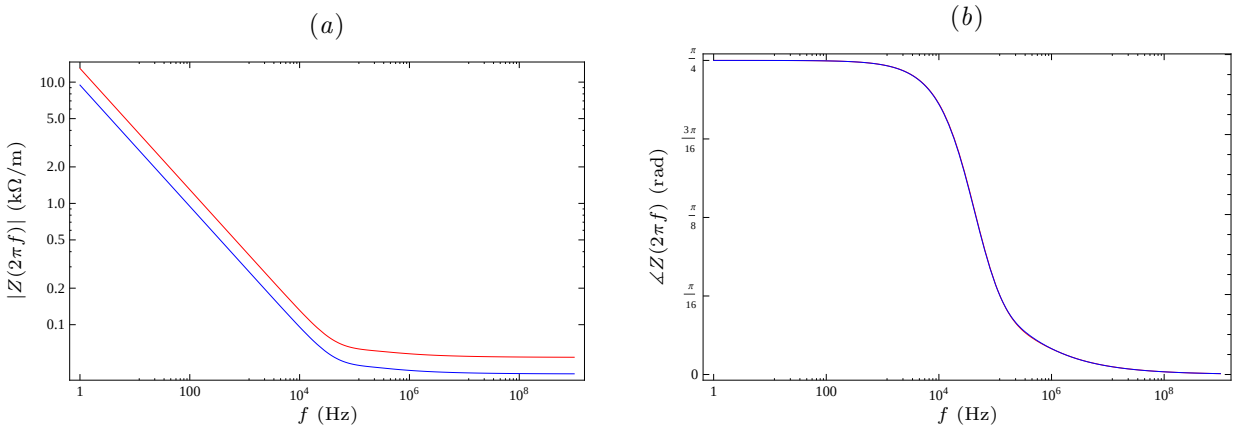

Figure 2.13: Magnitudes (a) and phases (b) of the even (red) and the odd (blue) mode characteristic impedances for lossy SUP cable.

in the most general configuration, the connection to the shield is made via a common impedance $Z_{\mathsf{S}0}$. At the load end, the line is terminated by two impedances $Z_{\mathsf{L}1}$ and $Z_{\mathsf{L}2}$ that are connected, on one hand, to conductors 1 and 2, respectively, and on the other hand to the shield via a common impedance $Z_{\mathsf{L}0}$. That the termination of a transmission line can be modeled in this relatively simple manner may be justified by careful analysis, as shown in KING [73, pp. 58–73].

Writing Kirchhoff's voltage law around the two separate circuits at both the source and the load ends, one obtains the following four equations:

$$\begin{aligned} v_1(0) &= v_{\mathsf{S}1} - Z_{\mathsf{S}1} i_1(0) + Z_{\mathsf{S}0} i_0(0), \\ v_2(0) &= v_{\mathsf{S}2} - Z_{\mathsf{S}2} i_2(0) + Z_{\mathsf{S}0} i_0(0), \\ v_1(\ell) &= Z_{\mathsf{L}1} i_1(\ell) - Z_{\mathsf{L}0} i_0(\ell), \\ v_2(\ell) &= Z_{\mathsf{L}2} i_2(\ell) - Z_{\mathsf{L}0} i_0(\ell). \end{aligned}$$

Remembering that $i_0 = -i_1 - i_2$, and substituting from (2.81) and (2.83), these equations lead to the system

$$\begin{bmatrix} 1 + A_{\mathsf{S}1} & 1 - A_{\mathsf{S}1} & 1 + B_{\mathsf{S}1} & 1 - B_{\mathsf{S}1} \\ 1 + A_{\mathsf{S}2} & 1 - A_{\mathsf{S}2} & -(1 + B_{\mathsf{S}2}) & -(1 - B_{\mathsf{S}2}) \\ (1 - A_{\mathsf{L}1})\,\mathrm{e}^{\mathrm{i}\lambda_{\mathsf{e}}\ell} & (1 + A_{\mathsf{L}1})\,\mathrm{e}^{-\mathrm{i}\lambda_{\mathsf{e}}\ell} & (1 - B_{\mathsf{L}1})\,\mathrm{e}^{\mathrm{i}\lambda_{\mathsf{o}}\ell} & (1 + B_{\mathsf{L}1})\,\mathrm{e}^{-\mathrm{i}\lambda_{\mathsf{o}}\ell} \\ (1 - A_{\mathsf{L}2})\,\mathrm{e}^{\mathrm{i}\lambda_{\mathsf{e}}\ell} & (1 + A_{\mathsf{L}2})\,\mathrm{e}^{-\mathrm{i}\lambda_{\mathsf{e}}\ell} & -(1 - B_{\mathsf{L}2})\,\mathrm{e}^{\mathrm{i}\lambda_{\mathsf{o}}\ell} & -(1 + B_{\mathsf{L}2})\,\mathrm{e}^{-\mathrm{i}\lambda_{\mathsf{o}}\ell} \end{bmatrix} \begin{bmatrix} V_{\mathsf{e}}^{+} \\ V_{\mathsf{e}}^{-} \\ V_{\mathsf{o}}^{+} \\ V_{\mathsf{o}}^{-} \end{bmatrix} = \sqrt{2} \begin{bmatrix} v_{\mathsf{S}1} \\ v_{\mathsf{S}2} \\ 0 \\ 0 \end{bmatrix}, \tag{2.86}$$

where, with $\mathsf{X} = \mathsf{S}, \mathsf{L}$ and $j = 1, 2$,

$$\begin{aligned} A_{\mathsf{X}j} &= \frac{Z_{\mathsf{X}j} + 2Z_{\mathsf{X}0}}{Z_{\mathsf{e}}}, \\ B_{\mathsf{X}j} &= \frac{Z_{\mathsf{X}j}}{Z_{\mathsf{o}}}. \end{aligned}$$

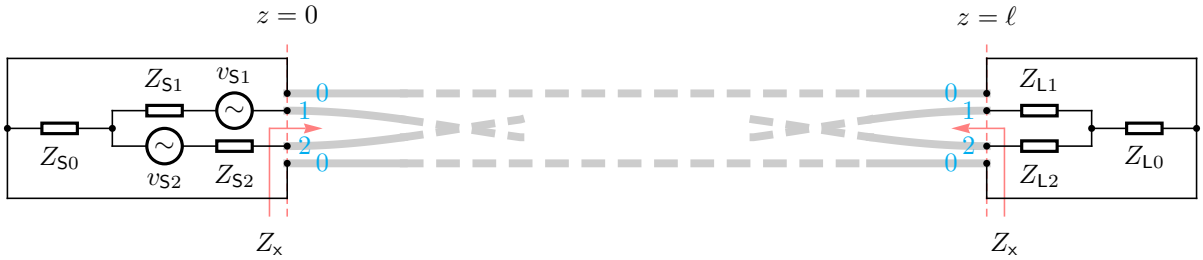

Figure 2.14: A transmission-line circuit featuring STP cable.

The general solution of (2.86) is readily found but rather cumbersome to write down; the result simplifies considerably for the practically interesting case of "balanced" source and load configurations, for which $Z_{\mathsf{S}1} = Z_{\mathsf{S}2} \equiv Z_{\mathsf{S}}$ and $Z_{\mathsf{L}1} = Z_{\mathsf{L}2} \equiv Z_{\mathsf{L}}$, yielding

$$\begin{bmatrix} V_{\mathsf{e}}^{+} \\ V_{\mathsf{e}}^{-} \end{bmatrix} = \frac{Z_{\mathsf{e}}}{Z_{\mathsf{S}} + 2Z_{\mathsf{S}0} + Z_{\mathsf{e}}} \frac{1}{1 - \Gamma_{\mathsf{Se}}\Gamma_{\mathsf{Le}}\,\mathrm{e}^{\mathrm{i}2\lambda_{\mathsf{e}}\ell}} \begin{bmatrix} 1 \\ \Gamma_{\mathsf{Le}} \end{bmatrix} \frac{v_{\mathsf{S}1} + v_{\mathsf{S}2}}{\sqrt{2}}, \tag{2.87}$$

$$\begin{bmatrix} V_{\mathsf{o}}^{+} \\ V_{\mathsf{o}}^{-} \end{bmatrix} = \frac{Z_{\mathsf{o}}}{Z_{\mathsf{S}} + Z_{\mathsf{o}}} \frac{1}{1 - \Gamma_{\mathsf{So}}\Gamma_{\mathsf{Lo}}\,\mathrm{e}^{\mathrm{i}2\lambda_{\mathsf{o}}\ell}} \begin{bmatrix} 1 \\ \Gamma_{\mathsf{Lo}} \end{bmatrix} \frac{v_{\mathsf{S}1} - v_{\mathsf{S}2}}{\sqrt{2}}, \tag{2.88}$$

where the reflection coefficients are defined as

$$\begin{aligned} \Gamma_{\mathsf{Xe}} &= \frac{Z_{\mathsf{X}} + 2Z_{\mathsf{X}0} - Z_{\mathsf{e}}}{Z_{\mathsf{X}} + 2Z_{\mathsf{X}0} + Z_{\mathsf{e}}}, \\ \Gamma_{\mathsf{Xo}} &= \frac{Z_{\mathsf{X}} - Z_{\mathsf{o}}}{Z_{\mathsf{X}} + Z_{\mathsf{o}}}. \end{aligned}$$

Concept of operation

Note from (2.87) and (2.88) that the even-mode and the odd-mode amplitudes are proportional to the sum and the difference, respectively, of the two source signals, a separation that occurs only in the special case of balanced source *and* load terminations considered above. This observation motivates the definition of the *common*-mode and the *differential*-mode voltages and currents (see, *e.g.*, [77] or [71, p. 37])

$$\begin{aligned} v_{\mathsf{c}} &\equiv \tfrac{1}{2}\,(v_1 + v_2), & v_{\mathsf{d}} &\equiv v_1 - v_2, \\ i_{\mathsf{c}} &\equiv i_1 + i_2, & i_{\mathsf{d}} &\equiv \tfrac{1}{2}\,(i_1 - i_2). \end{aligned}$$

These definitions are especially useful in analyzing experiments where a single source is used to excite the cable (see §4.2). Introducing the new voltage and current vectors

$$\begin{aligned} \mathbf{u} &\equiv \begin{bmatrix} v_{\mathsf{c}} \\ v_{\mathsf{d}} \end{bmatrix} = \begin{bmatrix} \frac{1}{2} & \frac{1}{2} \\ 1 & -1 \end{bmatrix} \mathbf{v}, \\ \mathbf{j} &\equiv \begin{bmatrix} i_{\mathsf{c}} \\ i_{\mathsf{d}} \end{bmatrix} = \begin{bmatrix} 1 & 1 \\ \frac{1}{2} & -\frac{1}{2} \end{bmatrix} \mathbf{i}, \end{aligned}$$

and substituting from (2.81) and (2.83), one finds that

$$\begin{aligned} \mathbf{u}(z) &= \big(U_{\mathsf{c}}^{+}\,\mathrm{e}^{\mathrm{i}\lambda_{\mathsf{e}}z} + U_{\mathsf{c}}^{-}\,\mathrm{e}^{-\mathrm{i}\lambda_{\mathsf{e}}z}\big)\mathbf{y}_{\mathsf{c}} + \big(U_{\mathsf{d}}^{+}\,\mathrm{e}^{\mathrm{i}\lambda_{\mathsf{o}}z} + U_{\mathsf{d}}^{-}\,\mathrm{e}^{-\mathrm{i}\lambda_{\mathsf{o}}z}\big)\mathbf{y}_{\mathsf{d}}, \\ \mathbf{j}(z) &= \frac{1}{Z_{\mathsf{c}}}\,\big(U_{\mathsf{c}}^{+}\,\mathrm{e}^{\mathrm{i}\lambda_{\mathsf{e}}z} - U_{\mathsf{c}}^{-}\,\mathrm{e}^{-\mathrm{i}\lambda_{\mathsf{e}}z}\big)\mathbf{y}_{\mathsf{c}} + \frac{1}{Z_{\mathsf{d}}}\,\big(U_{\mathsf{d}}^{+}\,\mathrm{e}^{\mathrm{i}\lambda_{\mathsf{o}}z} - U_{\mathsf{d}}^{-}\,\mathrm{e}^{-\mathrm{i}\lambda_{\mathsf{o}}z}\big)\mathbf{y}_{\mathsf{d}}, \end{aligned}$$

where the new characteristic impedances and basis vectors are

$$\begin{aligned} Z_{\mathsf{c}} &= \tfrac{1}{2}\,Z_{\mathsf{e}}, & Z_{\mathsf{d}} &= 2Z_{\mathsf{o}}, \\ \mathbf{y}_{\mathsf{c}} &= [1 \quad 0]^{\mathrm{T}}, & \mathbf{y}_{\mathsf{d}} &= [0 \quad 1]^{\mathrm{T}}, \end{aligned}$$

and the new mode amplitudes are given by

$$\begin{bmatrix} U_{\mathsf{c}}^{+} \\ U_{\mathsf{c}}^{-} \end{bmatrix} = \frac{Z_{\mathsf{e}}}{Z_{\mathsf{S}} + 2Z_{\mathsf{S}0} + Z_{\mathsf{e}}} \frac{1}{1 - \Gamma_{\mathsf{Se}}\Gamma_{\mathsf{Le}}\,\mathrm{e}^{\mathrm{i}2\lambda_{\mathsf{e}}\ell}} \begin{bmatrix} 1 \\ \Gamma_{\mathsf{Le}} \end{bmatrix} \frac{v_{\mathsf{S}1} + v_{\mathsf{S}2}}{2},$$

$$\begin{bmatrix} U_{\mathsf{d}}^{+} \\ U_{\mathsf{d}}^{-} \end{bmatrix} = \frac{Z_{\mathsf{o}}}{Z_{\mathsf{S}} + Z_{\mathsf{o}}} \frac{1}{1 - \Gamma_{\mathsf{So}}\Gamma_{\mathsf{Lo}}\,\mathrm{e}^{\mathrm{i}2\lambda_{\mathsf{o}}\ell}} \begin{bmatrix} 1 \\ \Gamma_{\mathsf{Lo}} \end{bmatrix} (v_{\mathsf{S}1} - v_{\mathsf{S}2}).$$

A possible concept of operation is to send a "message" signal v_{m} for communication, while simultaneously sending a "test" signal v_{t} down the line for monitoring the health of the cable. Although not discernible from Fig. 2.12, the odd mode is the slightly faster and less attenuated of the two transmission-line modes. Note also from Fig. 2.5 that, for the even mode, the current flow on the shield is slightly less nonuniform over the azimuth, thus making it more sensitive to shield imperfections such as chafing. For these reasons, it seems sensible to assign the message signal to the differential mode, while the test signal is transmitted via the common mode. Thus, in the balanced case, the source signals may be taken as

$$\begin{aligned} v_{\mathsf{S}1} &= v_{\mathsf{t}} + \tfrac{1}{2}\, v_{\mathsf{m}}, \\ v_{\mathsf{S}2} &= v_{\mathsf{t}} - \tfrac{1}{2}\, v_{\mathsf{m}}. \end{aligned}$$

2.4 Twisted cable

2.4.1 Eigenvalues

For finite p, the waveguide geometry is that of STP cable. In a typical cable, the twisting of the wires is very gradual in comparison with the transverse dimension (*i.e.*, $p \gg r_{\mathsf{i}}$), and therefore the eigenvalues and the corresponding fields for the modes of STP cable may be expected, at least over the spectral region of interest, to behave substantially like those of SUP cable discussed in §2.2. Specifically, for the transmission-line modes of STP cable, one expects to find $\lambda \gtrsim k$. Furthermore, for the parameter values in Table 2.1, one has that $\kappa \gg k$ up to 1 GHz. Consequently, one may adopt the approximation $\gamma_m \simeq |m|\kappa$ in (2.24). Noting that the modified Bessel functions and their derivatives obey the reflection relation $W_{-m}(x) = W_m(x)$, and making use of the corresponding large-order approximations [68, p. 378], (2.25) thus becomes

$$\Lambda(\omega, \lambda) \simeq \left[\left(\frac{\lambda}{k} \right)^2 \frac{1}{\sqrt{1 + (\kappa r_{\mathsf{c}})^2}} - \sqrt{1 + (\kappa r_{\mathsf{c}})^2} \right] \sum_m \frac{1}{m} \left\{ \mathrm{e}^{-2m[\Xi(r_{\mathsf{i}}) - \Xi(r_{\mathsf{c}})]} - 1 \right\} = 0, \tag{2.89}$$

where m runs over positive even (odd) values for the even (odd) mode, and

$$\Xi(\rho) = \sqrt{1 + (\kappa\rho)^2} + \ln \left[\frac{\kappa\rho}{1 + \sqrt{1 + (\kappa\rho)^2}} \right].$$

It should perhaps be noted that, for the even mode, the $m = 0$ term in (2.25) must be treated separately using small-argument approximations for Bessel functions. The contribution of this term becomes ultimately immaterial, however, since the sum in (2.89) is technically divergent. The eigenvalue is therefore determined by the factor outside the sum, giving simply

$$\lambda = \pm k \sqrt{1 + (\kappa r_{\mathsf{c}})^2}. \tag{2.90}$$

Remembering that $\sqrt{1 + (\kappa r_{\mathsf{c}})^2} = 1/\sin\psi$, it is observed that, at least to this order of approximation, the multiplicative "correction" of (2.90) to the eigenvalues of the transmission-line modes of SUP cable is purely geometric (*i.e.*, independent of frequency), and essentially accounts for the elongated path the fields must travel along the twisted wires in STP cable. It is also intuitively satisfying to note that the correction depends on κ through an even power, and is therefore insensitive to the sense of the twist (*i.e.*, the sign of κ), as one would expect on physical grounds. Using the parameter values in Table 2.1, the radical in (2.90) evaluates to 1.01261 (1.0101) for the even (odd) mode, revealing that the correction is indeed slight. Note that the most prominent feature of periodic structures, namely the forbidden spectral regions known as "stop bands" wherein axial wave propagation ceases, is *not* observed. As was anticipated by early workers [49], this feature is eliminated here by the presence of the shield, which traps the radiation that would flow out radially in these frequency bands if the cable were an "open" structure.

2.4.2 Mode fields

The exact field solutions given in §2.1 may now be evaluated with (2.90) to the same order of accuracy as (2.89), making use of both small-argument and large-order approximations for the Bessel functions. Note

that it is important to properly account for the $m = 0$ term here. This procedure leads to approximate analytical expressions for the mode fields that are, unfortunately, rather unwieldy to include here. It is therefore merely noted that these approximate solutions exhibit a slight twist compared with the field plots for SUP cable given in §2.2.2, but are otherwise of the same general character. This result, corroborated by exact numerical solutions (see §3.5), was to be expected given the very small twist rate of the wires typical for STP cables.

Finally, it seems reasonable to expect that the equivalent-circuit model for SUP cable may be useful for STP cable as well. If the development of §2.3 is followed with the new eigenvalue (2.90) and without regard to the small axial field components that appear as a result of twisting, it is found that the per-unit-length line parameters $\mathbf{C}$, $\mathbf{G}$, $\mathbf{L}$, and $\mathbf{Z}$ are all increased by the factor $1/\sin\psi$, which is consistent with the geometric argument presented above. Consequently, the eigenvalues for the transmission-line modes of *lossy* STP cable may be obtained simply by multiplying (2.82) by the same factor, leading to a small increase in attenuation along with the small reduction in phase velocity indicated by (2.90). (The characteristic impedances Z_{x} remain the same, as they involve ratios of the per-unit-length line impedances to the eigenvalues.)

Chapter 3

Simulation

3.1 Overview

Electromagnetic wave propagation simulations are presented as performed with COMSOL Multiphysics simulation software (version 4.2) with the RF and the AC/DC modules. The purpose of the simulations is to characterize the cables as a function of frequency in both unfaulted and faulted conditions. This characterization can then be compared with the theoretical derivations as part of a validation process. The results can also be used as part of a trade-space assessment for diagnostic tool development for STP cable.

3.2 Geometric fidelity

Different representations of the geometry of STP cable were considered. These representations were examined in order to determine the greatest level of agreement between the actual cable and the simulator while allowing for the computations (or more specifically the memory usage) to be practical. All simulations were performed on a dual quad core Intel Xeon W5590 @ 3.33 GHz computer equipped with 192 GB of RAM.

There are essentially two different kinds of STP cable: impedance controlled and non-impedance controlled. The difference between these two types of cables is the uniformity of the spacing between the inner conductors and the shield. The non-impedance controlled cable can have flat faces and the impedance controlled cable has been manufactured to be round. From a modeling perspective, we examined four variations as shown in Fig. 3.1. The first is the most practical from an analytical perspective, it has a perfectly round shield filled with dielectric and two twisting conductors. In practice, the cable actually has air gaps between the dielectrics on the wires and the shield. The early days of analytical wave propagation analysis also included approximating the inner conductors with infinitely thin metallic tapes. We simulated all of these including the non-impedance controlled (flat) configuration.

The theoretical model had dimensions corresponding to a shield radius of 1.5 mm, a dielectric radius of

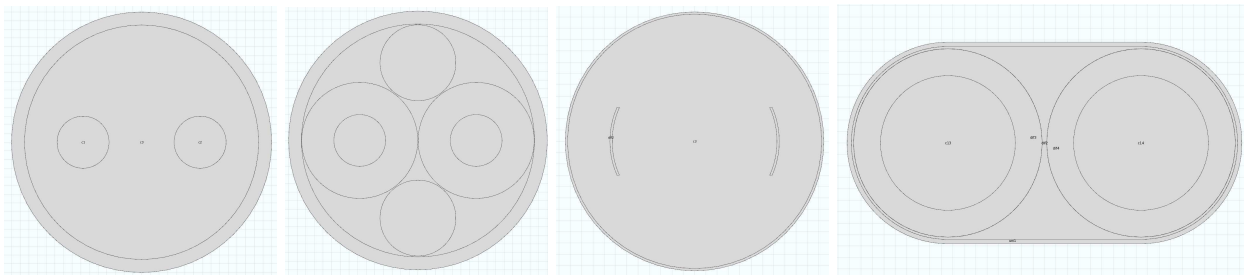

Figure 3.1: Cross-sections of simulated cable geometries. On the left is the geometry corresponding to the theoretical model, next has the inclusion of air, and to the right are the typical tape approximation and the flat non-impedance controlled cable.

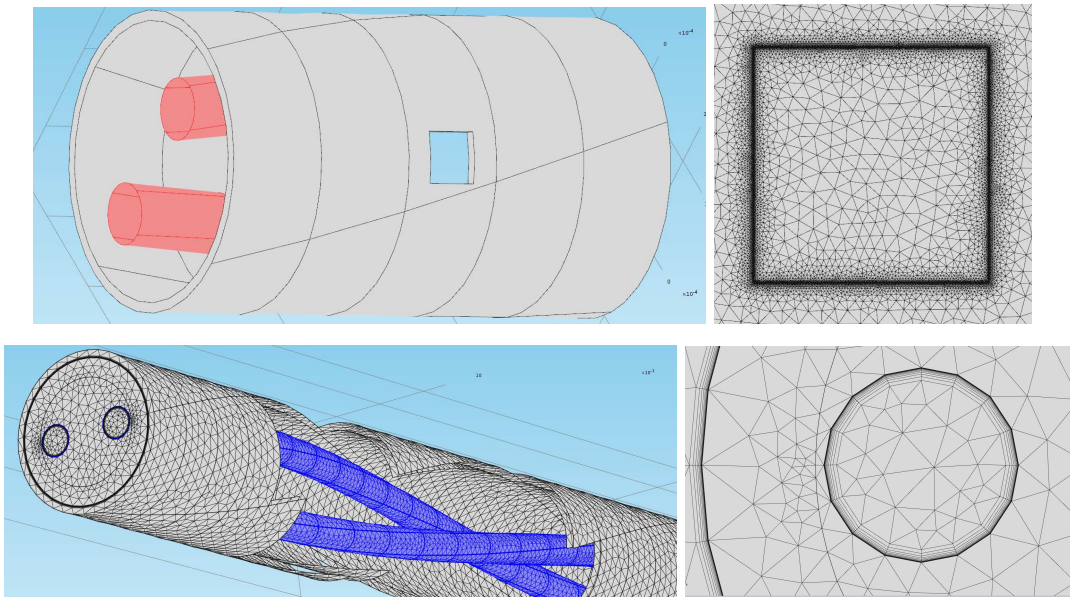

Figure 3.2: Meshes for STP cable and hole fault. Top left shows the hole in the shield. Top right shows the meshing detail for the hole and the density near the edges. Bottom left shows the mesh, including the boundary layer mesh, for the whole 3D structure. Bottom right shows the boundary layer meshes for part of the shield and one conductor.

1.35 mm, and core conductors of 0.3 mm. One 360-degree rotational twist occurred within a 30 mm length. The impedance controlled model, which included air, had the dielectric radius around each conductor as 0.675 mm. All other parameters were equal to the theoretical model analyzed in §2. The electrical parameters were consistent across models. The relative permittivity of the insulation was 2.3, and the conductivity of the copper was $5.998\,10^7$ S/m.

3.3 Mesh

Most of the 3D simulations presented will rely upon the simplest geometric model. The mesh for this model is presented in Figure 3.2. The mesh consisted of four different levels of spatial resolution in order to resolve the fields of interest. The perfectly matched layer absorber at the end of the cable is not shown. The unfaulted shielded twisted pair had a maximum swept mesh spacing of $1.09\,10^{-4}$ m. For the cases with a hole fault, the square holes were modeled with a high-density mesh at the very edges for 2 μm, the rest of the volume of the hole was at 40 μm. A typical 60 mm length of cable without faults used 1.3 million elements representing 18.1 million degrees of freedom. The analyses with faults used much shorter lengths of cable (typically 5 mm) in order to have enough memory for the iterative solver. These numbers do not include when boundary layer meshes were added to facilitate modelling the submicron skin effects for the attenuation calculations. The boundary layer mesh shown in Fig. 3.2 (and described later in more detail) resulted in using 892,000 elements so that only a 30 mm length of cable for the attenuation analysis was able to fit within memory using an iterative solver.

For the 2D analyses the capacitances were solved for by using a direct MUMPS solver. The 3D eigenfrequency analyses were also performed with a direct MUMPS solver. The 3D field solutions for the cables with a shield hole fault were calculated using a stationary iterative solver in the frequency domain based upon GMRES with a geometric multigrid. The iterative solver was necessary due to the large memory requirements, which were in excess of the machine's capability for a direct solution.

3.4 2D analysis

The first analysis consists of a 2D (Laplace) solution of the fields in order to determine the capacitance. The calculated capacitances are shown in Table 3.1 and the resulting fields are shown in Fig. 3.3.

The capacitance of the theoretical model and the impedance-controlled model (with air) are within 10 % of each other and so it seems that the theoretical approximation is close. The tape model is further away from these capacitances and has magnitudes of the electric fields that are significantly peaked due to the thin edges. The flat (non-impedance controlled) cable is significantly different as expected. The magnitude of the fields is important when we go on to consider the magnitude of the fields in the hole faults. If the fields are significantly stronger (*e.g.*, tape) than that expected analytically, the expected reflections will be significantly in error. The tape model and the flat non-impedance controlled model will not be discussed further in our presentation of the simulation results.

Table 3.1: Capacitances from 2D analysis.

Model	**Self Capacitance** (pF)	**Mutual Capacitance** (pF)
theoretical STP cable	111.616	−17.511
STP cable with foam & air	95.7642	−17.8204
flat STP cable	257.0246	−25.1478
tape	89.0881	−5.4137

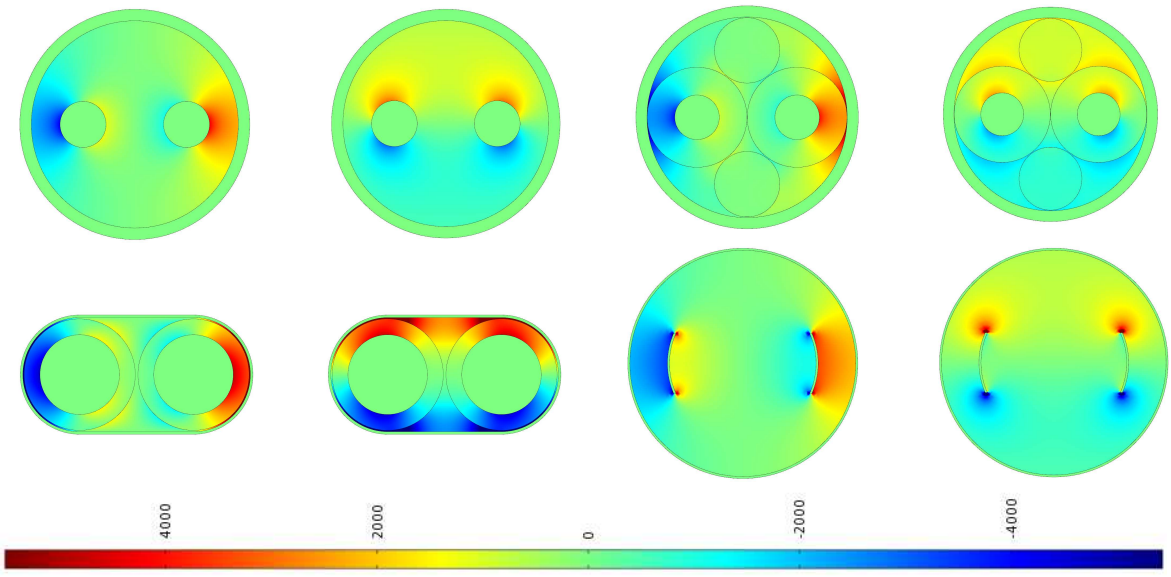

Figure 3.3: Pairs of real E_x (left) and real E_y (right) fields for the even mode. Note that red represents 5000 V/m and blue represents −5000 V/m.

3.5 3D analysis

A full 3D segment representing more than one complete twist was analyzed in COMSOL to determine the dominant modes of propagation. An eigenfrequency analysis was conducted on 180 mm of coaxial cable (configured as RG-58), on the theoretical STP cable with lengths ranging from 90 mm to 360 mm, 90 mm

of STP cable with foam and air (shorter due to increased mesh elements), and 180 mm of SUP cable. The computed eigenvalues at the resulting frequencies are presented in Tables 3.2 and 3.3 for the two primary modes (even and odd) of the three-conductor cable. The transverse electric fields for these results are presented in Fig. 3.4. Table 3.3 modeled the high-frequency skin effect, and so it also includes attenuation. It was also confirmed that these computed eigenvalues agree very well with the theoretical model of §2 up to—and possibly beyond—10 GHz.

Table 3.2: Eigenvalues from 3D analysis.

Model	**Frequency** (GHz)	**Odd-mode** $\Re[\lambda]$ (1/m)	**Even-mode** $\Re[\lambda]$ (1/m)
coaxial cable	0.552	17.36	
coaxial cable	1.10	34.56	
STP cable with air	5.98	19.01	19.89
STP cable with air	1.79	57.02	59.67
SUP cable	5.49	17.45	17.45
SUP cable	1.10	34.80	34.79

Table 3.3: STP cable eigenvalues from 3D analysis for theoretical model.

Frequency (GHz)	**Odd-mode** λ (1/m)	**Even-mode** λ (1/m)
0.54	$17.1452 + \mathrm{i}\,0.0522$	$17.2476 + \mathrm{i}\,0.0515$
1.62	$51.4973 + \mathrm{i}\,0.0809$	$51.8045 + \mathrm{i}\,0.0813$
2.7	$85.8547 + \mathrm{i}\,0.0958$	$86.3679 + \mathrm{i}\,0.0977$
3.8	$120.2127 + \mathrm{i}\,0.1056$	$120.9327 + \mathrm{i}\,0.1091$
4.9	$154.5704 + \mathrm{i}\,0.113$	$155.498 + \mathrm{i}\,0.118$
5.9	$188.9276 + \mathrm{i}\,0.119$	$190.0636 + \mathrm{i}\,0.1254$
7.1	$223.284 + \mathrm{i}\,0.124$	$224.6293 + \mathrm{i}\,0.1318$
8.1	$257.6396 + \mathrm{i}\,0.1284$	$259.1952 + \mathrm{i}\,0.1375$
9.2	$291.9943 + \mathrm{i}\,0.1324$	$293.7612 + \mathrm{i}\,0.1428$

The transverse electric field resulting from the mode analysis was compared with the solution of the Laplace equation in order to assess whether it was representative of the even mode or the odd mode. A careful examination of Fig. 3.4 reveals the asymmetrical effects of the twists on the fields in the first pair of images as opposed to the last pair that are untwisted. The subtlety of the change in fields between twisted and uniform conductors is also revealed by the similarity in eigenvalues between the twisted and untwisted cases. The inclusion of air in the impedance controlled model produces a minor change in the eigenvalues. (Note that the frequencies reported in the two tables are different due to the inherent differences in velocity of propagation and lengths of samples simulated.)

The calculation of the attenuation in STP cable required significantly more attention to the meshing of the skin of the conductors and the shield. Within the mesh generator in COMSOL is a feature to create boundary layer meshes. This feature was used to generate a boundary layer mesh specified to have 15 layers with a stretching factor of 1.4 and a starting mesh size of 10^{-7} m. This resulted in boundary mesh layers at approximately 0.1, 0.24, 0.44, 0.71, 1.09, 1.63, 2.39, 3.44, 4.92, 6.98, 9.87, 13.92, 19.59, 27.53, 38.64 μm.

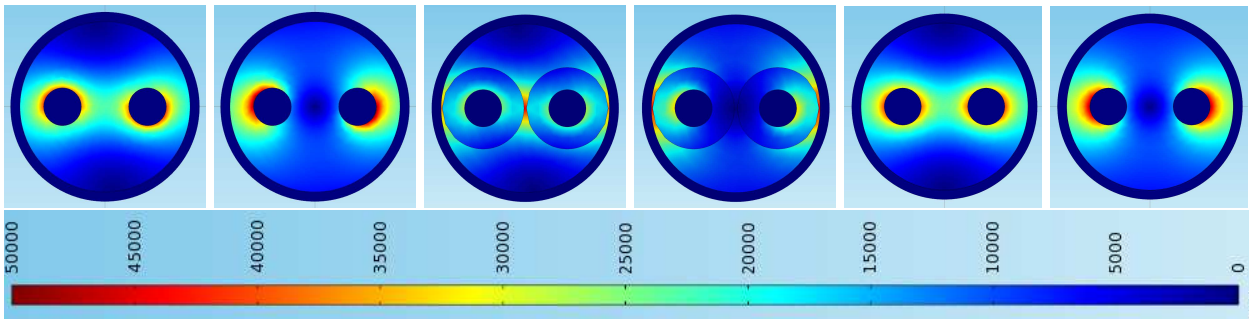

Figure 3.4: From left to right, the first pair of plots depicts the magnitude of the transverse electric field for the first two eigenmodes of the theoretical STP cable; the second pair is the impedance controlled cable which has air between the dielectrics; the third pair is the SUP cable. All plots are scaled 0 to 50,000 V/m.

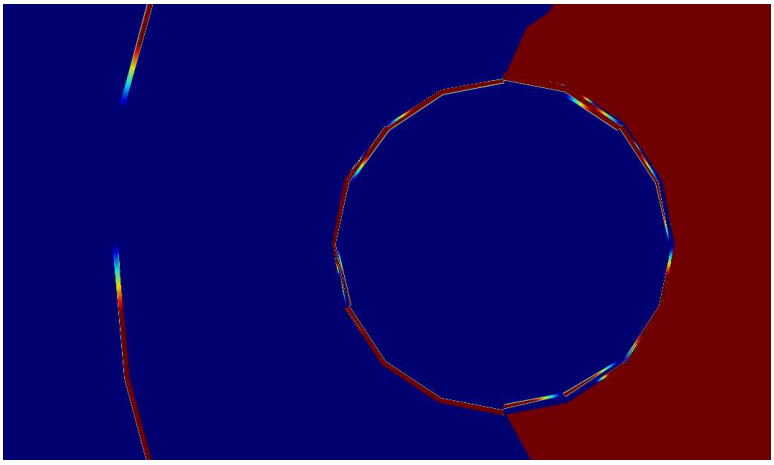

Figure 3.5: Electric field penetration into the metals via the boundary layer mesh of 3.44 to 4.92 μm at 300 MHz.

Obviously, the conductors are thicker than 38 μm, so the rest of the volume of the conductors and the shield are represented with tetrahedral elements.

A rough estimate of skin depth $\sqrt{2/(\omega\mu\sigma)}$ ranges from 3.75 μm at 300 MHz, to 2.06 μm at 1.0 GHz and to 1.02 μm at 4 GHz. The dynamic range of the electric field penetrating into the metal was roughly $\pm 10^{-3}$ V/m. Fig. 3.5 depicts the electric field within the metal at 300 MHz (the maximum depth of penetration). The simulation resulted in depths in the range of 3.44 to 4.92 μm for 300 MHz, 2.39 to 3.44 μm for 1 GHz, and 1.09 to 1.63 μm for 4 GHz. The simulation tended to allow greater penetration because the mesh could not be made fine enough to truly represent the skin effect. A coarser mesh forces the fields to exist deeper into the metals than usually occurs, but due to computer memory limitations, the mesh density was deemed adequate given the penetration ranges.

The eigenanalysis with this boundary layer mesh resulted in an attenuation of 0.052/m at 540 MHz and 0.081/m at 1.63 GHz. A frequency-domain simulation using this mesh was then performed with a TEM source (*i.e.*, a coaxial port) to obtain the scattering parameters for the common mode. The throughput for a $\ell = 30$ mm length of STP cable, given by $-\ln|S_{21}|/\ell$, is plotted in Figure 3.6 along with the linear loss from the eigenanalysis. The key point to examine in this figure is where S_{21} dips to its lowest where it approaches the linear attenuation, which matches closely with the attenuation line drawn using the lossy part of the eigenvalues. (The oscillatory behavior of S_{21} is due to the mismatched terminations at the two ends of the cable.)

The theoretical analytic model compares well with the simulation results as shown by examining the transverse fields of the analytical model for SUP cable with the transverse fields of the 2D simulation and

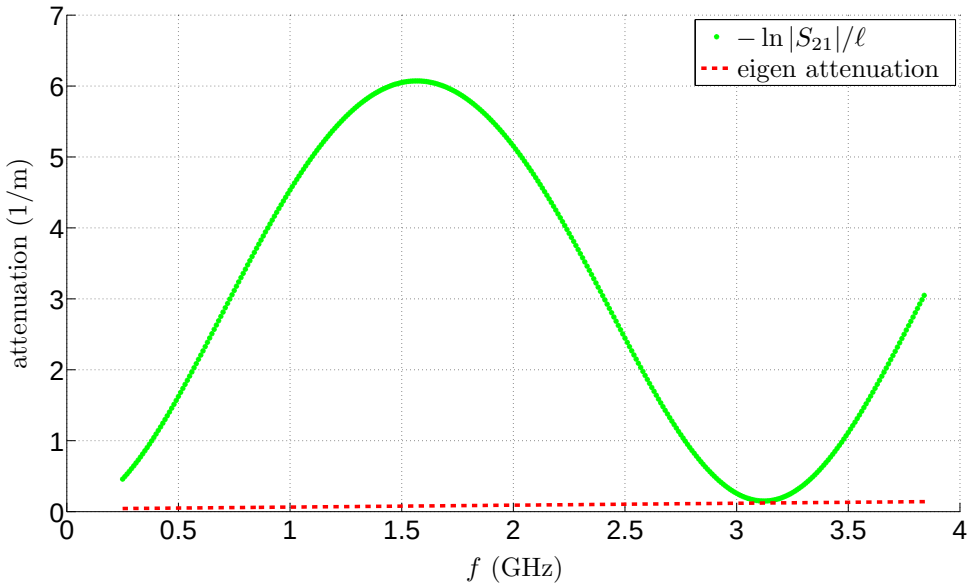

Figure 3.6: Attenuation per meter in theoretical STP cable. Shown for a 30 mm length of cable are the through scattering parameter $-\ln|S_{21}|/\ell$, and the linear loss line derived from the eigen-analysis.

the frequency based simulations for the full 3D simulation model. Figs. 3.7 and 3.8 show the profiles of the real part of E_x when following along the x-axis, and the real part of E_y when following along parallel to the y-axis through conductor 1. The E_x profiles show three field regions from left to right: between shield and left conductor, between conductors, and finally between the right conductor and the shield. E_x matches closely with the analytical model (6 % error) when near the shield and shows the greatest error when closest to a conductor (19 % error). The most important region for accuracy of detecting a shield hole is the field between the conductor and the shield. The E_y profiles show two field regions: the fields between the bottom of the right conductor and the shield, and the fields between the top of the right conductor and the shield. Again, the agreement is close between theory and 2D simulation (1 % error) when closest to the shield, and the error is greatest near the conductor (7 % error). The error closest to the conductor in both cases is due to the filament approximation to the round conductor. The fields at 1 GHz naturally diverge away from the lossless 2D solution, and are shown to emphasize that the loss with respect to frequency dominates most other effects.

3.6 Chafe faults

Since the angular positions of the conductors within STP cable change as a function of length, the field intensity rotates with distance along the cable. Thus, when determining fault characteristics, we have to consider not only distance to fault and the size of the fault but also the angular position of the fault, which can cause substantial variations in reflection depending upon whether it is close to a conductor or far away.

This key point is illustrated in Fig. 3.9, which plots E_y for three discrete hole angles. The faulted specimen was 5 mm in length with the fault centered at 2.5 mm. The angle of rotation of the conductors was 12 degrees per millimeter. Thus, the center of a hole located on the x-axis at 2.5 mm is at -30 degrees with respect to the axis running through the conductors. The other two angles were at -75 and 15 degrees. The wave propagation was initiated by specifying E_x and E_y in the dielectric at one end of the cable. The initial values of E_x and E_y were taken from the mode analysis solution for the primary eigenvalue of even mode propagation.

The fields escaping through the hole are determined mainly by E_z in the hole. Fig. 3.10 displays the E_z field along the centerline of the hole running on the z-axis (direction of propagation) for the three hole positions. Note that the peak fields at 15 degrees are more than two times in magnitude compared with

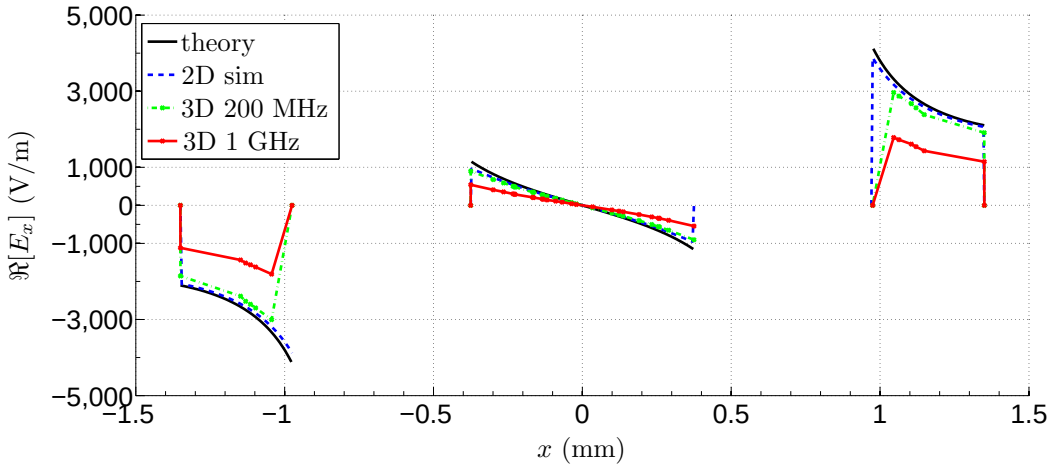

Figure 3.7: Profile of real E_x parallel to x-axis for analytical theory, 2D simulation, 3D simulation at 300 MHz, and 3D simulation at 1 GHz.

those at -75 degrees. These peak fields, when adjusted by the area of the fault, are proportional to the expected magnitude of reflection from these faults. This implies that it may be possible to have a small fault near a conductor be nearly equal in reflection magnitude to a larger size hole fault that is farther away from the conductors. These multiple possibilities would then require that any fault parameterization search routine be able to cope with such an ambiguity.

In order to quickly take advantage of the changes with respect to fault angle, a capacitance look-up table was created by solving the Laplace equation for the impedance-controlled cable (including air). Note that, since this is a 2D calculation, the effects of twist are not captured. Table 3.4 lists the resulting capacitances for both conductors with different sized faults at discrete angles. The fault size of 3 mm represents half of the shield without intrusion into the dielectric. We could have chosen to also abrade/remove the dielectric, but this would have had a greater impact on the results. Thus, by not removing the dielectric, it is possible to examine the least detectability inherent within the problem.

Table 3.4: Capacitances (in pF) with faults for the even mode of impedance controlled STP cable with air but no foam.

Hole size (mm)	**Angle** = 0 deg.	**Angle** = 45 deg.	**Angle** = 90 deg.
0.0	71.476, 71.476		
0.5	71.464, 66.000	71.436, 70.894	71.383, 71.383
1.0	71.422, 55.682	71.310, 68.863	71.066, 71.066
2.0	71.181, 37.979	70.729, 55.760	69.144, 69.144
2.5	70.847, 31.002	70.062, 42.379	66.001, 66.001

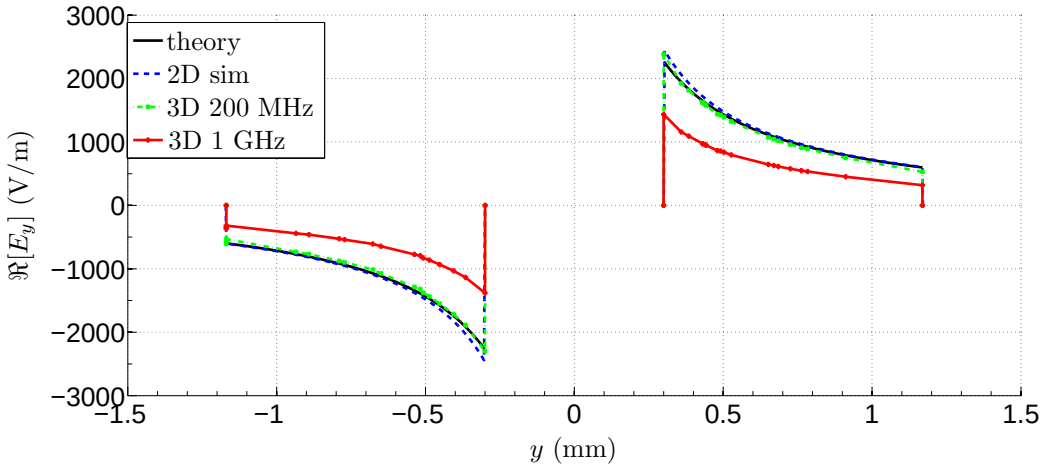

Figure 3.8: Profile of real E_y running parallel to y-axis through center of right conductor for analytical theory, 2D simulation, 3D simulation at 300 MHz, and 3D simulation at 1 GHz.

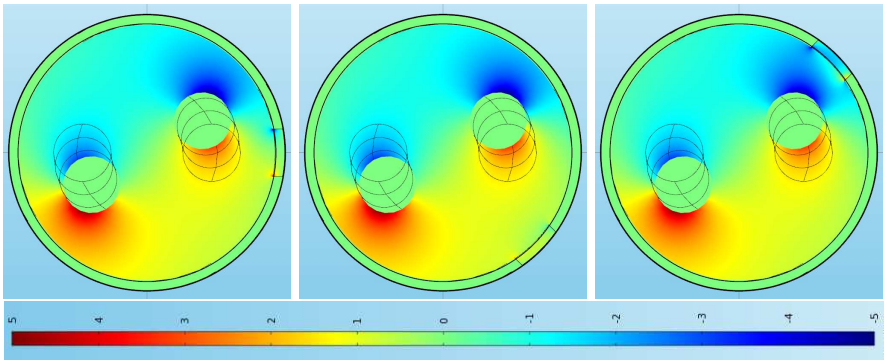

Figure 3.9: E_y field strength at 2 GHz with hole at -30, -75 and 15 degrees from axis formed by conductors.

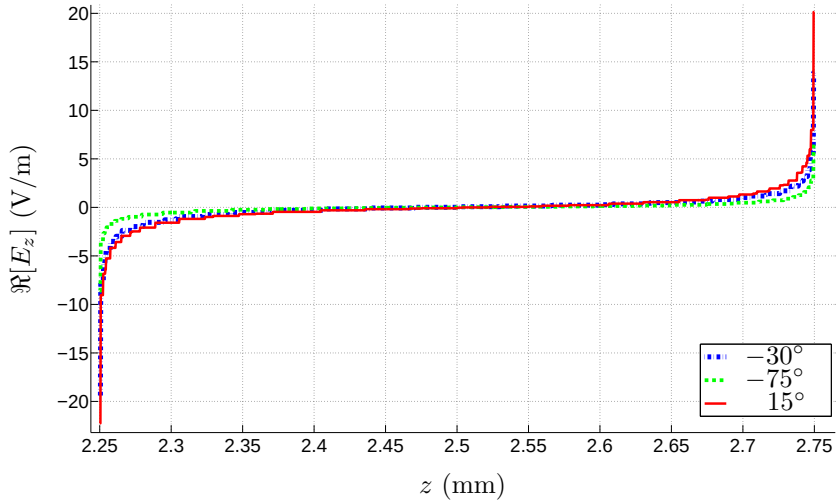

Figure 3.10: Real part of E_z along the centerline of hole for three different angular hole positions.

Chapter 4

Experiment

4.1 Overview

Before the theoretical model can be compared with experiment, the effects of the measurement setup itself must be incorporated to produce a complete model for the entire system that includes instrument impedance mismatch, measurement delays, and a small degree of allowable miscalibration, all of which significantly affect the measured signal by a much greater margin than the chafe faults we aim to detect. This overall system model will now be developed within the S-parameter framework detailed in [78]. Optimal estimation of the unknown or uncertain cable and measurement setup parameters from laboratory data will then be couched as a Bayesian inference problem, whose solution will be demonstrated by several examples.

4.2 System model

4.2.1 Common-mode cable model

As discussed in §2.3.5, of the two transmission-line modes of STP cable, the common mode is more suitable for the diagnostic assessment of cable health. The pertinent model parameters for common-mode excitation of STP cable are the twist-corrected axial eigenvalue

$$\lambda_{\mathsf{c}} = \frac{\lambda_{\mathsf{e}}}{\sin\psi} = \sqrt{[1+(\kappa r_{\mathsf{ce}})^2]\left[\mathrm{i}\omega\mu(\sigma-\mathrm{i}\omega\epsilon) - \left(\frac{\sigma}{\epsilon}-\mathrm{i}\omega\right)(z_{\mathsf{s}}+z_{\mathsf{m}})(c_{\mathsf{s}}+c_{\mathsf{m}})\right]}, \tag{4.1}$$

and the characteristic impedance

$$Z_{\mathsf{c}} = \frac{Z_{\mathsf{e}}}{2} = \frac{(z_{\mathsf{m}}^2 - z_{\mathsf{s}}^2)(c_{\mathsf{s}}^2 - c_{\mathsf{m}}^2) + \mathrm{i}2\omega\mu\epsilon(z_{\mathsf{s}}c_{\mathsf{s}} + z_{\mathsf{m}}c_{\mathsf{m}}) + (\omega\mu\epsilon)^2}{\mathrm{i}2\lambda_{\mathsf{e}}(c_{\mathsf{s}}+c_{\mathsf{m}})[(z_{\mathsf{s}}-z_{\mathsf{m}})(c_{\mathsf{s}}-c_{\mathsf{m}}) - \mathrm{i}\omega\mu\epsilon]}. \tag{4.2}$$

The line parameters c_{s}, c_{m}, z_{s}, and z_{m} have been derived in §2.3.3 and §2.3.4. In the inference examples described in §4.4.1, the geometric parameters of the cable cross-section will be assumed known, and the material parameters ϵ, σ, σ_{w}, and σ_{s} will be estimated from laboratory measurements. In order to explicitly exhibit the dependence of the model on the inferred parameters as well as on frequency, the expressions for the line parameters are rewritten as

$$c_{\mathsf{s}} = \tau_{\mathsf{s}}\epsilon, \tag{4.3}$$

$$c_{\mathsf{m}} = \tau_{\mathsf{m}}\epsilon, \tag{4.4}$$

$$z_{\mathsf{s}} = \eta_{\mathsf{s}}^{(\mathsf{w})}\sqrt{\frac{\omega}{\sigma_{\mathsf{w}}}} + \eta_{\mathsf{s}}^{(\mathsf{s})}\sqrt{\frac{\omega}{\sigma_{\mathsf{s}}}}, \tag{4.5}$$

$$z_{\mathsf{m}} = \eta_{\mathsf{m}}^{(\mathsf{w})}\sqrt{\frac{\omega}{\sigma_{\mathsf{w}}}} + \eta_{\mathsf{m}}^{(\mathsf{s})}\sqrt{\frac{\omega}{\sigma_{\mathsf{s}}}}, \tag{4.6}$$

where*

$$\begin{aligned}
\tau_{\mathsf{s}} &= \pi\left[\frac{1}{\ln(R_{\mathsf{e}}/r_{\mathsf{w}})}+\frac{1}{\ln(R_{\mathsf{o}}/r_{\mathsf{w}})}\right],\\
\tau_{\mathsf{m}} &= \pi\left[\frac{1}{\ln(R_{\mathsf{e}}/r_{\mathsf{w}})}-\frac{1}{\ln(R_{\mathsf{o}}/r_{\mathsf{w}})}\right],\\
\eta_{\mathsf{s}}^{(\mathsf{w})} &= \frac{1-\mathrm{i}}{2\pi r_{\mathsf{w}}}\sqrt{\frac{\mu_0}{2}}\left[1+\frac{(r_{\mathsf{ce}}-q)^2}{r_{\mathsf{w}}^2-(r_{\mathsf{ce}}-q)^2}+\frac{(r_{\mathsf{co}}-q)^2}{r_{\mathsf{w}}^2-(r_{\mathsf{co}}-q)^2}\right],\\
\eta_{\mathsf{s}}^{(\mathsf{s})} &= \frac{1-\mathrm{i}}{2\pi r_{\mathsf{i}}}\sqrt{\frac{\mu_0}{2}}\left(\frac{r_{\mathsf{i}}^4+r_{\mathsf{ce}}^4}{r_{\mathsf{i}}^4-r_{\mathsf{ce}}^4}+\frac{2r_{\mathsf{i}}^2r_{\mathsf{co}}^2}{r_{\mathsf{i}}^4-r_{\mathsf{co}}^4}\right),\\
\eta_{\mathsf{m}}^{(\mathsf{w})} &= \frac{1-\mathrm{i}}{2\pi r_{\mathsf{w}}}\sqrt{\frac{\mu_0}{2}}\left[\frac{(r_{\mathsf{ce}}-q)^2}{r_{\mathsf{w}}^2-(r_{\mathsf{ce}}-q)^2}-\frac{(r_{\mathsf{co}}-q)^2}{r_{\mathsf{w}}^2-(r_{\mathsf{co}}-q)^2}\right],\\
\eta_{\mathsf{m}}^{(\mathsf{s})} &= \frac{1-\mathrm{i}}{2\pi r_{\mathsf{i}}}\sqrt{\frac{\mu_0}{2}}\left(\frac{r_{\mathsf{i}}^4+r_{\mathsf{ce}}^4}{r_{\mathsf{i}}^4-r_{\mathsf{ce}}^4}-\frac{2r_{\mathsf{i}}^2r_{\mathsf{co}}^2}{r_{\mathsf{i}}^4-r_{\mathsf{co}}^4}\right).
\end{aligned}$$

It should be emphasized that, for a given cable geometry, these constants need be evaluated only once.

For a nominal cable segment of length Δz and a very small twist rate, the S-parameter matrix takes the form

$$\mathbf{S}^{(\mathsf{n})} = \begin{bmatrix} 0 & S_{21}^{(\mathsf{n})} \\ S_{21}^{(\mathsf{n})} & 0 \end{bmatrix},$$

where

$$S_{21}^{(\mathsf{n})} = \mathrm{e}^{\mathrm{i}\lambda_{\mathsf{c}}\Delta z}. \tag{4.7}$$

4.2.2 A simple chafe fault model

Deferring a detailed electromagnetic model of scattering from a hole to a later publication, the approach taken in [78] for coaxial cable will be followed towards developing a simple fault model. Consider, then, a small chafe located at a distance d_{f} on a STP cable of length ℓ, having width $w_{\mathsf{f}} = r_{\mathsf{i}}\Delta\phi_{\mathsf{f}}$, length ℓ_{f}, and angular position ϕ_{f}, as depicted in Figure 4.1. It is assumed firstly that common-mode propagation across the chafed cable segment may be modeled by a modified axial eigenvalue λ_{f} and a modified characteristic impedance Z_{f}, as indicated in the figure, and that the inevitable coupling of energy into the differential mode will be negligibly small. It is further assumed that these fault model parameters may be obtained from the general expressions (4.1) and (4.2) by recomputing the line parameters therein for the chafed cable

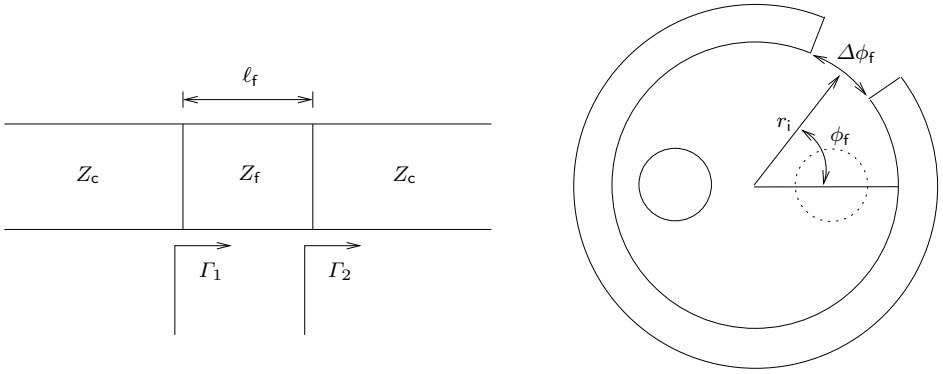

Figure 4.1: (Left) A constant-impedance model for a chafed cable segment. (Right) Cross-section of a cable with a chafed shield.

*Note that high-frequency approximations are being used here for the line impedances, in anticipation of the frequency range of laboratory measurements reported subsequently.

cross-section. Specifically, since the (electrical) length of the chafe is very small, the effects of loss due to finite conductivity may be neglected by setting $\sigma = z_{\mathsf{s}} = z_{\mathsf{m}} = 0$. Replacing the (per-unit-length) even-mode capacitance $c_{\mathsf{s}} + c_{\mathsf{m}}$ with the (per-unit-length) common-mode fault capacitance $c_{\mathsf{f}} \equiv \tau_{\mathsf{f}}\epsilon$, one thus obtains the expressions

$$\lambda_{\mathsf{f}} = \omega\sqrt{\mu\epsilon[1 + (\kappa r_{\mathsf{ce}})^2]}, \tag{4.8}$$

$$Z_{\mathsf{f}} = \frac{1}{2\tau_{\mathsf{f}}}\sqrt{\frac{\mu}{\epsilon}}. \tag{4.9}$$

Unfortunately, τ_{f} appearing above cannot be obtained in closed form, and a look-up table must instead be constructed off-line. Toward this end, we choose a set of angular fault positions within the range $(0, \pi/2)$ and a set of fault widths within the range $(0, \pi r_{\mathsf{i}})$. For each possible combination of ϕ_{f} and w_{f}, the 2D Laplace equation ($\nabla_\perp^2 \Phi = 0$) is solved under even-mode boundary conditions (*i.e.*, both inner conductors set to unit potential while the shield is held at zero potential). Since the cable cross-section is now "open," the computational domain must be bounded by an outer surface held at zero potential that is sufficiently removed from the shield in order not to disturb the fields leaking out through the hole. The resulting potential is then integrated numerically to obtain

$$\tau_{\mathsf{f}}(\phi_{\mathsf{f}}, w_{\mathsf{f}}) = -\frac{1}{2}\left[\oint_{\mathcal{W}_1} \hat{\mathbf{n}}_1 \cdot \boldsymbol{\nabla}_\perp \Phi(\mathbf{r}_\perp)\,\mathrm{d}l + \oint_{\mathcal{W}_2} \hat{\mathbf{n}}_2 \cdot \boldsymbol{\nabla}_\perp \Phi(\mathbf{r}_\perp)\,\mathrm{d}l\right], \tag{4.10}$$

where the dependence of τ_{f} on the underlying fault parameters ϕ_{f} and w_{f} has been indicated explicitly, and the average of separate integrals around each conductor is taken in an effort to compensate somewhat for the asymmetry of the cable cross-section due to the presence of the hole.[†]

Since the chafe model is symmetric with respect to the cable axis, the S matrix for the fault with respect to the common-mode impedance Z_{c} takes the form

$$\mathbf{S}^{(\mathsf{f})} = \begin{bmatrix} S_{11}^{(\mathsf{f})} & S_{21}^{(\mathsf{f})} \\ S_{21}^{(\mathsf{f})} & S_{11}^{(\mathsf{f})} \end{bmatrix}.$$

Noting from Fig. 4.1 that $\Gamma_1 = -\Gamma_2$, one obtains

$$S_{11}^{(\mathsf{f})} = \frac{\Gamma_2(\mathrm{e}^{\mathrm{i}2\lambda_{\mathsf{f}}\ell_{\mathsf{f}}} - 1)}{1 - \Gamma_2^2\,\mathrm{e}^{\mathrm{i}2\lambda_{\mathsf{f}}\ell_{\mathsf{f}}}}, \tag{4.11}$$

$$S_{21}^{(\mathsf{f})} = \frac{(1 - \Gamma_2^2)\,\mathrm{e}^{\mathrm{i}\lambda_{\mathsf{f}}\ell_{\mathsf{f}}}}{1 - \Gamma_2^2\,\mathrm{e}^{\mathrm{i}2\lambda_{\mathsf{f}}\ell_{\mathsf{f}}}}, \tag{4.12}$$

where

$$\Gamma_2 = \frac{Z_{\mathsf{c}} - Z_{\mathsf{f}}}{Z_{\mathsf{c}} + Z_{\mathsf{f}}}. \tag{4.13}$$

Finally, the composite S-parameter matrix for a chafed cable may be written using the S-parameter matrices derived above for nominal and faulty cable segments, with a switch to and from the corresponding T-parameter matrices. The result is

$$\mathbf{S} = \begin{bmatrix} S_{11}^{(\mathsf{f})}\,\mathrm{e}^{\mathrm{i}2\lambda_{\mathsf{c}}d_{\mathsf{f}}} & S_{21}^{(\mathsf{f})}\,\mathrm{e}^{\mathrm{i}\lambda_{\mathsf{c}}(\ell-\ell_{\mathsf{f}})} \\ S_{21}^{(\mathsf{f})}\,\mathrm{e}^{\mathrm{i}\lambda_{\mathsf{c}}(\ell-\ell_{\mathsf{f}})} & S_{11}^{(\mathsf{f})}\,\mathrm{e}^{\mathrm{i}2\lambda_{\mathsf{c}}(\ell-\ell_{\mathsf{f}}-d_{\mathsf{f}})} \end{bmatrix}. \tag{4.14}$$

4.2.3 System S-parameters

The S-parameter framework detailed in [78] is now applied to obtain the overall system model for the vector network analyzer (VNA) based measurement setup shown in Fig. 4.2. Our ultimate goal here is to validate the fault model of §4.2.2; therefore, the two inner conductors of the STP cable are assumed shorted together

[†]Alternatively, τ_{f} may be computed as a *single* integral around a contour $\mathcal{C}$ that encloses both conductors.

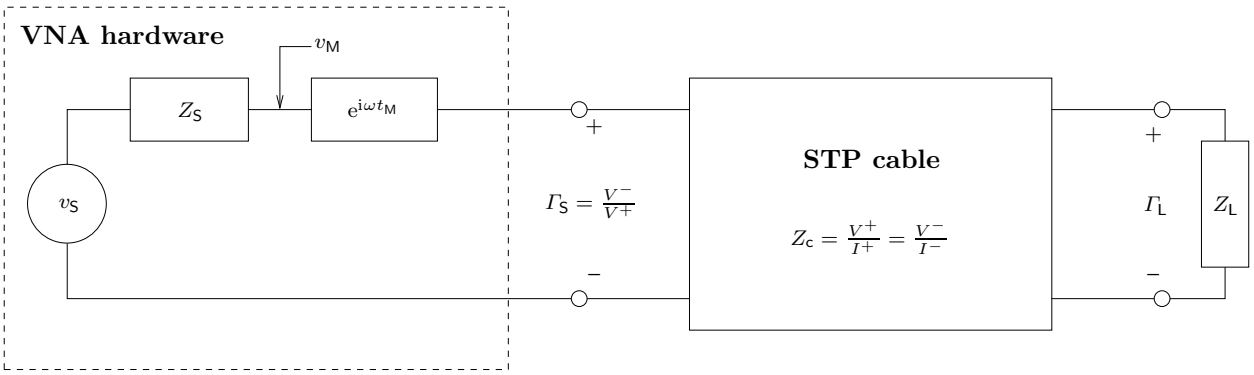

Figure 4.2: VNA hardware model.

at the ends in an effort to preferentially excite the common mode. The input signal is the source voltage v_{S}, presented with a port impedance Z_{S}. The load impedance Z_{L} represents an arbitrary, possibly frequency-dependent, load connection, including the possibility of connecting the other end of the cable back into the VNA, in which case $Z_{\mathsf{L}} = Z_{\mathsf{S}}$. The output signal is the voltage v_{M} indicated in the figure, which differs from the actual voltage at that point by an internal measurement delay t_{M} and a calibration gain G.

For modeling purposes, the VNA hardware measurement setup shown in Fig. 4.2 may be represented by the abstract S-parameter block shown in Fig. 4.3, with $\mathbf{S}$ given by (4.14). The general S-parameters for the composite system, including impedance mismatches, measurement delay, and gain, are given by [78]

$$\overline{\mathbf{S}} = \frac{G\,\mathrm{e}^{\mathrm{i}\omega t_{\mathsf{M}}}}{1 + S_{11}\Gamma_{\mathsf{S}} - S_{22}\Gamma_{\mathsf{L}} - (S_{11}S_{22} - S_{12}S_{21})\Gamma_{\mathsf{S}}\Gamma_{\mathsf{L}}} \times \begin{bmatrix} S_{11} + \Gamma_{\mathsf{S}} - \Gamma_{\mathsf{S}}\Gamma_{\mathsf{L}}S_{22} - (S_{11}S_{22} - S_{12}S_{21})\Gamma_{\mathsf{L}} & S_{12}(1-\Gamma_{\mathsf{S}})(1-\Gamma_{\mathsf{L}}) \\ S_{21}(1+\Gamma_{\mathsf{S}})(1+\Gamma_{\mathsf{L}}) & S_{22} - \Gamma_{\mathsf{L}} - \Gamma_{\mathsf{S}}\Gamma_{\mathsf{L}}S_{11} + (S_{11}S_{22} - S_{12}S_{21})\Gamma_{\mathsf{S}} \end{bmatrix}, \quad (4.15)$$

where S_{mn} are the elements of the common-mode S-matrix given in (4.14) for the possibly chafed cable.

The elements of the matrix $\overline{\mathbf{S}}$ may be measured directly by a VNA; equations (4.1) through (4.15) relate these measurements to the underlying cable and fault parameters that one may wish to infer from laboratory data. With only a look-up table for τ_{f} computed ahead of time, these closed-form equations allow one to compute the system S-parameters within $\sim 20\ \mu$s per measurement frequency ω_m in MATLAB$^{\mathrm{TM}}$ on a modern desktop PC.

4.3 Bayesian parameter inference

For the validation of the theoretical model against experimental measurements, one must adopt a method for estimating the effective parameters of the particular cable under test, as well as those of the measurement

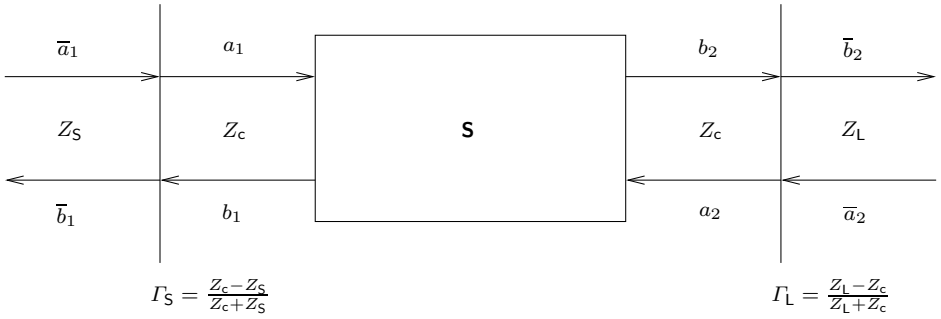

Figure 4.3: S-parameter block diagram of the measurement setup with impedance mismatch.

environment. In this section, a specific probabilistic framework is presented for inferring the unknown or uncertain parameters θ of the cable and the experimental setup from S-parameter measurements at M discrete frequencies. In the most general case of all four system S-parameters simultaneously available, the noisy measurement model takes the form

$$y = g(\theta, \omega) + \nu, \tag{4.16}$$

where $\omega \in \mathrm{R}^M$ is the vector of measurement frequencies, $y \in \mathrm{C}^{4M}$ is the vector of S-parameter measurements, $\nu \in \mathrm{C}^{4M}$ is a complex vector of additive random noise, and $g \in \mathrm{C}^{4M}$ is a nonlinear function of θ whose form has been elucidated in §4.2. The explicit ω dependence on g will henceforth be dropped, but is implied throughout.

Assuming statistically independent, identically distributed Gaussian noise for both the real and the imaginary parts of the measurements, the likelihood distribution for the measured data may then be written as[‡]

$$p(y|\theta, s) = (2\pi s^2)^{-4M}\, \mathrm{e}^{-\|y-g(\theta)\|^2/2s^2}, \tag{4.17}$$

where the variance s^2 characterizes the uncertainty due to *both* modeling error and measurement noise.

It is reasonable to assume that one would have access to manufacturer's specifications, baseline or calibration data, *etc.*, from which one can gain some prior knowledge of the cable and experimental setup parameters. Let this knowledge be represented in the form of a joint prior distribution $p(\theta)$ over the parameters to be estimated. Additionally, the combined standard deviation s of modeling error and measurement noise is treated as initially unknown, and assumed to follow an exponential distribution $p(s) = (1/\bar{s})\, \mathrm{e}^{-s/\bar{s}}$, for $s \geq 0$, with mean $\bar{s} = 0.1$. The net prior distribution is then $p(\theta, s) = p(\theta)\, (1/\bar{s})\, \mathrm{e}^{-s/\bar{s}}$.

Ultimately, our interest lies in estimating the parameter values given the measured data. This is achieved first by specifying the posterior probability density function through Bayes' theorem,

$$p(\theta, s|y) = \frac{p(y|\theta, s)\, p(\theta, s)}{\int p(y|\theta', s')\, p(\theta', s')\, \mathrm{d}\theta'\, \mathrm{d}s'}, \tag{4.18}$$

and then finding the maximum-posterior estimate (θ^*, s^*) by solving the optimization problem

$$\text{maximize } p(\theta, s|y). \tag{4.19}$$

Furthermore, the shape of the marginal posterior distribution

$$p(\theta|y) = \int p(\theta, s|y)\, \mathrm{d}s \tag{4.20}$$

around θ^* indicates how confident we are in this estimate.

Unfortunately, finding an analytical solution to problem (4.19), or for that matter the marginal integral (4.20), is intractable. However, Markov-chain Monte Carlo (MCMC) methods enable one to draw N samples from the posterior distribution,

$$\theta_n, s_n \sim p(\theta, s|y), \quad n = 1, 2, \ldots, N, \tag{4.21}$$

with only the ability to evaluate the numerator in (4.18). This set of N samples then enables the estimation of the desired quantities. In particular,

$$(\theta^*, s^*) \simeq \mathrm{argmax}_{\theta_n, s_n}\, p(y|\theta_n, s_n)\, p(\theta_n, s_n). \tag{4.22}$$

Furthermore, by themselves, the θ_n samples are distributed according to the marginal posterior $p(\theta|y)$, and thus their spread may be taken as a measure of our uncertainty about this estimate. More generally, the law of large numbers guarantees that

$$\lim_{N\to\infty} \frac{1}{N} \sum_{n=1}^{N} f(\theta_n) = \int f(\theta)\, p(\theta|y)\, \mathrm{d}\theta = \mathrm{E}[f(\theta)]. \tag{4.23}$$

Thus, the samples can be used to estimate the expected value of almost any function of θ. Standard examples are the mean $f(\theta) = \theta$ and the variance $f(\theta) = (\theta - \mathrm{E}[\theta])^2$. In addition, for skewed distributions with separate

[‡]Since y is a $4M$-dimensional complex-valued vector, this is the joint distribution of $8M$ real-valued random variables.

mean and mode, it is useful to represent the single-variate marginal uncertainty as a $100(1-\alpha)\%$ *posterior interval*. This is defined as the interval $[a, b]$ such that $100(\alpha/2)\%$ of the samples fall below a and above b [79, p. 38].

There are many different MCMC-based algorithms one can implement to achieve the above sampling. The results presented in §4.4 were obtained using a relatively new method called *nested sampling* [80, 81].

4.4 Experimental results

The modeling and Bayesian inference process outlined above is now demonstrated by a few examples using a 1-m long section of impedance-controlled aircraft-grade STP cable, whose geometric specifications are provided in Table 2.1, with SMA connectors attached to each end, and with the inner conductors shorted together at the source and the load ends in order to enable excitation of primarily the common mode. The S-parameter measurements were made using a Rhode & Schwarz ZVB8 VNA (300 kHz – 8 GHz, 4 ports). For all examples, the VNA was calibrated using a lower-grade kit (50 Ω, ZV-Z132, male), and unless noted otherwise, the S-parameters were measured from 2 MHz to 8 GHz, in increments of 2 MHz, with an IF-bandwidth (or measurement bandwidth) setting of 1 kHz and 0 dBm input power.

The results presented below demonstrate that the twist-corrected analytical model can fit experimental data within 2 % maximum error out to 1 GHz. Beyond this frequency, the (unmodeled) effects due to the connectors as well as cable imperfections start to dominate the data. This is a useful practical result, since most field-deployable instrumentation would operate within this frequency range for a variety of other reasons. We note in passing that the frequency-domain measurements reported here may also be used to synthesize the time-domain reflectometry (TDR) and time-domain transmissometry (TDT) responses of the cable, as we will show subsequently.

4.4.1 Nominal cable examples

Due to a variety of reasons including manufacturing variability in cable construction and calibration drifts of measurement equipment, it is advisable to infer the actual parameters of a given cable and experimental setup directly from laboratory measurements. Table 4.1 lists the prior information available for these experiments; the notation $\mathcal{N}^+$ denotes the nonnegative Gaussian distribution. The joint prior distribution $p(\theta)$ of the vector of parameters to be inferred is given by the product of the marginal prior distributions indicated in the table.

Table 4.1: Parameter prior information.

Parameter	**Distribution**	**Description**
ε_{d}	$\mathcal{N}^+(2.30, 2.0)$	effective relative dielectric permittivity
σ_{w}	$\mathcal{N}^+(6, 0.2) \times 10^7$ S/m	wire conductivity
σ_{s}	$\mathcal{N}^+(0.5, 2) \times 10^7$ S/m	shield conductivity
σ_{d}	$\mathcal{N}^+(2, 2) \times 10^{-15}$ S/m	effective dielectric conductivity
ℓ	$\mathcal{N}^+(1, 0.005)$ m	cable length
Z_{S}	$\mathcal{N}^+(50, 2)$ Ω	source impedance
t_{M}	$\mathcal{N}^+(0.1, 0.05)$ ns	measurement time delay
G	$\delta(G-1)$	system gain (assumed fixed)

Note that, in place of ϵ and σ used in §4.2.1, two *effective* parameters ε_{d} and σ_{d} are being introduced here to account for the inhomogeneous nature of the dielectric medium between the wires and the shield of a real impedance-controlled cable.[§] If conductors 1 and 2 in Fig. 2.1 are assumed to be coated with insulation

[§]Since air and foam are nonmagnetic, the dielectric permeability remains μ_0.

of permittivity $\epsilon = 2.3\,\epsilon_0$ and radius q (such that they are just touching each other and the shield), and the remaining space inside the shield assumed filled with air, a rough estimate for the effective *relative* dielectric permittivity would be

$$\varepsilon_{\mathsf{d}} \simeq 1.57877. \tag{4.24}$$

Example 1

We start by considering a simple field-deployable measurement setup where the input of the cable is attached to the VNA, and the other end of the cable is left open-ended in air. This is a more practical interrogation setup because it does not require attaching both ends of the cable to the VNA, or any specialized termination at the other end of the cable. (Generally, there are no impedance standards for aircraft connectors.) Furthermore, this measurement setup is the frequency-domain equivalent of the traditional TDR setup commonly used in practice. In this example, the VNA measures the system $\overline{S}_{11}$ parameter, which includes the signal reflected from the open far end of the cable, and thus provides more information regarding the unknown cable parameters than would be the case for a matched termination. Accordingly, the VNA measurements are modeled by $\overline{S}_{11}$ with $\Gamma_{\mathsf{L}} = 1$ in (4.15).

Table 4.2 shows the results of the model parameter inference for this example. The estimates and uncertainty information were computed from the approximate mode and 95 % posterior interval of 2,000 samples from the posterior distribution, all obtained using the nested sampling algorithm mentioned in §4.3. A cross-section of the samples, corresponding to the marginal posterior distribution $p(\varepsilon_{\mathsf{d}}, \sigma_{\mathsf{w}}|y)$, is plotted in Fig. 4.4. Perhaps most notable is the inference of the effective relative dielectric permittivity ε_{d}. The prior for this parameter corresponds to a homogeneous insulation of relative permittivity 2.3 (see Table 4.1), but the probabilistic inference algorithm was able to glean from data a more realistic value closer to the crude estimate given in (4.24).

In Fig. 4.5, the measured data are plotted against the best (*i.e.*, most probable) fitting model for the system $\overline{S}_{11}$ parameter. While only the VNA measurements out to 1 GHz were used to obtain the fit, the comparison between the measurements and model extrapolated out to 2 GHz is also shown. We also explored fitting all the data out to 2 GHz, and that resulted in increased error for the frequencies below 1 GHz. Under the controlled laboratory test conditions, it appears the residual error between the best fitting model and the measured data is more deterministic than random. This is caused by a variety of factors not considered in the model, such as frequency-dependent VNA miscalibration and geometry variation along the length of the cable. Furthermore, this error was treated as random noise in the probability model as an effective way to handle its presence. While the random noise component may be small in the lab, we do not expect this to hold in any practical environment. The modeling and parameter inference approach we have taken is expected to be robust under both types of uncertainty likely to be encountered in the field.

Table 4.2: Example 1. Parameter estimates and 95 % posterior intervals.

Parameter	**Mode**	**95% Interval**	**Units**
ε_{d}	1.5824	$[1.560, 1.603]$	
σ_{w}	6.0232	$[5.648, 6.369]$	10^7 S/m
σ_{s}	0.4974	$[0.479, 0.520]$	10^7 S/m
σ_{d}	2.000	$[0.156, 5.699]$	10^{-15} S/m
Z_{S}	50.8202	$[50.48, 51.18]$	Ω
ℓ	0.9997	$[0.993, 1.007]$	m
t_{M}	0.0776	$[0.077, 0.078]$	ns
s	0.0063	$[0.006, 0.007]$	

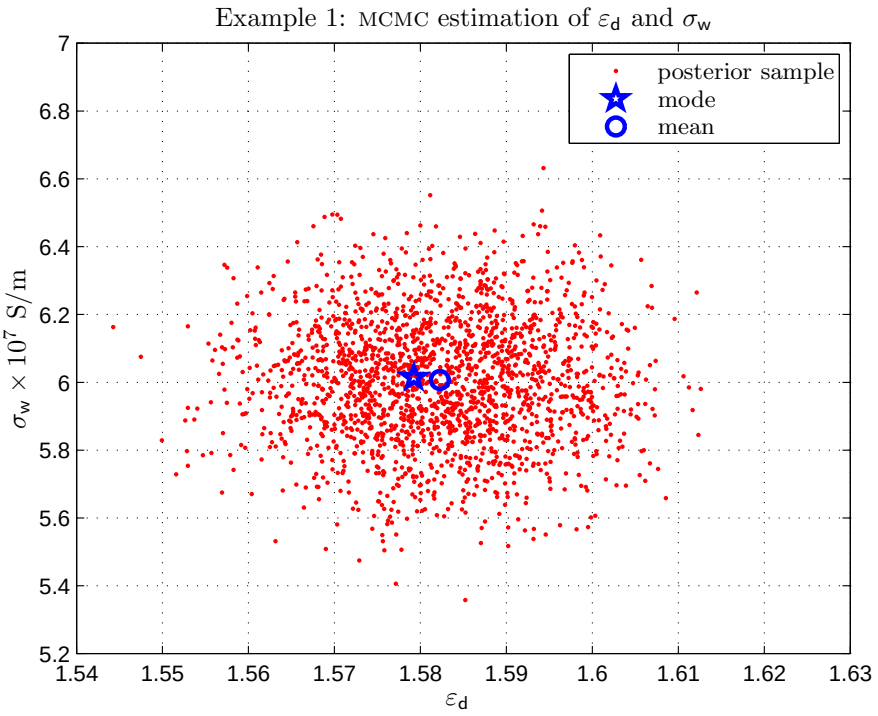

Figure 4.4: Samples from the marginal posterior distribution $p(\varepsilon_d, \sigma_w|y)$, which show the uncertainty associated with the simultaneous estimation of these parameters given the measured data.

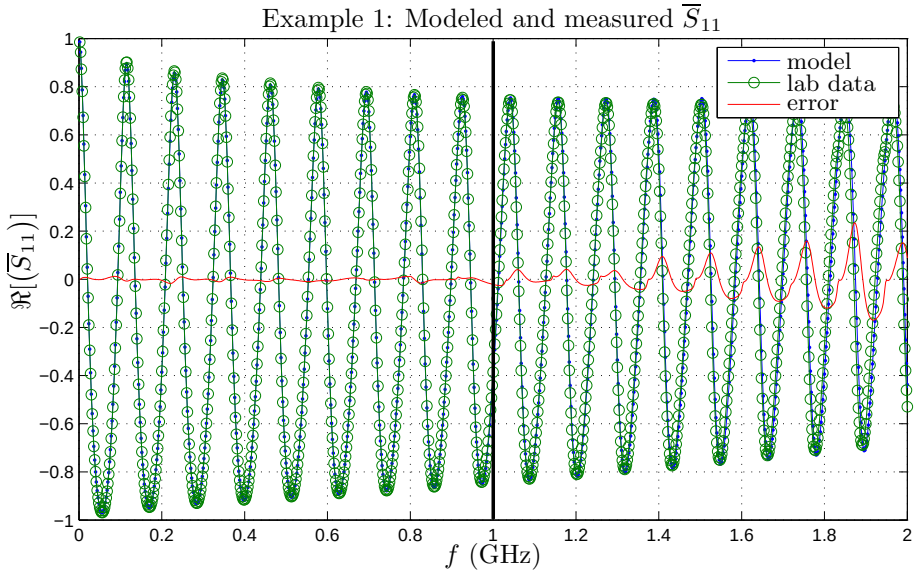

Figure 4.5: Comparison between the measured and modeled $\Re[(\overline{S}_{11})]$ (the plot for the imaginary part looks similar). Only the data out to 1 GHz were used in the inference process to obtain the fit, below this frequency, the maximum absolute error is less than 0.0213. The data beyond 1 GHz are provided to show the onset of unmodeled effects above this frequency.

Example 2

The more ideal case is now considered where measurements of the system $\overline{S}_{11}$ and $\overline{S}_{21}$ parameters are available simultaneously. This will tell us how much improvement we can expect over the non-ideal measurement setup discussed in Example 1. In addition, the additional $\overline{S}_{21}$ data will provide practical information regarding signal transmission through the cable, which is important for fault detection.

The same table and set of figures shown for example 1 are produced for this example (also based on $2,000$ samples from the posterior distribution). Table 4.3 and Figure 4.6 show that the estimated parameters and the associated accuracy were largely unchanged. This makes sense from an energy/information conservation perspective. In the first example, all the energy was reflected by the open end and measured at the input port. In this example, most of the signal energy is transmitted into the output port 2, and is measured as $\overline{S}_{21}$, while the rest is reflected back to the input port 1 and is measured as $\overline{S}_{11}$. This example further shows that more measurements—there are twice as many measurement points in example 2—do not necessarily translate to greater accuracy, a fact captured by our Bayesian inference approach.

The most striking difference between the two examples occurs with respect to how well the model fits the measured data, shown in Figs. 4.7 and 4.8. The maximum absolute error over all measurements for both $\overline{S}_{11}$ and $\overline{S}_{21}$ was 0.018, and when the model is extrapolated beyond 1 GHz, the residual error grows much less rapidly with frequency. This might be expected because the cable is now properly terminated into the calibrated port 2 of the VNA, which was not the case in example 1. Another interesting difference is that the estimated port impedance parameter Z_{S} differs from the estimate obtained for the first example by a statistically significant margin. This could be caused by a variety of reasons such as the non-ideal termination used for the first example or a possible drift in the calibrated impedance between the two sets of tests.

Finally, Fig. 4.9 summarizes the practical results for the modeling work by showing the attenuation of a propagating mode as a function of frequency corresponding to the best model parameter fit given the measured data. The solid blue curve shows the attenuation constant $\alpha(\omega) = \Im[\lambda_{\mathsf{c}}(\omega)]$ for the model best matching the measured data out to 1 GHz; this is the attenuation one can expect for the given cable under perfectly matched conditions. The dashed red curve in the figure is the theoretical $-\ln|\overline{S}_{21}|/\ell$ (which is directly comparable to α), calculated by fitting the model to $\overline{S}_{21}$ data measured out to 8 GHz in the lab, the latter plotted as the solid green curve. Since the S-parameter model and data include a significant impedance mismatch between the source and the cable, higher attenuation is observed in an oscillatory fashion for frequencies greater than about 10 MHz, as expected in accordance with Fig. 3.6. The broad spectral feature peaking around 4 GHz in the lab data is believed to be a connector artifact; not surprisingly, the model does not fit this feature.

Table 4.3: Example 2. Parameter estimates ± one standard deviation

Parameter	**Mode**	95 % **Interval**	**Units**
ε_{d}	1.5443	$[1.521, 1.566]$	
σ_{w}	6.0201	$[5.634, 6.374]$	10^7 S/m
σ_{s}	0.5003	$[0.480, 0.526]$	10^7 S/m
σ_{d}	2.000	$[0.169, 5.742]$	10^{-15} S/m
Z_{S}	51.5423	$[51.19, 51.93]$	Ω
ℓ	0.9995	$[0.993, 1.007]$	m
t_{M}	0.0785	$[0.078, 0.079]$	ns
s	0.0047	$[0.004, 0.005]$	

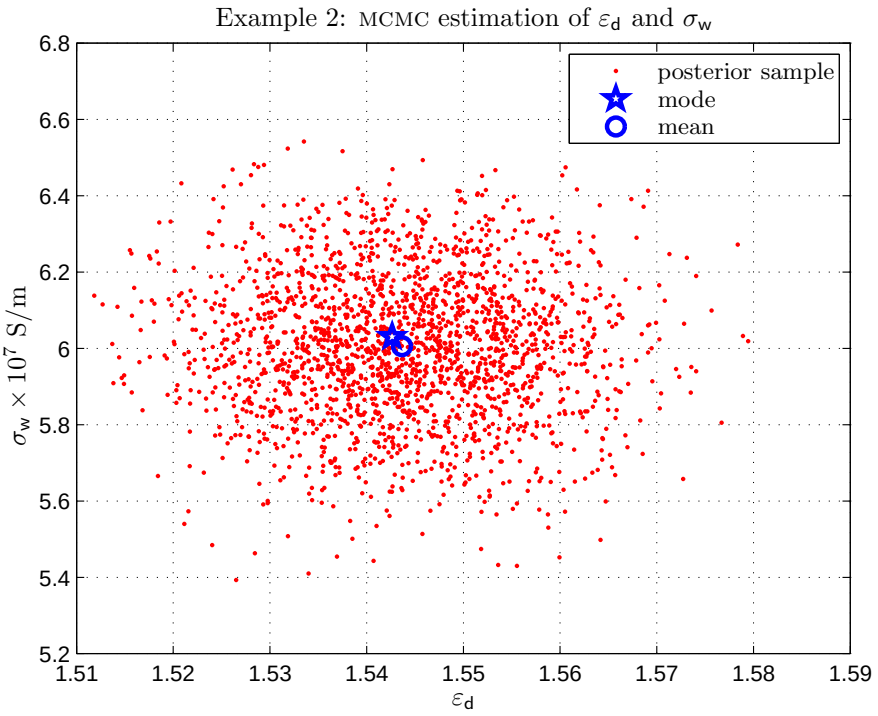

Figure 4.6: Samples from the marginal posterior distribution $p(\varepsilon_d, \sigma_w|y)$, which show the uncertainty associated with the simultaneous estimation of these parameters given the measured data.

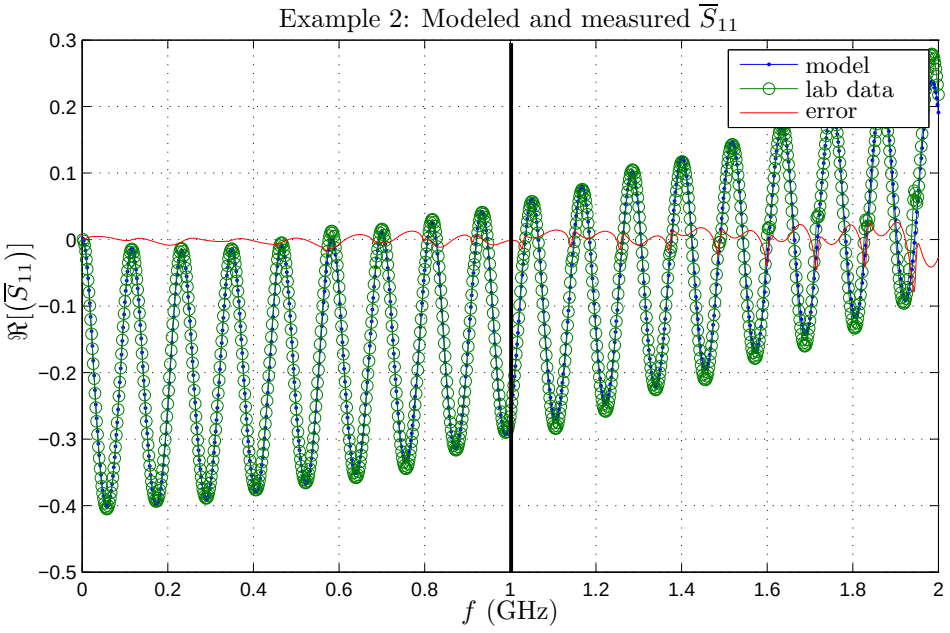

Figure 4.7: Comparison between the measured and modeled $\Re[(\overline{S}_{11})]$ (the plot for the imaginary part looks similar). Only the data out to 1 GHz were used in the inference process to obtain the fit.

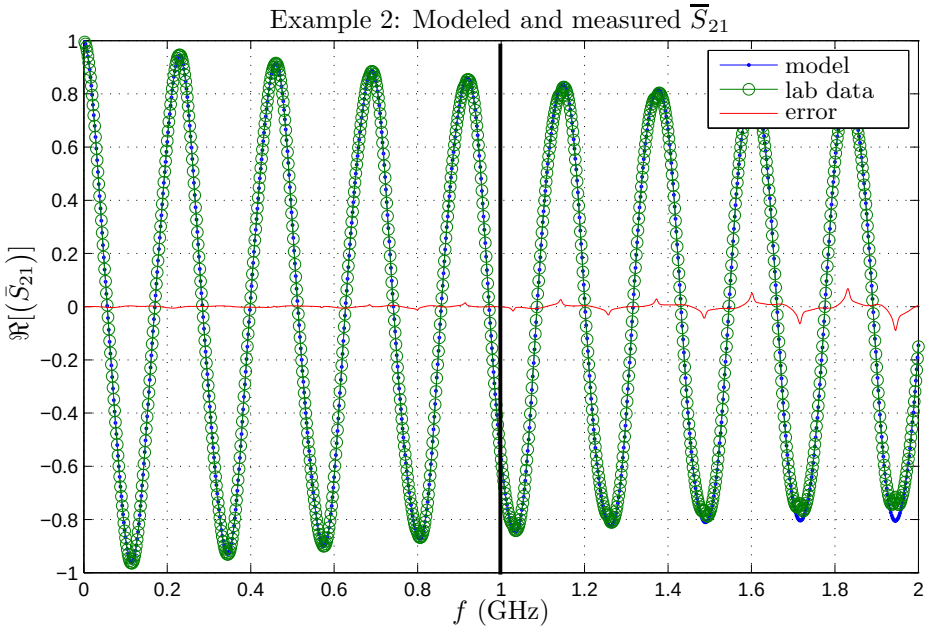

Figure 4.8: Comparison between the measured and modeled real part of $\overline{S}_{21}$ (the plot for the imaginary part looks similar). Only the data out to 1 GHz were used in the inference process to obtain the fit.

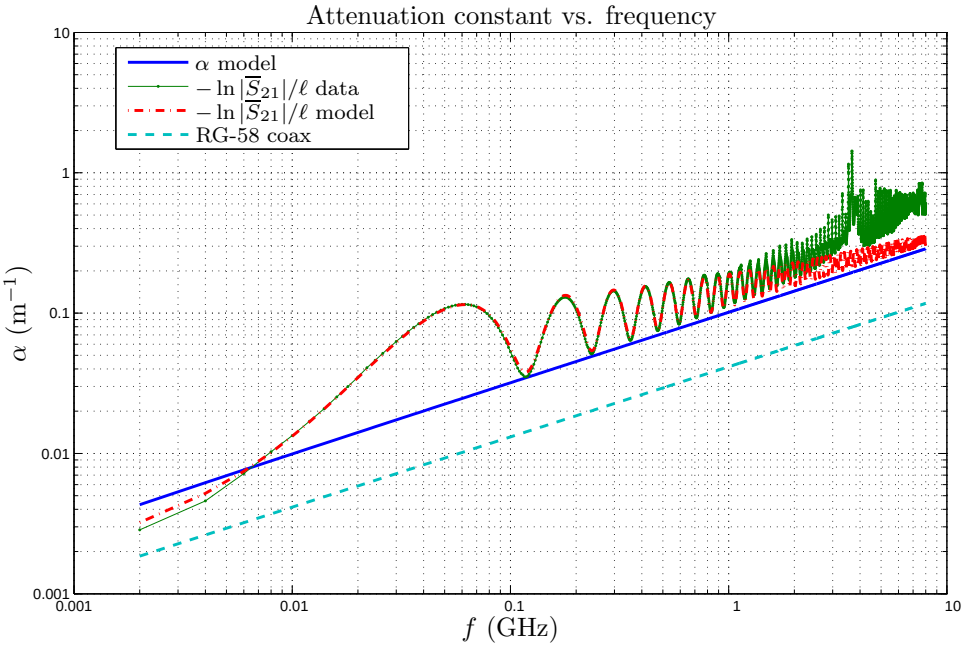

Figure 4.9: Comparison of modeled and measured attenuation constants for STP cable (see the text). The cyan curve is the attenuation constant of theoretical RG-58 coaxial cable, provided for comparison.

4.4.2 Faulty cable example

In this example, a 3 mm × 6 mm fault centered at 60° was added to the cable at 0.33 m (*i.e.*, $w_\mathsf{f} = 3$ mm, $\ell_\mathsf{f} = 6$ mm, $\phi_\mathsf{f} = \pi/3$, and $d_\mathsf{f} = 0.33$ m), which was then interrogated with the same measurement setup as in §4.4.1. The nominal cable parameters are assumed to have the values estimated in the previous section, and the goal is to validate the chafe model against laboratory data.

In Fig. 4.10, the difference between the nominal and the chafed cable is plotted in the frequency domain, where we again focus on the real parts of $\overline{S}_{11}$ and $\overline{S}_{21}$. The plot clearly shows increasing fault detectability with frequency, especially with respect to the $\overline{S}_{11}$ parameter, which is roughly equivalent to the TDR response of the chafed cable. Since the twist-corrected cable model matches the lab results out to about 1 GHz, and the chafe produces little measurable effect below 200 MHz, it is concluded that 200 MHz – 1 GHz is the most useful range of frequencies for model-based inference of unknown cable or fault parameters from experimental data.

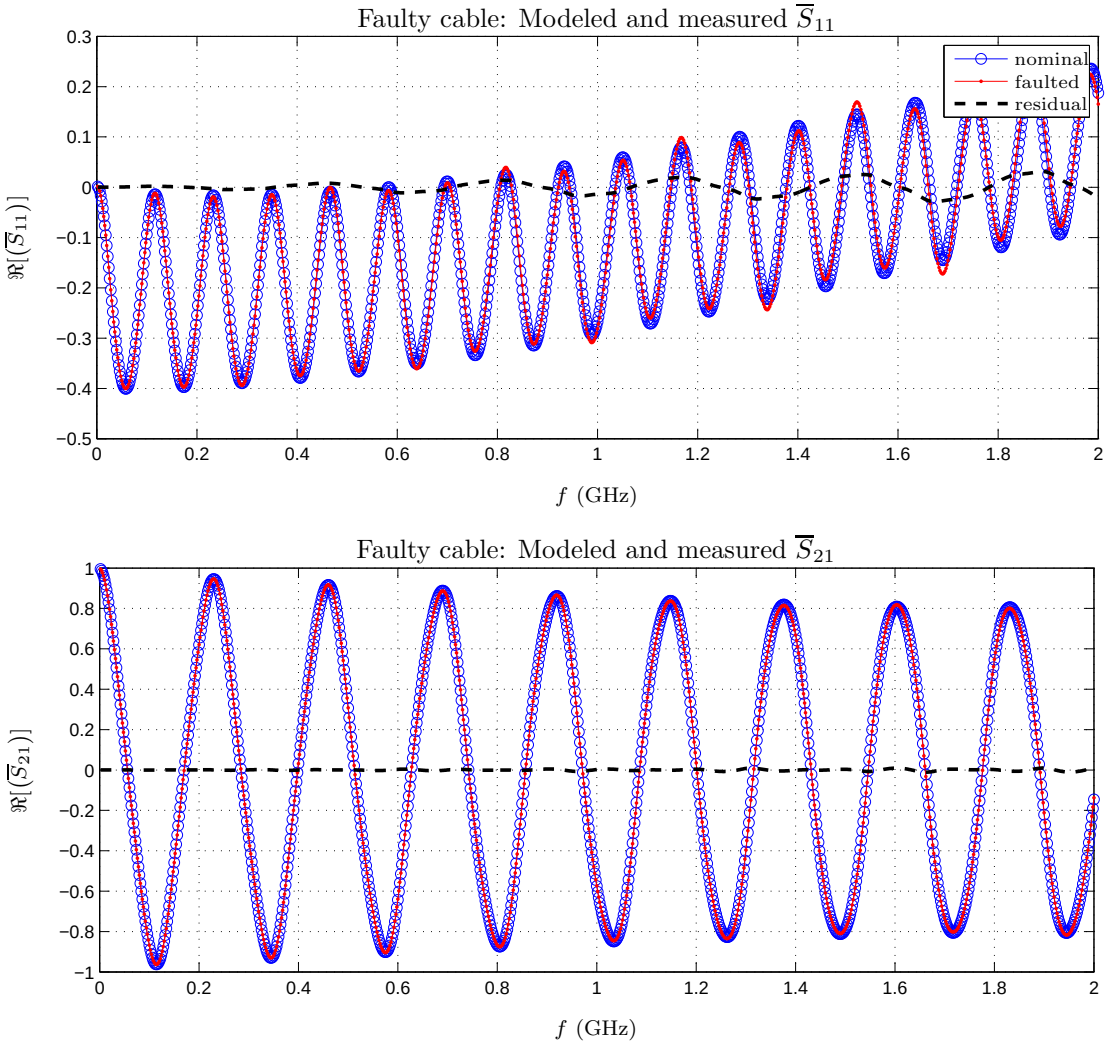

Figure 4.10: Frequency-domain comparison between nominal and chafed cable models.

In order to aid intuition, the time-domain transmitted and reflected responses to the input signal shown in Fig. 4.11 are synthesized and plotted in Fig. 4.12.

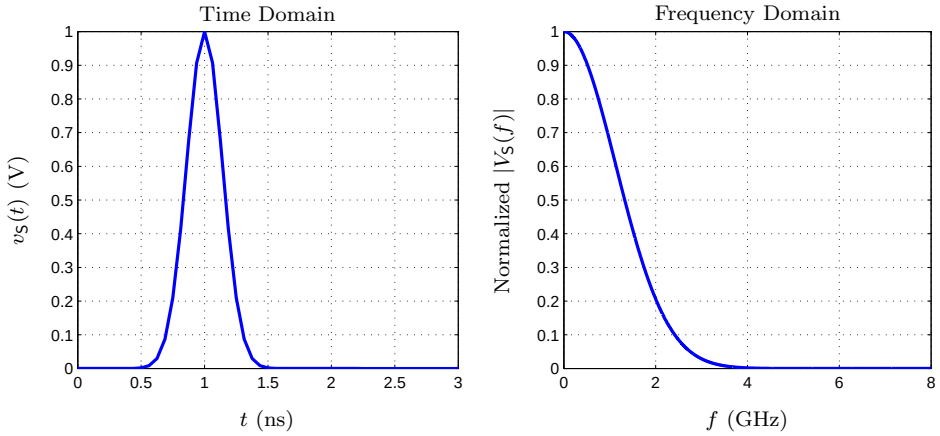

Figure 4.11: Input interrogation signal used for the time-domain analysis.

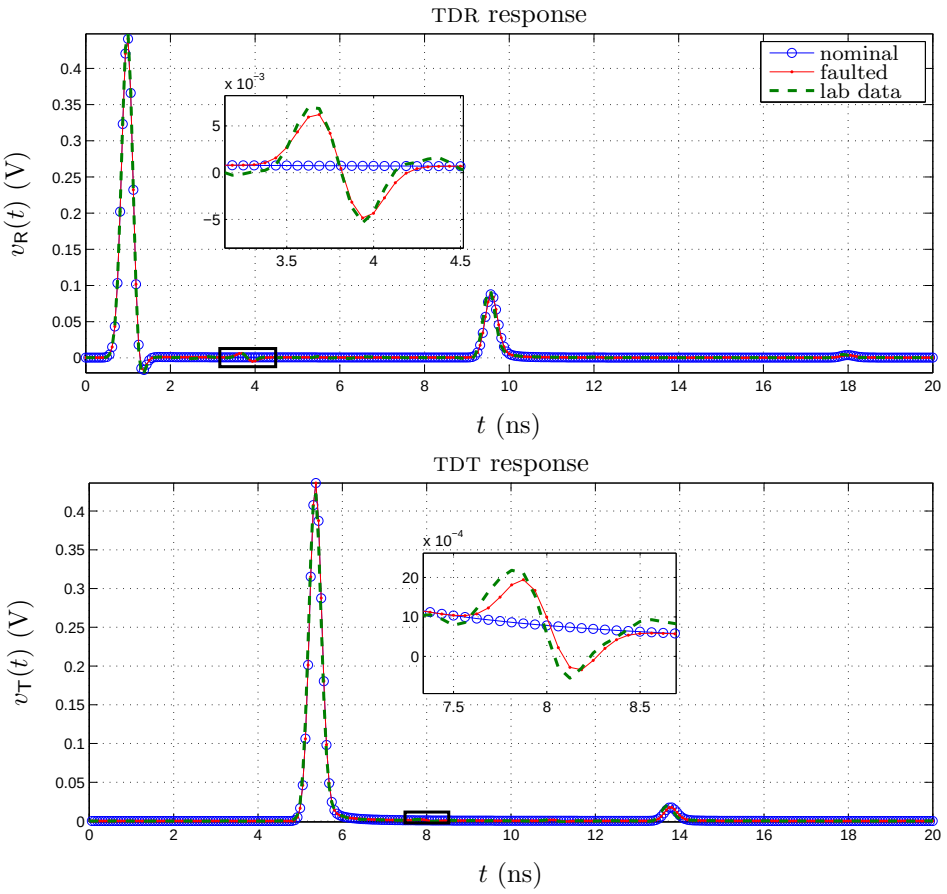

Figure 4.12: Time-domain comparison between nominal and chafed models with lab measurements from a chafed STP cable. The plots show the net measured voltage response to the input pulse shown above in Fig. 4.11.

Specifically, the applied input source voltage was

$$v_{\mathsf{S}}(t) \,=\, \exp\left[-\left(\frac{t-1\,\mathrm{ns}}{0.2\,\mathrm{ns}}\right)^2\right], \tag{4.25}$$

$$V_{\mathsf{S}}(f) \,=\, \mathtt{fft}[v_{\mathsf{S}}(t)], \tag{4.26}$$

where $t = m\,\Delta t$, for $m = 0, 1, \ldots, M-1$, with $M = 8001$ and $\Delta t = 1/(2M \times 10^6)$. The *net* reflected and transmitted signals are then synthesized, from both modeled and measured data, according to the equations

$$v_{\mathsf{R}}(t) \,=\, \mathtt{ifft}\left[\frac{1}{2}(1+\bar{S}_{11})V_{\mathsf{S}}\right], \tag{4.27}$$

$$v_{\mathsf{T}}(t) \,=\, \mathtt{ifft}\left[\frac{1}{2}\bar{S}_{21}V_{\mathsf{S}}\right]. \tag{4.28}$$

These equations follow directly from the definition of $\overline{S}_{mn}$, as described in [78]. The time-domain plots show the contribution from the chafe to be roughly the derivative of the input signal (as expected) and quite small at ~ 5 mV for the TDR response, and ~ 1 mV for the TDT response.

Chapter 5

Conclusion

5.1 Summary of main results

From a modeling perspective, perhaps the most important point to stress is that the filament model is more than capable of reproducing the eigenvalues and the mode fields of both SUP and STP cables with sufficiently high accuracy for the purpose of fault detection. In fact, none of the other approaches that were attempted proved amenable to analytical treatment to nearly the same extent as the filament model. Some of the more esoteric features that are characteristic of helical and other periodic structures—significant difference in the frequency dependence of common- and differential-mode eigenvalues, presence of "extraordinary" bands (referred to as stop-bands in open periodic structures) with unusual dispersion and loss properties, *etc.*—are not observed in these cables over the spectral range of interest. It should be emphasized that this is due entirely to the very slow rate of twisting found in typical aerospace-grade STP cables, and is *not* a limitation or defect of the filament model.

The essential consequence of this slow rate of twisting is a small correction to the eigenvalues and mode fields of SUP cable, which can be analyzed exactly and in great detail. The correction is important for propagation over long segments of STP cable; however, in analyzing local interactions—connection to source and load, scattering from a hole in the shield, *etc.*—the simpler SUP cable model may be used instead.

The simulations have shown that the eigenvalues simulated from the simplified theoretical model are close enough to the eigenvalues of the true impedance controlled cable to be realistic for practical application. The fields generated by the historical tape model are not distributed anywhere near as uniformly as those in the wire model, and probably should not be used for reflectometry applications.

The fields within a fault, which when scaled by the effective area of the fault are proportional to the expected reflections, are heavily dependent not only on distance from source but also upon the angular location. For a fault at a fixed distance from source, the fields were shown to vary by a factor of at least two due to angular variation alone. The calculated electrostatic 2-d capacitances varied by a few picofarads with respect to angle. The capacitances varied by almost 30 pF with respect to hole size ranging from 0.5 mm to 2.5 mm. The ability to detect a fault can be thought of as being proportional to this change in capacitance. Most reflectometry systems will require at least a few picofarads of change to reliably detect a fault.

Classical trade-offs still exist. For example, reflectometry that employs a fast rise-time edge pulse will better be able to discern the edges of a small hole fault the higher the frequency becomes, with the down-side that the loss with respect to cable length increases with frequency. The loss characteristics for shielded twisted pair are not really that different from coaxial cable such as RG-58. The difference is in the additional ambiguity that the angular position of the hole fault adds to the quantification of detectability.

Modeling of a chafed segment of cable as a characteristic-impedance jump in an otherwise uniform line is a proven method that leads to a fast look-up table approach for fault detection [82]. Likewise, Bayesian inference of unknown cable and fault parameters using nested sampling was successfully implemented by the present authors before [78]. This approach met with great success here as well. Specifically, optimal fits to experimental data have demonstrated that the SUP cable model indeed provides an acceptable fit to data from STP cables up to 1 GHz. Not surprisingly, the slight analytical correction for twisting does not have a significant effect on the fits, but it does seem to reduce the bias on underlying parameter estimates. It is

therefore judged that other (unmodeled) elements in the system (*e.g.*, cable imperfections, connectors, VNA calibration drifts, *etc.*) are mainly responsible for the residual.

It is observed that the simple impedance-discontinuity model of a chafe is able to replicate the tell-tale "differentiation" effect of a small hole on a propagating pulse. It is also established empirically that average-size chafes do not produce a sensible reflection or transmission signal below 200 MHz, while unmodeled effects due to cable and connector imperfections start to become prominent above 1 GHz. It is therefore suggested that the theoretical cable and fault models derived here are suitable for chafe fault detection within a spectral window of roughly 0.2 – 1 GHz.

5.2 Areas of future research

Various open questions remain:

- first-principles modeling, verification, and validation of chafe faults, particularly when both common- and differential-mode signals are present on the cable;
- analytical modeling and/or numerical simulation of distributed (random) scattering from cable imperfections (*e.g.*, rough shield surface, nonuniform twist rate, *etc.*);
- development of closed-form or look-up-table S-parameter models for typical connectors;
- physics-based trade-space study of fault detectability in practical settings;
- (more) realistic noise models for more robust fault detection algorithm design;
- implementation of fast deterministic optimization algorithms for on-line fault detection;

among others. Some of these items are currently in the investigation pipeline.

5.3 Acknowledgments

This work was funded by NASA's Aeronautics Research Mission Directorate under the Vehicle Systems Safety Technologies Project of the Aviation Safety Program. The authors gratefully acknowledge the assistance of Mr D. Nishikawa of NASA Ames Research Center with the experimental aspects of this work.

5.4 Contact information

The authors of this report welcome questions and comments, and may be contacted as follows:

Author	**Telephone**	**E-mail**	**Main contribution**
Stefan R. Schuet	(650) 604-1802	`stefan.r.schuet@nasa.gov`	experiment (§4)
Doğan A. Timuçin	(650) 604-1262	`dogan.a.timucin@nasa.gov`	theory (§2)
Kevin R. Wheeler	(650) 604-3807	`kevin.r.wheeler@nasa.gov`	simulation (§3)

Bibliography

[1] K. R. Wheeler, D. A. Timucin, I. X. Twombly, K. F. Goebel, and P. F. Wysocki. (2007, June) Aging aircraft wiring fault detection survey. [Online]. Available: http://ti.arc.nasa.gov/m/pub-archive/1342h/1342%20(Wheeler).pdf

[2] CFR NPRM 05-08. (2005, October) Enhanced airworthiness program for airplane systems fuel tank safety. [Online]. Available: http://rgl.faa.gov/

[3] L. A. Griffiths, R. Parakh, C. Furse, and B. Baker, "The invisible fray: A critical analysis of the use of reflectometry for fray location," *IEEE Sensors Journal*, vol. 6, no. 3, June 2006.

[4] D. K. Cheng, *Field and Wave Electromagnetics*, 2nd ed. Reading, MA: Addison-Wesley, 1989.

[5] W. R. Smythe, *Static and Dynamic Electricity*, 3rd ed. New York, NY: McGraw-Hill, Inc., 1968.

[6] R. E. Collin, *Field Theory of Guided Waves*, 2nd ed. Hoboken, NJ: IEEE/John Wiley & Sons, Inc., 1991.

[7] A. W. Gent, "Capacitance of shielded balanced-pair transmission line," *Electrical Communication*, vol. 33, no. 3, pp. 234–240, September 1956.

[8] M. P. Sarma and W. Janischewsky, "Electrostatic field of a system of parallel cylindrical conductors," *IEEE Transactions on Power Apparatus and Systems*, vol. 88, no. 7, pp. 1069–1079, July 1969.

[9] V. Alessandrini, H. Fanchiotti, C. A. G. Canal, and H. Vucetich, "Exact solution of electrostatic problem for a system of parallel cylindrical conductors," *Journal of Applied Physics*, vol. 45, no. 8, pp. 3649–3661, August 1974.

[10] K. Foster and R. Anderson, "Capacitances of the shielded-pair line," *Proceedings of the IEE*, vol. 119, no. 7, pp. 815–820, July 1972.

[11] A. Gavrilakis, A. P. Duffy, K. G. Hodge, and A. J. Willis, "Partial capacitance calculation for shielded twisted pair cables," *IEEE Transactions on Electromagnetic Compatibility*, vol. 46, no. 2, pp. 299–302, May 2004.

[12] J. D. Jackson, *Classical Electrodynamics*, 3rd ed. New York, NY: John Wiley & Sons, Inc., 1999.

[13] J. W. Craggs, "The determination of capacity for two-dimensional systems of cylindrical conductors," *Quarterly Journal of Mathematics*, vol. 17, pp. 131–137, 1945.

[14] J. W. Craggs and C. J. Tranter, "The capacity of two-dimensional conductors and dielectrics with circular boundaries," *Quarterly Journal of Mathematics*, vol. 17, pp. 139–144, 1946.

[15] C. M. Miller, "Capacitances of a shielded balanced-pair transmission line," *The Bell System Technical Journal*, vol. 51, no. 3, pp. 759–776, March 1972.

[16] J. D. Nordgård, "The capacitances and surface-charge distributions of a shielded balanced pair," *IEEE Transactions on Microwave Theory and Techniques*, vol. 24, no. 2, pp. 94–100, February 1976.

[17] ——, "The capacitances and surface-charge distributions of a shielded unbalanced pair," *IEEE Transactions on Microwave Theory and Techniques*, vol. 25, no. 2, pp. 137–140, February 1977.

[18] G. S. Smith and J. D. Nordgård, "On the design and optimization of the shielded-pair transmission line," *IEEE Transactions on Microwave Theory and Techniques*, vol. 28, no. 8, pp. 887–893, August 1980.

[19] J. R. Carson, "Wave propagation over parallel wires: The proximity effect," *Philosophical Magazine*, vol. 41, no. 244, pp. 607–633, 1921.

[20] H. B. Dwight, "Proximity effect in wires and thin tubes," *Transactions of the American Institute of Electrical Engineers*, vol. 42, pp. 850–859, June 1923.

[21] S. P. Mead, "Wave propagation over parallel tubular conductors: The alternating current resistance," *The Bell System Technical Journal*, vol. 4, no. 2, pp. 327–338, April 1925.

[22] J. R. Carson, "The rigorous and approximate theories of electrical transmission along wires," *The Bell System Technical Journal*, vol. 7, no. 1, pp. 11–25, January 1928.

[23] R. S. Hoyt and S. P. Mead, "Mutual impedances of parallel wires," *The Bell System Technical Journal*, vol. 14, no. 3, pp. 509–533, July 1935.

[24] A. H. M. Arnold, "The alternating-current resistance of parallel conductors of circular cross-section," *Journal of the Institution of Electrical Engineers*, vol. 77, pp. 49–58, 1935.

[25] E. I. Green, F. A. Leibe, and H. E. Curtis, "The proportioning of shielded circuits for minimum high-frequency attenuation," *The Bell System Technical Journal*, vol. 15, no. 2, pp. 248–283, April 1936.

[26] A. H. M. Arnold, "Proximity effect in solid and hollow round conductors," *Journal of the Institution of Electrical Engineers*, vol. 88, pp. 349–359, 1941.

[27] G. S. Smith, "Proximity effect in systems of parallel conductors," *Journal of Applied Physics*, vol. 43, no. 5, pp. 2196–2203, May 1972.

[28] V. Belevitch, "Theory of the proximity effect in multiwire cables," *Philips Research Reports*, vol. 32, pp. 16–43 and 96–117, 1977.

[29] W. Sollfrey, "Wave propagation on helical wires," *Journal of Applied Physics*, vol. 22, no. 7, pp. 905–910, 1951.

[30] R. A. Waldron, "A helical coordinate system and its applications in electromagnetic theory," *Quarterly Journal of Mechanics and Applied Mathematics*, vol. XI, no. 4, pp. 438–461, 1958.

[31] L. Lewin, *Theory of Waveguides*. New York, NY: John Wiley & Sons, Inc., 1975.

[32] L. B. Felsen and N. Marcuvitz, *Radiation and Scattering of Waves*. Englewood Cliffs, NJ: Prentice-Hall, Inc., 1973.

[33] J. G. van Bladel, *Electromagnetic Fields*, 2nd ed. Hoboken, NJ: IEEE/John Wiley & Sons, Inc., 2007.

[34] C. A. Balanis, *Advanced Engineering Electromagnetics*. New York, NY: John Wiley & Sons, Inc., 1989.

[35] A. Ishimaru, *Electromagnetic Wave Propagation, Radiation, and Scattering*. Englewood Cliffs, NJ: Prentice-Hall, Inc., 1991.

[36] G. Conciauro, M. Bressan, and C. Zuffada, "Waveguide modes vla an integral equation leading to a linear matrix eigenvalue problem," *IEEE Transactions on Microwave Theory and Techniques*, vol. 32, no. 11, pp. 1495–1504, November 1984.

[37] R. S. Phillips, "The electromagnetic field produced by a helix," *Quarterly of Applied Mathematics*, vol. 8, no. 3, pp. 229–246, 1950.

[38] A. Y. Alksne, "Magnetic fields near twisted wires," *IEEE Transactions on Space Electronics and Telemetry*, vol. 10, pp. 154–158, December 1964.

[39] J. R. Moser and R. F. Spencer, Jr., "Predicting the magnetic fields from a twisted-pair cable," *IEEE Transactions on Electromagnetic Compatibility*, vol. 10, no. 3, pp. 324–329, September 1968.

[40] S. Shenfeld, "Magnetic fields of twisted-wire pairs," *IEEE Transactions on Electromagnetic Compatibility*, vol. 11, pp. 164–169, November 1969.

[41] C. D. Taylor and J. P. Castillo, "On the response of a terminated twisted-wire cable excited by a plane-wave electromagnetic field," *IEEE Transactions on Electromagnetic Compatibility*, vol. 22, no. 1, pp. 16–19, February 1980.

[42] R. Stolle, "Electromagnetic coupling of twisted pair cables," *IEEE Journal on Selected Areas in Communications*, vol. 20, no. 5, pp. 883–892, June 2002.

[43] Y. Leviatan and A. T. Adams, "The response of a two-wire transmission line to incident field and voltage excitation, including the effects of higher order modes," *IEEE Transactions on Antennas and Propagation*, vol. 30, no. 5, pp. 998–1003, September 1982.

[44] J. D. Kraus, *Antennas*, 2nd ed. New York, NY: McGraw-Hill, Inc., 1988.

[45] J. R. Pierce, *Traveling-Wave Tubes*. New York, NY: D. Van Nostrand Co., Inc., 1950.

[46] P. K. Tien, "Traveling-wave tube helix impedance," *Proceedings of the IRE*, pp. 1617–1623, November 1953.

[47] ——, "Bifilar helix for backward-wave oscillators," *Proceedings of the IRE*, pp. 1137–1143, July 1954.

[48] J. R. Pierce and P. K. Tien, "Coupling of modes in helixes," *Proceedings of the IRE*, vol. 25, no. 9, pp. 1389–1396, September 1954.

[49] L. Stark, "Lower modes of a concentric line having a helical inner conductor," *Journal of Applied Physics*, vol. 25, no. 9, pp. 1155–1162, September 1954.

[50] S. Sensiper, "Electromagnetic wave propagation on helical structures (a review and survey of recent progress)," *Proceedings of the IRE*, pp. 149–161, February 1955.

[51] H. R. Johnson, T. E. Everhart, and A. E. Siegman, "Wave propagation on multifilar helices," *IRE Transactions on Electron Devices*, pp. 18–24, January 1956.

[52] C.-M. Chu, "Propagation of waves in helical wave guides," *Journal of Applied Physics*, vol. 29, no. 1, pp. 88–99, January 1958.

[53] H. Buchholz, *Elektrische und Magnetische Potentialfelder*. Berlin: Springer-Verlag, 1957.

[54] D. A. Watkins, *Topics in Electromagnetic Theory*. New York, NY: John Wiley & Sons, Inc., 1958.

[55] S. Ramo, J. R. Whinnery, and T. van Duzer, *Fields and Waves in Communication Electronics*, 3rd ed. New York, NY: John Wiley & Sons, Inc., 1994.

[56] D. Chernin, T. M. Antonsen, Jr., and B. Levush, "Exact treatment of the dispersion and beam interaction impedance surrounded by a radially stratified dielectric of a thin tape helix," *IEEE Transactions on Electron Devices*, vol. 46, no. 7, pp. 1472–1483, July 1999.

[57] V. J. Fowler, "Analysis of helical transmission lines by means of the complete circuit equations," *IRE Transactions on Antennas and Propagation*, vol. 2, pp. 132–143, October 1954.

[58] J. E. Schutt-Ainé, "High-frequency characterization of twisted-pair cables," *IEEE Transactions on Communications*, vol. 49, no. 4, pp. 598–601, April 2001.

[59] C. R. Paul and J. W. McKnight, "Prediction of crosstalk involving twisted pairs of wires–part I: A transmission-line model for twisted-wire pairs," *IEEE Transactions on Electromagnetic Compatibility*, vol. 21, no. 2, pp. 92–105, May 1979.

[60] ——, "Prediction of crosstalk involving twisted pairs of wires–part II: A simplified low-frequency prediction model," *IEEE Transactions on Electromagnetic Compatibility*, vol. 21, no. 2, pp. 105–114, May 1979.

[61] J. A. B. Faria and M. V. G. das Neves, "Analysis of the helical twisted-wire pair running above ground: transfer function evaluation," *IEEE Transactions on Electromagnetic Compatibility*, vol. 45, no. 2, pp. 449–453, May 2003.

[62] C. Buccella, M. Feliziani, and G. Manzi, "Three-dimensional FEM approach to model twisted wire pair cables," *IEEE Transactions on Magnetics*, vol. 43, no. 4, pp. 1373–1376, April 2007.

[63] S. Caniggia, A. Maffucci, F. Maradei, F. Villone, and W. Zamboni, "3-D numerical modeling and circuit extraction techniques for the analysis of unshielded twisted pairs," *IEEE Transactions on Magnetics*, vol. 43, no. 4, pp. 1357–1360, April 2007.

[64] M. Jakovljević, T. Magesacher, K. Ericson, P. Ödling, P. O. Börjesson, and S. Zazo, "Common mode characterization and channel model verification for shielded twisted pair (STP) cable," in *Proceedings of the International Conference on Communications*. IEEE, 2008, pp. 447–451.

[65] R. A. Waldron, "Theory of the helical waveguide of rectangular cross-section," *Journal of the British IRE*, vol. 17, pp. 577–592, October 1957.

[66] P. M. Morse and H. Feshbach, *Methods of Theoretical Physics*. New York, NY: McGraw-Hill, Inc., 1953.

[67] R. E. Collin, *Foundations for Microwave Engineering*, 2nd ed. New York, NY: McGraw-Hill, Inc., 1992.

[68] M. Abramowitz and I. A. Stegun, Eds., *Handbook of Mathematical Functions*. New York, NY: Dover, 1965.

[69] F. W. J. Olver, D. W. Lozier, R. F. Boisvert, and C. W. Clark, Eds., *NIST Handbook of Mathematical Functions*. Cambridge, UK: Cambridge University Press, 2010.

[70] W. H. Press, S. A. Teukolsky, W. T. Vetterling, and B. P. Flannery, *Numerical Recipes—The Art of Scientific Computing*, 3rd ed. Cambridge, UK: Cambridge University Press, 2007.

[71] C. R. Paul, *Analysis of Multiconductor Transmission Lines*. New York, NY: John Wiley & Sons, Inc., 1994.

[72] J. M. van Hofweegen and K. S. Knol, "A universal adjustable transformer for U.H.F. work," *Philips Research Reports*, vol. 3, pp. 140–155, 1948.

[73] R. W. P. King, *Transmission-Line Theory*. New York, NY: Dover, 1965.

[74] B. G. King, J. McKenna, and G. Raisbeck, "Experimental check of formulas for capacitance of shielded experimental check of formulas for capacitance of shielded balanced-pair transmission line," *Proceedings of the IRE*, vol. 46, pp. 922–923, May 1958.

[75] S. A. Schelkunoff, "The electromagnetic theory of coaxial transmission lines and cylindrical shields," *The Bell System Technical Journal*, vol. 13, no. 4, pp. 532–579, October 1934.

[76] J. A. Stratton, *Electromagnetic Theory*. New York, NY: McGraw-Hill, Inc., 1941.

[77] D. E. Bockelman and W. R. Eisenstadt, "Combined differential and common-mode scattering parameters: Theory and simulation," *IEEE Transactions on Microwave Theory and Techniques*, vol. 43, no. 7, pp. 1530–1539, July 1995.

[78] S. Schuet, D. Timucin, and K. Wheeler, "A model-based probabilistic inversion framework for characterizing wire fault detection using TDR," *IEEE Transactions on Instrumentation and Measurement*, vol. 60, no. 5, pp. 1654–1663, May 2011.

[79] A. Gelman, J. Carlin, H. Stern, and D. Rubin, *Bayesian Data Analysis*, 2nd ed. Chapman & Hall/CRC, 2004.

[80] J. Skilling, "Nested sampling for general bayesian computation," *Bayesian Analysis*, vol. 1, no. 4, pp. 833–860, 2006. [Online]. Available: http://ba.stat.cmu.edu/journal/2006/vol01/issue04/skilling.pdf

[81] N. Chopin and C. P. Robert, "Properties of nested sampling," *Biometrika*, p. asq021, 2010. [Online]. Available: http://biomet.oxfordjournals.org/cgi/content/abstract/asq021v1

[82] M. Kowalski, "A simple and efficient computational approach to chafed cable time-domain reflectometry signature prediction," in *Annual Review of Progress in Applied Computational Electromagnetics Conference*. ACES, March 2009.

REPORT DOCUMENTATION PAGE

Form Approved
OMB No. 0704–0188

1. REPORT DATE *(DD-MM-YYYY)*	2. REPORT TYPE	3. DATES COVERED *(From - To)*
01-03-2012	Technical Memorandum	10/2010–9/2011

4. TITLE AND SUBTITLE
Shielded-twisted-pair cable model for chafe fault detection via time-domain reflectometry

5a. CONTRACT NUMBER

5b. GRANT NUMBER

5c. PROGRAM ELEMENT NUMBER

6. AUTHOR(S)
Stefan R. Schuet, Doğan A. Timuçin, and Kevin R. Wheeler

5d. PROJECT NUMBER

5e. TASK NUMBER

5f. WORK UNIT NUMBER
284848.02.03.01.03

7. PERFORMING ORGANIZATION NAME(S) AND ADDRESS(ES)
NASA Ames Research Center
Moffett Field, California 94035-1000

8. PERFORMING ORGANIZATION REPORT NUMBER

9. SPONSORING/MONITORING AGENCY NAME(S) AND ADDRESS(ES)
National Aeronautics and Space Administration
Washington, DC 20546-0001

10. SPONSOR/MONITOR'S ACRONYM(S)
NASA

11. SPONSOR/MONITOR'S REPORT NUMBER(S)
NASA/TM–2012–216001

12. DISTRIBUTION/AVAILABILITY STATEMENT
Unclassified-Unlimited
Subject Category 03
Availability: NASA CASI (443) 757-5802

13. SUPPLEMENTARY NOTES
An electronic version can be found at http://ntrs.nasa.gov.

14. ABSTRACT
This report details the development, verification, and validation of an innovative physics-based model of electrical signal propagation through shielded-twisted-pair cable, which is commonly found on aircraft and offers an ideal proving ground for detection of small holes in a shield well before catastrophic damage occurs. The accuracy of this model is verified through numerical electromagnetic simulations using a commercially available software tool. The model is shown to be representative of more realistic (analytically intractable) cable configurations as well. A probabilistic framework is developed for validating the model accuracy with reflectometry data obtained from real aircraft-grade cables chafed in the laboratory.

15. SUBJECT TERMS
Waveguide theory, transmission-line theory, shielded-twisted-pair cable, electromagnetic wave propagation, numerical electromagnetic simulations, scattering parameters, chafing, fault detection, time-domain reflectometry

16. SECURITY CLASSIFICATION OF:			17. LIMITATION OF ABSTRACT	18. NUMBER OF PAGES	19a. NAME OF RESPONSIBLE PERSON
a. REPORT	b. ABSTRACT	c. THIS PAGE			STI Help Desk (email: help@sti.nasa.gov)
U	U	U	UU	71	19b. TELEPHONE NUMBER *(Include area code)* (443) 757-5802